

N° d'ordre NNT : 2017LYSE1189

THÈSE DE DOCTORAT DE L'UNIVERSITÉ DE LYON

opérée au sein de

l'Université Claude Bernard Lyon 1

École Doctorale ED52

Ecole doctorale de Physique et d'Astrophysique (PHAST)

Spécialité de doctorat : Physique

Soutenue publiquement le 28 septembre 2017, par :

Tanguy Damart

Energy dissipation in oxide glasses

Devant le jury composé de :

M. Anaël Lemaître, Professeur, Ecole des Ponts ParisTech	Rapporteur
M. Benoit Rufflé, Professeur, Université de Montpellier	Rapporteur
Mme Catherine Barentin, Professeur, Université de Lyon	Présidente
M. Tanguy Rouxel, Professeur, Université de Rennes 1	Examinateur
M. David Rodney, Professeur, Université de Lyon	Directeur de thèse
Mme Anne Tanguy , Professeur, INSA de Lyon	Co-directrice de thèse

It is common for people first starting to grapple with computers to make large-scale computations of things they might have done on a smaller scale by hand. They might print out a table of the first 10,000 primes, only to find that their printout isn't something they really wanted after all. They discover by this kind of experience that what they really want is usually not some collection of answers, what they want is understanding.

William P. Thurston

Summary

The origin of sound attenuation at low and high frequency in glasses stays elusive mainly because of the complex temperature and frequency dependence of the phenomena at its root. Indeed, the presence of complex structures and multi-scale organizations in glasses induce the existence of relaxation times ranging from the second to the femto-second as well as spatial correlations ranging from the Angström to a hundred nanometers. Therefore, the study of attenuation and dissipation requires to look not only at the interactions between the disordered medium and mechanical waves of different frequencies but also to inspect the interaction between local structures and waves of different wave-vectors.

At low-frequency (below the MHz), a better understanding of the phenomena at the origin of dissipation would be beneficial for several applications. For example, the multi-layers coating the mirrors of gravitational wave detectors consist of a superposition of two oxide glasses: silica (SiO_2) and tantalum pentoxide (Ta_2O_5), chosen for their optical properties. These glasses are an important source of dissipation limiting the accuracy of the detector as a whole. It was recently shown that doping Ta_2O_5 with TiO_2 leads to a decrease in the mechanical loss, opening the way towards the synthesis of high performance materials. However, the atomistic origin of this decrease is as of today not understood, mainly because of our ignorance about the structure of these glasses.

At high frequency (in the THz regime), when the wave-vector is small with respect to inter-atomic distances ($0.1 < q < 1 - 3\text{nm}^{-1}$ in silica), mechanical waves are attenuated because of elastic heterogeneities present in the glass. But when the wave-vector reaches a few nm^{-1}, glasses exhibit a strong increase in dissipation. Above this limit, refereed to as the Ioffe-Regel limit, vibrations cannot be described as phonons and the energy they carry propagates more diffusively than ballisticaly. At these wave-vectors, mechanical waves interact directly with the atomic disorder. The study of dissipation in this regime raises theoretical questions about the link between attenuation and dissipation as well as between local atomic symmetry and dissipation.

In the present study, we conducted a thorough analysis of the interaction between mechanical waves and the structure of two oxide glasses using simulation techniques such as non-equilibrium molecular dynamics. In a first part, we characterized the still unknown structure of Ta_2O_5 and

TiO_2 doped Ta_2O_5 glasses. We showed that amorphous Ta_2O_5 consists of polyhedra organized in a chain-like structure that is not disrupted by the addition of TiO_2. Furthermore, performing a normal mode analysis, we proposed a reinterpretation of their Raman spectra.

In a second step, we examined energy dissipation in SiO_2 and Ta_2O_5. At high-frequencies, we used mechanical spectroscopy to measure dissipation numerically and performed in parallel an analytical development based on the projection of the atomic motion on the vibrational eigenmodes. We showed that dissipation is harmonic in the THz regime and that it can be expressed analytically provided that the atomic positions and interactions are known. These analytical expressions reveal the role played by non-affine motions in dissipation, which, in the case of a hydrostatic wave, is directly related to local symmetry. We showed that a local atomic symmetry field projected on the vibrational eigenmodes of the glass is the key quantity regulating dissipation. In SiO_2 and Ta_2O_5 glasses, the asymmetry is larger for the oxygen atoms whose non-affine displacements produce vibration mainly of the Si-O-Si and Ta-O-Ta bonds.

At low-frequencies, we used molecular dynamics and the nudged elastic band method to gather sets of thermally activated bistable states accepted as source of dissipation. We were able to class these events know as two-level systems (TLS) in three categories based on topologically distinct atomic motions. From these sets of events and using a TLS model that takes into account the tensorial nature of the sensitivity of the TLS to the strain and the difference in attempt frequency between the initial and final states, we predicted dissipation numerically. We also showed that the approximations used in the literature to fit experimental data are valid in the low temperature limit. Finally, we showed that the dissipation predicted from our numerical calculations is of the same order as the experimental measurements, showing a direct link between the TLSs identified here at the atomic scale and macroscopic measurement of energy dissipation.

Through this study, we highlighted the importance of the structure of glasses, especially at the short- and medium- range order, in the context of energy dissipation in the two extreme frequency ranges (below the MHz and above the GHz).

RÉSUMÉ

L'atténuation d'ondes à basses et hautes fréquences dans les verres n'est pas encore bien comprise en grande partie car les phénomènes à l'origine de cette dissipation varient grandement en fonction de la fréquence. L'existence de structures complexes et d'organisations multi-échelles dans les verres favorisent l'apparition de temps de relaxation allant de la seconde à la femtoseconde et de corrélations prenant place de l'Angström à la centaine de nanomètres. Il est donc nécessaire d'étudier l'interaction du matériau avec des ondes mécaniques variant en fréquence et parallèlement d'étudier l'interaction entre les structures locales et des ondes possédant différentes longueurs d'onde.

A basse fréquence, une meilleure compréhension de ces phénomènes de dissipation serait bénéfique à de nombreux domaines. Par exemple, les multi-couches recouvrant les miroirs des interféromètres servant à détecter les ondes gravitationnelles sont réalisées à partir de verres d'oxydes, le silica (SiO_2) et l'oxyde de tantale (Ta_2O_5), choisis pour leurs propriétés optiques. Cependant, ces verres sont une source majeure de dissipation et limitent la précision du détecteur dans son ensemble. Il a récemment été montré que le dopage du Ta_2O_5 avec du TiO_2 entraînait une réduction des pertes mécaniques dans le verre, ouvrant ainsi la voie vers la synthèse de matériaux plus performants. Cependant, l'origine atomique de cette diminution n'est pas encore comprise, en grande partie à cause de notre méconnaissance de la structure de ces verres.

A haute fréquence, lorsque la taille du vecteur d'onde est encore petite par rapport aux distances inter-atomiques ($0.1 < q < 1-3$ nm^{-1} dans la silice), les ondes mécaniques sont atténuées dû à leurs interactions avec les hétérogénéités élastiques présentes dans le verre. Lorsque le vecteur d'onde atteint quelques nm^{-1}, le verre présente une rapide augmentation de sa dissipation. Au-delà de cette limite, appelée limite de Ioffe-Regel, les modes propres ne peuvent être considérés comme des phonons et propagent l'énergie de manière plus diffusive que balistique. Les ondes mécaniques sentent alors directement le désordre atomique et interagissent de manière forte avec les modes propres de vibrations du système. A ces fréquences, l'étude de la dissipation pose des questions théoriques sur le lien entre asymétrie locale et atténuation acoustique.

Durant cette étude, nous avons réalisé une analyse approfondie de l'interaction entre ondes mécaniques et structure des verres en utilisant des techniques de simulation telles que la

dynamique moléculaire et la dynamique moléculaire hors équilibre. En partant de la synthèse de verres de SiO_2 et Ta_2O_5, nous nous sommes appliqués à trouver l'origine structurelle de la dissipation aux différentes échelles de fréquence.

Dans un premier temps, nous avons caractérisé la structure encore peu connue du Ta_2O_5 et du Ta_2O_5 dopé au TiO_2 en montrant la structure en chaîne que ceux-ci adoptent dans leurs organisations à moyenne distance. De plus, grâce à une analyse des modes propres dans ces verres, nous avons pu proposer une ré-interprétation de leurs spectres Ramans.

Nous nous sommes ensuite penchés sur l'étude de la dissipation. A haute fréquence, nous avons utilisé une technique de spectroscopie mécanique appuyée par un développement analytique basé sur la projection du mouvement atomique sur les vecteurs propres de vibration. Nous avons montré que la dissipation à ces fréquences est harmonique et qu'elle peut être exprimée analytiquement pour peu que les positions et interactions atomiques soient connues. Les expressions analytiques ainsi obtenues révèlent le rôle joué par les mouvements non-affines dans le phénomène de dissipation. Dans le cas d'une onde de déformation hydrostatique, cela se traduit par une importance de la symétrie atomique locale, qui, projetée sur les modes propres de vibrations, est la quantité clé décidant du pouvoir dissipatif d'un mode propre de vibration. Pour les verres de SiO_2 et Ta_2O_5 l'asymétrie est plus grande pour les atomes d'oxygène dont les déplacements non-affines produisent des vibrations, principalement des liaisons Si-O-Si et Ta-O-Ta.

A basse fréquence, nous avons utilisé la dynamique moléculaire ainsi que la méthode NEB pour obtenir des listes d'évènements thermiquement activés appelés Two-Level Systems (TLS) et reconnus comme source de dissipation. Nous avons été capable de classer ces évènements en trois catégories correspondant à des mouvements atomiques topologiquement distincts. A partir de ces événements et en utilisant une théorie des états à deux niveaux prenant en compte la nature tensorielle de la sensibilité aux déformations des TLSs et la différence de fréquence d'attaque entre l'état initial et l'état activé des TLSs, nous avons prédit numériquement la dissipation. Par la suite, nous avons discuté du bien-fondé des approximations employées dans la littérature lorsque le modèle TLS est utilisé pour fitter des données expérimentales. Comparant notre dissipation calculée numériquement à des mesures de dissipation expérimentales, nous avons montré que le modèle TLS permet de reproduire l'amplitude de la dissipation expérimentale révélant ainsi un lien fort entre les relaxations atomiques thermiquement activées et la dissipation.

A travers cette étude, nous avons mis en évidence l'importance du rôle de la structure des verres dans le contexte de la dissipation à haute et basse fréquence (au-dessus du THz et en dessous du MHz).

Table of Contents

Page

1 Introduction **1**

2 Background **5**

2.1 The Multi-scale Structure of Glasses 5

2.1.1 Short-, Medium- and Long- Range Orders 5

2.1.2 The Potential Energy Landscape of Oxide Glasses 8

2.2 Energy Dissipation in Glasses 10

2.2.1 Investigation Tools for Dissipation in Glasses 11

2.2.2 Energy Dissipation in Oxide Glasses 14

2.2.3 Thermal Noise in Gravitational Waves Detectors 17

2.3 Conclusion & Scope 19

3 Numerical Methods **21**

3.1 Molecular Dynamics 21

3.1.1 Temperature constraints 22

3.1.2 Periodic Boundary Conditions 23

3.1.3 The SLLOD Equations of Motion 24

3.1.4 Interatomic Potentials 25

3.2 Synthesizing Glasses 29

3.3 Exploring the Potential Energy Landscape 31

3.3.1 Finding new inherent structures using Molecular Dynamics 31

3.3.2 Nudged Elastic Band Method 32

3.3.3 The Activation Relaxation Technique 34

4 Structural and Vibrational Properties of Ta_2O_5 and TiO_2 doped Ta_2O_5 **37**

4.1 Structural Characterization 37

4.1.1 Tantalum Pentoxide (Ta_2O_5) 38

4.1.2 Titanium doped Tantalum Pentoxide (Ta_2O_5-TiO_2) 41

4.2 Vibrational Properties 42
4.2.1 Interpretation of the Raman spectra of Ta_2O_5 47
4.3 Summary 51

5 High Frequency Energy Dissipation 53
5.1 Methodology 54
5.1.1 Mechanical spectroscopy 54
5.1.2 Harmonic approximation 55
5.1.3 Analytic expression 56
5.2 Simulation Results 59
5.2.1 Full non-linear calculations 59
5.2.2 Harmonic approximation 60
5.3 Properties of Harmonic Dissipation 61
5.3.1 Physical interpretation 61
5.3.2 Influence of the Langevin friction parameter 62
5.3.3 Properties of C_m 64
5.3.4 Application to SiO_2 66
5.3.5 Application to Ta_2O_5 68
5.4 Summary 72

6 Low Frequency Energy Dissipation 73
6.1 Methodology 74
6.1.1 The Two-Level System model 74
6.1.2 Exploring the potential energy landscape 75
6.1.3 Deformation potential and attempt frequency 77
6.2 The case of SiO_2 77
6.2.1 Thermally Activated Relaxations in SiO_2 77
6.2.2 Application of the TLS model and Approximations 85
6.2.3 Comparison with experiments 88
6.3 The case of Ta_2O_5 90
6.3.1 Thermally Activated Relaxations in Ta_2O_5 90
6.3.2 Comparison with experiments 95
6.4 Summary 96

7 Conclusion 97

A Analytic Expression of the Complex Modulus in the Harmonic Approximation 101

A.1 Frequency-dependent pressure 101
A.2 Complex bulk modulus 104

B Potential Energy Landscape around an Inherent Structure 105

C Energy dissipation in the framework of the TLS model 109
C.1 Complex modulus 109
C.1.1 Equilibrium probabilities and detailed balance 109
C.1.2 Deformation potential 110
C.1.3 Master equation 111
C.1.4 Complex modulus 112
C.2 Longitudinal dissipation 112
C.3 Transverse dissipation 113

Bibliography 115

Acronyms

ART Activation relaxation technique.

BKS van Beest, Kramer, and van Santen.

C-NEB Climbing nudged elastic band.

DHO Damped harmonic oscillator.

EXAFS Extended X-ray absorption fine structure.

GW Gravitational wave.

hTST Harmonic transition state theory.

IBS Ion beam sputtering.

IR Ioffe-Regel.

IS Inherent state.

IXS Inelastic x-ray scattering.

LIGO Laser interferometer gravitational-wave observatory.

LRO Long-range order.

M-BKS Morse - van Beest, Kramer, and van Santen.

MD Molecular dynamics.

MEMS/NEMS Micro- and nanoelectromechanical systems.

MRO Medium-range order.

NEB Nudged elastic band.

NEMD Non-equilibrium molecular dynamics.

NVE Microcanonical.

PBC Periodic boundary condition.

PEL Potential energy landscape.

PR Participation ratio.

PU Picosecond ultrasonic.

RHS Right-hand side.

SRO Short-range order.

TAR Thermally activated relaxation.

TLS Two-level system.

TST Transition state theory.

VDOS Vibrational density of states.

CHAPTER 1

INTRODUCTION

Since the conceptualization of the notion of *gravific waves* by Henri Poincaré in 1905 [143] and the prediction of the existence of gravitational waves (GW) by Albert Einstein in 1937 [56], a collective endeavor led by the USA, Europe, Japan and Russia has focused on their detection. This work was at last validated in 2015 with the first detection of a GW by the Laser Interferometer Gravitational-Wave Observatory (LIGO) in collaboration with the Virgo interferometer [3]. To better appreciate the extent of this success, we should remind ourselves that despite the massive size of the events at their origin such as merging in binary star systems composed of white dwarfs, neutron stars or black holes, GWs are ripples of the space-time with an amplitude of merely 10^{-21} m when reaching Earth, as pictured in Fig. 1.1. To detect such small signals, large-scale Michelson interferometers have been designed. These interferometers comprise two arms several kilometers long, kept under vacuum, through which a laser beam propagate back and forth. The arms are placed perpendicularly to one another such that the slightest distortion of space in one of the two arms will be seen when the amplitudes of the two lasers are summed. To obtain a statistically significant signal-to-noise ratio, a search has been organized to characterize and bring all possible sources of noise below 10^{-20} m/$\sqrt{Hz}$. Part of this effort is directed toward understanding the phenomena at the origin of mechanical loss such as the energy dissipation taking place in the mirrors on which the laser is reflected. These mirrors are Bragg reflectors composed of thin film multilayers of a glass with a high index of reflection, tantalum pentoxide (Ta_2O_5) and one with a small index of reflection, silica (SiO_2).

However, the source of mechanical losses and thus energy dissipation in disordered solids such as oxide glasses remains elusive as it is both temperature- and frequency-dependent [188, 193]. In addition, the disparity existing in the short- and medium-range orders between different glasses

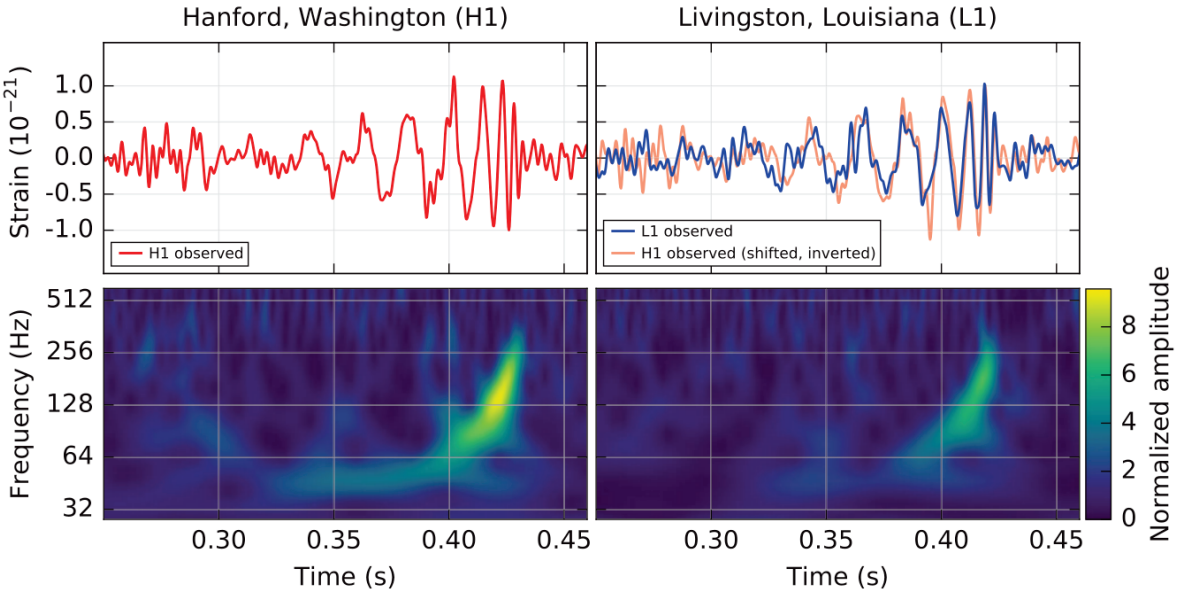

Figure 1.1: The gravitational-wave event GW150914 observed by the LIGO Hanford (left column panels) and Livingston (right column panels) detectors. The top row shows the strain fluctuation as a function of time while the lower row is a spectrogram of the strain. Figure reproduced from Ref. [3].

makes the atomistic phenomena at the origin of dissipation difficult to encapsulate. Added to these difficulties inherent to dissipation in glasses, there is a lack of experimental techniques able to probe the structure of disordered solids at the nanometer scale. In fact, classical experimental techniques are of no use on materials that present homogeneous structural or thermo-mechanical properties at the macro-scale while being heterogeneous below the nanometer. It is with the rise of numerical methods such as Molecular Dynamics (MD) or *ab-initio* calculations that the dynamics taking place at the atomic scale can be directly observed [147, 88].

The questions discussed in the present manuscript are as follow:

- How can numerical techniques and analytical calculations be used to model oxide glasses and their dissipative properties ?
- Which primitive units or rules are at the origin of the structure of oxide glasses such as SiO_2 and Ta_2O_5 ?
- Which phenomena are at the origin of dissipation in glasses at different frequencies and temperatures ?
- Which features of a glass control its dissipation ?

To answer these questions, we will use equilibrium and non-equilibrium molecular dynamics simulations to synthesize numerical oxide glasses and study their structure, before moving to an investigation of their dissipation properties in frequencies ranging first from the GHz to the THz and then from the Hz to the MHz.

The present manuscript is organized as follows:

First, chapter 2 will present the background needed to understand the importance of the present work, first in the context of the complexity of the structure of glasses and then in the context of energy dissipation. This chapter will also present traditional experimental investigation techniques as well as currently existing numerical tools.

In chapter 3, we will present the numerical methods such as the algorithms and techniques employed in our molecular dynamics code along with the protocols used to generate numerical glasses and the techniques deployed to explore their potential energy landscape.

Chapter 4 will consist of an in-depth study of the structure and vibrational properties of amorphous Ta_2O_5 and TiO_2-doped Ta_2O_5 glasses produced by molecular dynamics (MD). This chapter will first focus on the characterization of these glass structure at the short- and medium-range orders. Secondly, we will present a complete analysis of the vibrational modes of these glasses and discuss them with respect to the current interpretations of the Raman spectra of Ta_2O_5 glasses.

Chapter 5 is the first of two chapters considering dissipation, this first one will examine dissipation above GHz frequencies using a combination of non-equilibrium MD simulations and analytical calculations derived in the harmonic approximation. The dissipation will be shown to arise from non-affine relaxations triggered by the applied strain through the excitation of vibrational eigenmodes that act as damped harmonic oscillators.

In chapter 6, the last part of the present manuscript, we will study dissipation below the MHz. This study will be conducted using potential energy landscape exploration techniques and the Two-Level System model. It will show that dissipation in this frequency range comes from thermally activated atomic events that will be sorted in groups of similar topologies despite the apparent disorder of the glass.

CHAPTER 2

BACKGROUND

2.1 The Multi-scale Structure of Glasses

2.1.1 Short-, Medium- and Long- Range Orders

In solids, the state of matter reached when enough kinetic energy has been taken from the atoms with respect to their will to bound, the atoms lay in a state of lowest potential energy. This energy minimization process that is solidification is at the origin of two antagonistic but sometimes energetically equivalent structures. In the first one, referred to as the crystalline structure, atoms are organized periodically in space as the repetition of a basic pattern, a unit cell, where the collective organization of atoms is optimized to minimize the energy.

The second possible type of structure is the amorphous structure where no apparent order exists at long range in the atomic organization. Since crystals appear as a process of energy minimization, one can wonder, why are amorphous materials disordered? The answer resides in the formation of the solid: when a melt is cooled, the atoms diffuse, looking for the optimal location in order to minimize collectively energy. But if the cooling rate is high with respect to the diffusion rate of the particles, the atoms end up frozen in sub-optimal positions. For example in water, where the H_2O molecules self-diffuse at 10^{-9} m^2/s, crystals are formed easily [84], on the other hand in polymer melts, the molecular chains diffuse slowly, 10^{-11} m^2/s, leading to a low degree of crystallization [16]. Amorphous materials take different forms such as polymers, glasses or gels, but we will restrict our attention in the rest of this manuscript to the case of oxide glasses. Oxide glasses are the result of a mix of a transition-metal ion or a metalloid ion with oxygen and include numerous compounds such as silica (SiO_2) or lime (CaO). Silicon dioxide, or

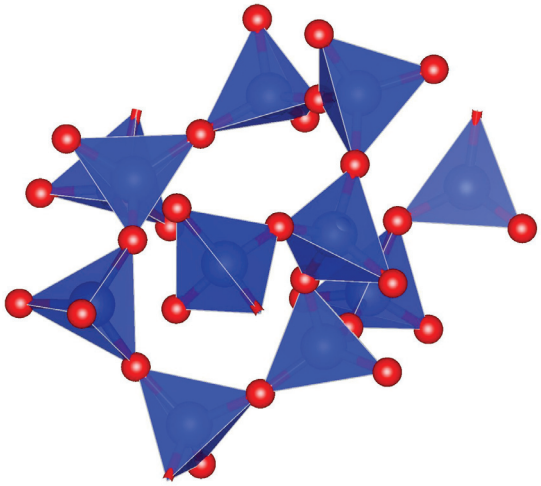

Figure 2.1: Part of a numeric SiO_2 glass synthesized using molecular dynamics, the blue/red spheres represents the silicium/oxygen atoms respectively.

silica, accounts for more than 60% of the earth crust and is heavily used in industry to produce window panels, cement or ceramics but also as additive in food or as insulator in micro-electronic. In addition, silica is sometimes referred to as an *ideal* glass because its local order based on tetrahedra is perfectly compatible with its stoichiometry. It is thus not surprising that silica is one of the most studied oxide glass [27, 207, 197, 181, 182, 145, 96] and will be used as a glass model in the present study.

Due to atomic disorder, the complete description of a glass such as SiO_2 is impossible. Consequently, the concepts of short-, medium- and long-range orders (SRO, MRO, LRO) have been proposed to depict the structure of materials as a sum of recurrent motifs. The mechanical and vibrational properties generated at the SRO, MRO and LRO are summarized in Fig. 2.2 (see Ref. [152] for a pertinent review of the link between elastic properties and SRO).

Short-Range Order: in the present manuscript, SRO will refer to distances and structures formed by the first shell of neighbors. At the SRO, structural motifs are often described as simple polyhedra as in SiO_2, composed of Si centered tetrahedra as represented in Fig. 2.1, where each Si atom is four-folded and each O atom is two-folded. At the SRO level, the local environment of an atom is often similar to the corresponding crystal since the same individual atomic forces apply between atom as in silica, although some other glasses such as metallic glasses can present structures such as icosahedra, not seen in their crystalline form [170]. In both cases, since the atoms did not have enough time to diffuse to their optimal position compared to crystals, the pair distribution function and angle distribution show broader peaks. These small heterogeneities at the SRO coupled to structures that cannot stack without faults such as the above-mentionned icosahedra, will provoke the disorder seen at larger scales. At the SRO, the first neighbor bonds

are responsible for high frequency vibrations that resemble the optic-modes seen in crystals. Another type of vibrations, referred to as Soft Modes, are also seen at the SRO. Soft modes are low-frequency vibrations centered on an unstable atom or group of atoms that play a role in plastic deformation [179].

Medium-Range Order: the MRO describes the order existing from two to several tens of bond lengths. At the MRO, the pilling of small bond distortions seen in the simple structures of the SRO intertwine and give rise to complex figures that are hard to characterize or catalog [173, 145, 168, 40]. While at the SRO, the glass can be described using pair distribution functions and simple polyhedra, the MRO is more challenging as the structures seen at this scale are glass dependent. Rings and chains allow for a good understanding for some glasses, but generalizable quantitative measurement are needed. To this end, several leads are explored; based on topology and graph theory such as the use of persistent homology [137], the building of catalogs of similar atomic configuration [20] or the concept of "cloth" proposed by B. Schweinhart *et al.* [164]. In SiO_2, the structure is simple as chains of successive Si-O bonds form closed rings. These rings involve from three to eight Si-O bonds and have been extensively studied as they have distinctive Raman signatures [167, 140, 126, 145, 101]. They are believed to be at the origin of some of the unique vibrational and thermal properties of the glass, and their distribution has been used as a measure of relaxation in both experimental and numerical SiO_2 glasses. The multiplicity of possible structural topologies seen at the MRO, associated with chains of stresses frozen are at the origin of complex collective displacements involving from a few to hundreds of atoms such as Shear Transformation Zone [148] and Thermally Activated Relaxations [9, 91] that are respectively shear and temperature driven. In addition, at the MRO, mechanical heterogeneities are observed. These heterogeneities originate in the coupling between the disorder created at the SRO and the short-, medium- and long-range elastic coupling [180]. From a vibrational point of view, disorder creates typical vibrational modes observed at the MRO and not seen in crystals such as rotons or diffusons i.e. delocalized vibrations responsible for diffusive (rather than ballistic) propagation of wave packets [8, 22]. Furthermore, the MRO and the heterogeneities present at the MRO were proposed to be at the origin of the excess of vibrational modes seen at low frequencies called the Boson peak [85, 171, 120, 43, 26, 131] although this link is contested [180, 21].

Long-Range Order: the LRO denotes the order beyond 30 atomic bonds. At this distance, the disordered solid can be seen as a continuum and the properties that were still heterogeneous at the MRO converge to average effective values [180]. At this scale, the vibrations are low-frequency waves, whose spatial periods are large enough not to feel the disorder existing at the smaller scale and therefore approach plane waves typical of crystals and continuous homogeneous media.

It is the superposition of phenomena originating at the SRO, MRO and LRO that makes glasses so complex and interesting.

	LRO >30 interatomic bonds	MRO	SRO 1st shell of neighbors
Mechanical Properties	Continuum Mechanics Applies	Mechanical Heterogeneities	Local structure fixed by Inter-atomic forces
Vibrational Properties	Acoustic Waves & Low Frequency phonons	Diffusons & Rotons	Soft Modes, Optic-like Modes

Figure 2.2: Mechanical and vibrational properties of glasses as function of long-, medium- and short-range orders.

2.1.2 The Potential Energy Landscape of Oxide Glasses

The dynamics of a solid is governed by the underlying atomic forces and thus the potential energy. When thinking about the dynamics in a glass such as aging or energy dissipation, it is easier to consider the change of energy rather than atomic displacements. This is done by studying the topography of the Potential Energy Landscape (PEL), that is the static potential energy map of the configurational space of the system [73]. For a 3D system made of N particles, the PEL has 3N+1 dimensions corresponding to the 3N degrees of freedom plus the dimension required to represent the potential energy. At any given time, the system is represented by a point on the PEL, and the system dynamics corresponds to a continuous path on the PEL. In a crystal, the PEL can be easily apprehended as the numerous symmetries can be used to reduce the number of dimensions from 3N to a few. In a disordered solid, none of the dimensions are equivalent and the PEL resembles an assembly of fractal basins as represented in Fig. 2.3 [54, 82]. Since it is impossible to form a mental image or graphic representation of the 3N+1 dimensions of the PEL, it is always represented along an arbitrary vector of the configurational space. However, this reduction hides the extreme complexity that the PEL has in 3N+1 dimensions.

The points of interest on the PEL are the local energy minima called Inherent Structures (IS) and the saddle points. Every IS is surrounded by a basin of attraction whose volume contains all the points in the PEL that would lead to the IS during an energy minimization. At an IS, all the eigenvalues of the Hessian matrix are real and correspond to the eigenfrequencies of the system. On the other hand, the saddle points are unstable maxima separating two basins of attraction. Accordingly, at a saddle point, there is a negative eigenvalue corresponding to the negative curvature of the PEL. This imaginary eigenfrequency is associated to the eigenvectors along which the system falls if pushed. The energy differences between an IS and its surrounding saddle points are referred to as activation energies or energy barriers. The theory used to describe the evolution of the system on its PEL is the Transition State Theory (TST) first developed to describe reaction rates in chemical physics [60, 202]. The TST assumes that each change of basin

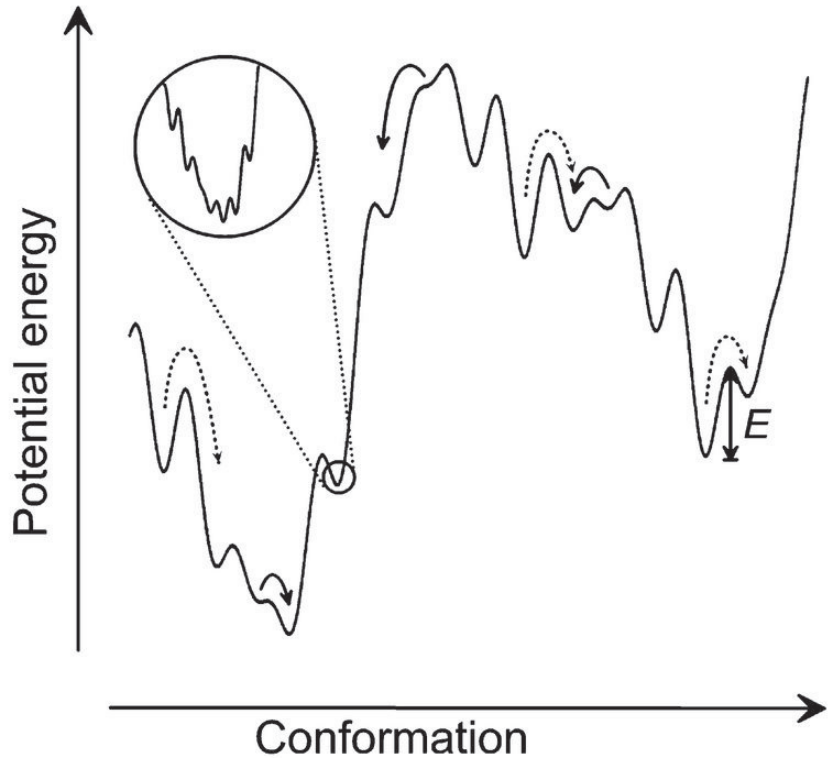

Figure 2.3: Potential energy along an arbitrary vector in the PEL. The bottom of each basin is an IS and each local maximum represents a saddle point.

is independent, i.e. the collective motion of the particles has time to fully decorrelate in-between transitions, which is true when the temperature is low compared to the height of the barriers. In this limit, the TST has proved that the rate at which a transition occurs follows an Arrhenius form: $\nu \propto \exp(-\frac{E_a}{k_b T})$ where E_a is the activation energy and T, the temperature of the system. At low T the system changes slowly, only exploring surrounding ISs, while at high T (in the liquid state), the system is free to go from meta-basin to meta-basin. Knowing the statistics of the energy barriers is key as sampling the jumps of the system from basin to basin is necessary to understand the dynamic properties of the glass, as will be done in Chap. 6.

A lot of work has been devoted to understand the link between the topology of the PEL and the structure of disordered solids [176, 199, 200]. At the SRO, the PEL can be approximated by the forces of the first shell of neighbors and thus looks like the atomic interaction in the direction of the bonds. However, at the MRO, the short-, medium- and long-range interactions quickly add up leading to a complex energy surface that cannot be captured by an analytic expression. Developing a better understanding of this link between PEL and structure at the MRO is the key to understanding the atomistic origin of the properties of a glass and being able to tailor them at the nanoscale [102, 189].

2.2 Energy Dissipation in Glasses

Energy dissipation (Q^{-1}), also called internal friction, is the irreversible conversion of mechanical energy into heat. It is at the origin of mechanical losses, acoustic attenuation and dielectric relaxation and is therefore an obstacle to the development of high-fidelity devices, such as micro- and nanoelectromechanical systems (MEMS/NEMS) [111, 86, 107] or sensitive gravitational wave detectors as mentioned in Introduction [161, 65, 74]. Energy dissipation can be defined in two different ways: from an attenuation or a cyclic dissipation point of view. From an attenuation point of view, dissipation arises from the decay in time of the amplitude of an initial deformation (e.g. plane wave), as $e^{-\Gamma t/2}\cos(\Omega t)$. In the Fourier space, this decay corresponds to a Lorentzian peaked on Ω with a width Γ, leading to the 1st definition of dissipation:

$$Q^{-1} = \frac{\Gamma}{\Omega}. \tag{2.1}$$

On the other hand, the cyclic dissipation point of view defines dissipation as the energy lost in a system under cyclic loading. A cyclic strain $\epsilon(\omega)$ imposed at frequency ω, will result in a stress $\sigma(\omega)$ related to $\epsilon(\omega)$ by a complex modulus $E(\omega)$ which can be written assuming linear response as

$$E(\omega) = E'(\omega) + iE''(\omega). \tag{2.2}$$

The real part of the modulus, E', represents the energy stored under cyclic loading, while the imaginary part, E'', represents the energy lost during a cycle [53], leading to the 2nd definition:

$$Q^{-1} = \frac{E''}{E'}. \tag{2.3}$$

Since $E(\omega)$ can also be written

$$E(\omega) = ||E(\omega)|| \left[\cos\phi + i\sin(\phi)\right], \tag{2.4}$$

a 3rd equivalent definition is

$$Q^{-1} = \tan\phi, \tag{2.5}$$

where ϕ represents physically the lag between the applied strain and the resulting stress. We note that while definitions 2.3 and 2.5 are strictly equal, they are not always equivalent to definition 2.1. This last equivalence holds in simple viscoelastic models, like Zener standard linear solid in the limit of small dissipation [139], but not necessarily in the general case.

2.2.1 Investigation Tools for Dissipation in Glasses

In glasses, the phenomena at the origin of energy dissipation are strongly frequency dependent, therefore, the tools used to study dissipation vary with the frequency range of interest.

From the Hz to the kHz, dissipation is studied through the response of the glass to mechanical signals. This method, called mechanical spectroscopy, is widely used in rheology, and mainly to study the viscoelastic behavior of polymers through the measurement of their complex modulus [63, 153, 39, 127]. In mechanical spectroscopy, a sinusoidal stress (or strain) is applied to the sample, and the resulting strain (or stress) is measured. Assuming a linear regime, if the material of interest shows dissipation at the frequency at which the load is applied, a lag will appear between the stress and strain, linked to dissipation as $Q^{-1} = \tan\phi$.

At intermediate frequencies, from the kHz to MHz, the study of dissipation is done through measurements of attenuation of vibrations in micro or nano-mechanical resonators made of the glass of interest. The sample, which is either in the form of a rod, a cantilever, a sphere or a thin film, is coupled with a resonant piezoelectric transducer possessing a high Q-factor [64, 67, 32, 95, 74, 144]. The lag between the driving signal and the resonance of the sample is measured using an electric setup, and dissipation is calculated once again as $Q^{-1} = \tan\phi$. Closely related, are Picosecond Ultrasonic (PU) techniques. In PU techniques, the driving signal is transmitted through a short acoustic pulse that enters the samples (usually thin) and decays while traveling in the medium [186, 150, 159]. Each time the pulse bounces on the surface of the medium, its amplitude is measured using a laser, from which the attenuation is obtained by fitting the exponential decay of the signal.

At higher frequencies, in the GHz and THz regimes, dissipation is studied experimentally through the dynamical structure factor, $S(q,\omega)$, as for instance in Refs. [187, 66, 156, 125, 155, 106, 12, 23, 13]. The dynamical structure factor expresses the spatial and temporal correlation existing in the movement of particles and is written as the space- and time-Fourier transform of the density-density correlation function [80]:

$$S(q,\omega) = \frac{q^2}{2\pi N\omega^2}\int \langle j(q,t)\cdot j(-q,0)\rangle\, e^{i\omega t}\,\mathrm{d}t. \tag{2.6}$$

It is probed experimentally using either Brillouin, neutron or inelastic x-ray scattering (IXS) that perform spectrographs i.e. slices of the dynamical structure factor at different wave-vectors q. At small wave vectors, the spectrum of $S(q,\omega)$ shows a peak at a well-defined frequency as illustrated in Fig. 2.4. This peak is fitted as a damped harmonic oscillators (DHO):

$$F(q,\omega) = \frac{\Omega(q)^2\Gamma(q)}{\left(\Omega(q)^2-\omega^2\right)^2+\omega^2\Gamma(q)^2}, \tag{2.7}$$

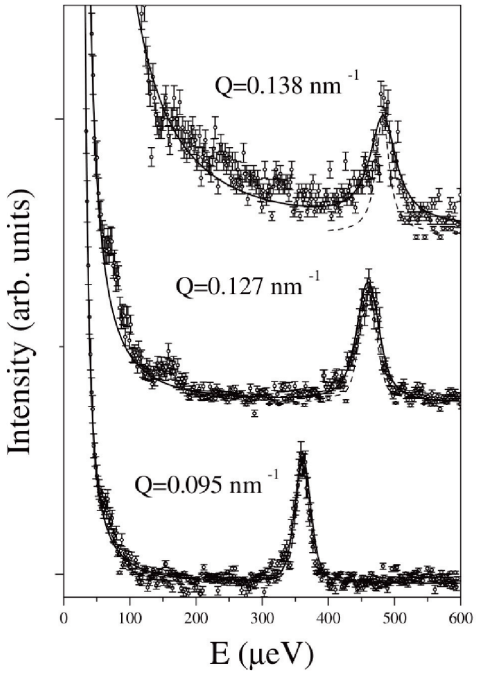

Figure 2.4: Brillouin spectra of vitreous silica at different wave-vectors. The continuous lines mark the DHO fits from which $\Omega(q)$ and $\Gamma(q)$ are obtained. Figure reproduced from Ref. [125].

from which the excitation frequency $\Omega(q)$, attenuation $\Gamma(q)$ and dissipation $Q^{-1}(q) = \Gamma(q)/\Omega(q)$ are obtained. The behavior of a DHO is directly related to its Q^{-1}, as for a given system, there exists a threshold above which the system is over-damped (the system doesn't oscillate when displaced and follows an exponential decay to equilibrium), and below which it is under-damped (the system oscillates when displaced but the amplitude of the vibrations decreases with time).

The above-mentioned techniques are adapted to probe the dissipative properties of glasses but are still indirect measurements of the phenomena at their origin. Indeed, in glasses, techniques such as neutron or X-ray scattering used traditionally to investigate the atomic order are limited due to the lack of periodicity. For example, X-ray scattering resolves appropriately only the first shell of neighbors before the signal decays into an homogeneous background. Progress has been made with the use of extended X-ray absorption fine structure (EXAFS) techniques, which gives precise first neighbor distances for each chemical element present in a glass [115, 17]. However, this technique only probes the SRO, while the MRO, the rigidity of the network and forces taking place between the different structural units are needed to understand the properties of the system. Therefore, the guesses on the atomic origin of dissipation stay theoretical until apparatus allowing atomic scale observation of the phenomena are developed. In addition, while mechanical spectroscopy, measurements in resonating samples and PU techniques probe dissipation directly, Brillouin scattering and IXS used at high frequencies, only provide an insight of the dynamical

structure factor from which the attenuation is obtained. As of today, it is not clear if these two sets of methods used at low and high frequencies measure exactly the same physical quantity. Settling this issue could be possible, for example by measuring dissipation at the same frequency using both Brillouin scattering and PU techniques, however these two methods do not cover the same frequency range.

To overcome these limitations, it is however possible to resort to atomic scale simulations made possible by the unstoppable developments in computer technology. The main method used to model solids and their dynamic properties at the atomic scale is Molecular Dynamics (MD), based on the numerical integration of the equations of motion [6, 7, 68]. However, MD requires a knowledge about the forces taking place between atoms. It is possible to obtain these interactions by solving the Schrödinger equation for each electron of each atom at each time step of the simulation. The development of *Ab initio*-MD based on the Born-Oppenheimer potential energy surface allows the successful usage of such a brute-force method. However, *Ab initio* methods are slow and and use complex approximations. In situations where the qualitative microscopic origin of a dynamic phenomenon or in situations where large systems or long simulations are needed, *Ab initio* methods are not appropriate. For such studies, classical MD is used. In classical MD, empirical or semi-empirical potentials describe the interaction between atoms, as will be detailed in Chap. 3. The idea behind classical MD is that if enough of the structural characteristics and properties of a solid are reproduced by a simple potential function, other properties of the material are likely to resemble the ones of the original solid.

Three methods have been implemented in MD to measure dissipation. The first one is mechanical spectroscopy [196, 192, 98, 203]. As done experimentally, the lag ϕ is measured between an imposed sinusoidal strain and the resulting internal stress, yielding dissipation. More details will be given in Chap. 5 where numerical mechanical spectroscopy will be implemented at the atomic scale. The second technique is based on the study of attenuation of waves propagating through the medium [184, 41, 71]. This is done by imposing a displacement in the form of a plane wave at $t = 0$, and following its attenuation as it is scattered by the disorder of the medium. With time, its amplitude deceases with an envelope proportional to $\exp(-\Gamma t/2)\cos(\Omega t)$ from which the attenuation coefficient, Γ, and resonance frequency, Ω, are obtained by a simple fit. The last method is the study of $S(q,\omega)$ as done experimentally using IXS, see for instance Refs. [75, 181, 45, 158, 171, 133, 120, 22, 21, 110]. Since the trajectories of the particles are known, the density-density correlation function and thus $S(q,\omega)$ can be computed numerically at fixed q. From these spectra, the attenuation is obtained fitting a DHO model as presented above. As mentioned in the previous section, dissipation computed using attenuation of plane wave and the $S(q,\omega)$ equals dissipation obtained using mechanical spectroscopy only when Eq. 2.1 and Eq. 2.5 are strictly equivalent, that is, at small dissipation in simple models.

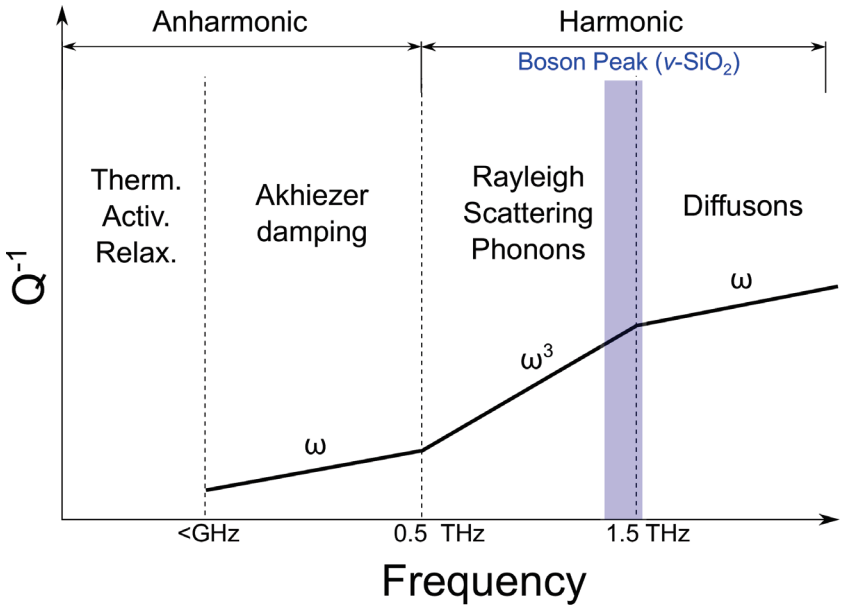

Figure 2.5: Source of dissipation and scalings of the dissipation as a function of frequency in silica [157, 12, 62, 71].

Numerical methods give the opportunity to simultaneously measure dissipation and observe the atomic motions or collective behaviors at its origin. In addition, being able to tune the parameters of the model helps revealing which features of the solid are important for the property considered. However, MD capabilities are strongly limited by the computational power of the machines on which it runs, in a large part due to the strong limitations both on their time scale with an integration step of the order of the fs, and on the number of particles involved. Therefore, direct measurement of dissipation at frequencies below the GHz or precise computation of the $S(q,\omega)$ for a 3D system containing more than a few thousand particles is for now out of reach. To compute dissipation at lower frequencies, and thus longer time scales, analytical models are used such as the TLS model which will be implemented in Chap 6.

2.2.2 Energy Dissipation in Oxide Glasses

While the source of energy dissipation in crystals can be traced back to crystalline defects [165], dissipation in oxide glasses can take many forms and may involve diverse phenomena depending on the temperature and frequency of interest, as pictured in Fig. 2.5.

From the Hz to MHz range, the frequency range of interest for many applications, dissipation in glasses arises from the attenuation of mechanical waves through their interactions with double-well potentials, understood through the framework of the Two-Level System model (TLS model) [91, 92, 142]. In the TLS model, the complexity of the PEL is represented as a distribution

of local double-well potentials of different asymmetry, Δ, and energy barrier, V. The dynamics of these double-well potentials is either: (1) Thermally controlled, at higher temperature (above a few Kelvin). In this temperature regime, the TLSs are referred to as thermally activated relaxation (TAR) since the transition from one well to the others is thermally activated. (2) Controlled by tunneling, below 10 K. If the kinetic energy is not sufficient for the system to hop above the energy barrier, atoms or group of atoms can tunnel through it.

When a mechanical wave passes through a glass, the solid is locally stretched or compressed which changes the relative positions of the atoms and therefore deforms the PEL. This deformation puts the TLSs out of equilibrium by changing the difference of energy, Δ, between the initial and final states. Since a relaxation time is needed for the system to respond to this energy change and come back to equilibrium, a lag appears between the mechanical wave and the response of the system. This lag is at the origin of dissipation.

In SiO_2 glasses, numerous studies aimed to quantify low frequency energy dissipation and expose the TLSs at its origin. As represented in Fig. 2.6, these works showed that dissipation in SiO_2 (solid and open circles) presents a plateau in the quantum regime, between 0.5 and 10 K while above 10 K, the majority of dissipation is due to TAR. A maximum of dissipation of $Q^{-1} \approx 10^{-3}$ has been observed at around 50 K before a drop of several orders of magnitude reaching $Q^{-1} \approx 10^{-7}$ at 300 K [95, 32, 106]. Atomic motion that could be at the origin of dissipation where identified in simulations by Reinisch *et al.* as oxygen centered displacements [146]. However this study focused on the quantum regime, thus the TLSs playing a role at room temperature have yet to be treated. In the present manuscript, TLS acting at room temperature will be studied in details in Chap. 6. It is important to note that the measurements presented in Fig. 2.6 have been carried out on bulk vitreous silica glasses. When deposited, for example with Ion Beam Sputtering (IBS) at low temperature, SiO_2 shows a lesser degree of relaxation. In IBS SiO_2 glasses, the study of dissipation showed from 10 to 300 K an almost constant plateau at $3 \cdot 10^{-3}$ with three maxima at 25, 160 and 250 K [123]. As IBS SiO_2 is less relaxed than its vitreous counterpart, it is more likely to present the same defaults than observed in numerical glasses quenched at high rates.

At higher frequencies (>GHz), dissipation in glasses arises from the attenuation of collective vibrational excitations [193, 125, 12], studied through the $S(q,\omega)$ as explained in the previous section. We saw in Fig. 2.4, that at low wave vectors (below 1-3 nm^{-1} in amorphous silica [85, 11, 110]), the spectrum of $S(q,\omega)$ shows a peak at a well-defined frequency. A sharp peak indicates a regime where the glass supports propagating vibrational modes, similar to crystalline phonons, but with a damping related to the finite width of the peak. For wave vectors larger than a few nm^{-1}, glasses exhibit a strong damping with an attenuation increasing rapidly with frequency: $\Gamma \propto \Omega^{\alpha}$, with $\alpha \sim 4$ in 3D seen in both experiments [66, 154, 11, 62] and MD simulations [162, 76, 133, 120, 43, 110]. Recently, a study revised these experimental data and used atomic

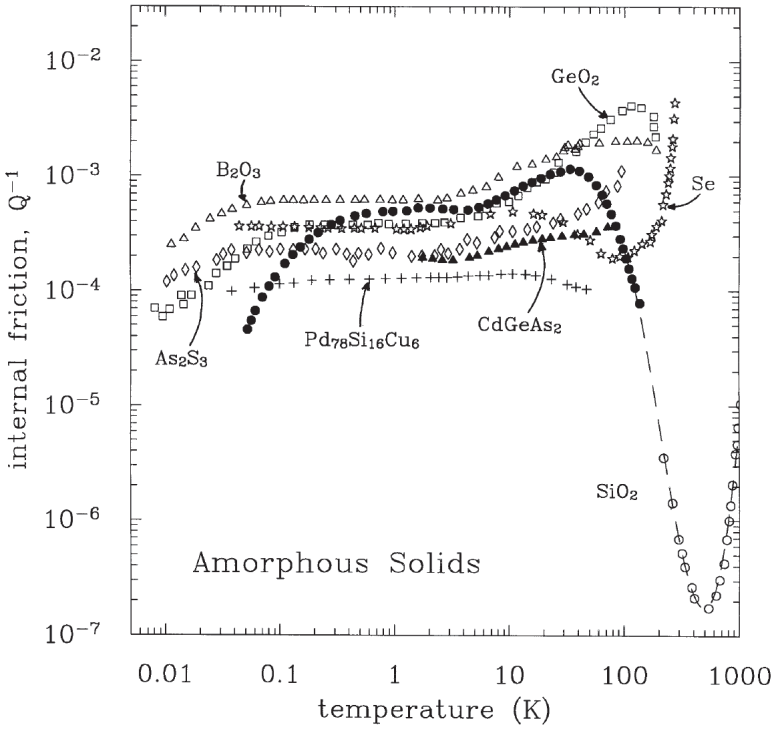

Figure 2.6: Internal friction for different amorphous solids. Dissipation for silica is measured at 100 kHz below 100 K (solid circles) and at 1.5 MHz above 100 K (open circles). Figure reproduced from Ref. [188].

scale simulations to identify a logarithmic correction: $\Gamma(q) = -q^{d+1}\ln q$ [71]. In this regime, damping is mainly of harmonic origin and is controlled by the structural disorder in the glass [45, 157, 158, 43]. More specifically, the acoustic vibrations undergo a Rayleigh type of scattering by the elastic heterogeneities in the glass that are correlated on the same nanometer scale as the wavelength of the acoustic vibrations [180, 191, 69, 198, 178, 120]. As a result of this strong scattering, the phonon mean free path, calculated as $l \propto 1/\Gamma$, decreases rapidly with frequency and becomes comparable to the wavelength of the vibrations. This equality between the wavelength of the vibrations and the mean free paths marks the limit between a regime where the propagation of energy is ballistic and a regime where it is diffusive. This limit is called the Ioffe-Regel (IR) limit and is reached when $\Gamma = \Omega/\pi$ [89]. Above this limit, the notion of phonon with a well-defined wave vector is inapplicable [8, 22]. In amorphous silica, the IR limit is reached at around 1~1.5 THz in both experiments and simulations [183, 163, 132, 11, 171, 22, 100, 110]. Interestingly, this region of strong damping is also the region leading to the boson peak [57, 31, 24, 55] that is also believed to originate from disorder. More details on dissipation at high frequency will be given in Chap. 5.

As illustrated in Fig. 2.5, there is an intermediate anharmonic regime, in the GHz frequencies,

where dissipation originates from a phenomenon called Akhiezer damping [4]. The theory is that when a solid is under loading, the eigenfrequencies it carries are slightly shifted in frequencies as the load deforms the solid. These shifts vary between the different eigenfrequencies as all eigenfrequencies are not affected in a linear manner. As a result, there are phonon-phonon relaxations through which the thermal energy is re-distributed between these new eigenvalues. This phenomenon will not be discussed in the rest of this manuscript, although it is an area of clear interest not thoroughly studied so far [25, 61, 98, 33].

2.2.3 Thermal Noise in Gravitational Waves Detectors

As mentioned in Introduction, applications in which dissipation plays a major role are gravitational wave (GW) detectors. As seen in Fig. 2.7, the source of dissipation in a GW detector are numerous as expected from the complexity of the device. The major sources are in order of increasing frequency : (1) Thermal noise, that is energy dissipation taking place in the coatings of the mirrors, (2) Angular control noise, arising from noise in the optical levers and wavefront sensors, (3) Suspension actuation noise, coming from dissipation within the suspension element of the mirrors [79], (4) Gas noise, that is the damping due to the friction with air or interaction of the beam with gas, (5) Quantum noise as the sum of the quantum radiation pressure noise, due to vacuum fluctuations, and shot noise [38], (6) Dark noise, due to thermally generated electrons flowing through the photodetectors.

We will focus here on the thermal noise, (1), coming from the mirrors coated with oxide-based glasses on which the laser is reflected. These coatings are as of today multi-layers of tantalum pentoxide glasses (Ta_2O_5) and silica (SiO_2) as shown in Fig. 2.8. These two materials were chosen for the contrast between their refractive indices leading to a very large reflectivity for the Bragg mirrors. While at room temperature at which LIGO and Virgo operate, SiO_2 presents a low of dissipation at $Q^{-1} \approx 10^{-7}$ shown in Fig. 2.6, the losses registered in Ta_2O_5 are $Q^{-1} \approx 10^{-4}$. Thus, it would be interesting to reduce the losses coming from this second glass. Recently, it has been discovered that doping Ta_2O_5 with TiO_2 leads to a reduction of internal friction in the range of frequencies of interest for GW detectors [121, 37, 74, 18]. However, the origin of this reduction remains obscure. Moreover, while the structure of silica is well-known, that of Ta_2O_5 and TiO_2-doped Ta_2O_5 glasses remains unclear. Experimental works have studied the MRO of Ta_2O_5 and its changes with the addition of Ti, and showed that doping impacts the MRO in a limited manner [17]. It should be emphasized that tantalum oxide glasses are of interest outside the field of GW detectors. For instance, they have recently been mixed with alumina to produce extremely strong glasses with excellent optical properties [149]. Tantalum oxides are also traditionally used in electronics due to their electric and dielectric properties [112].

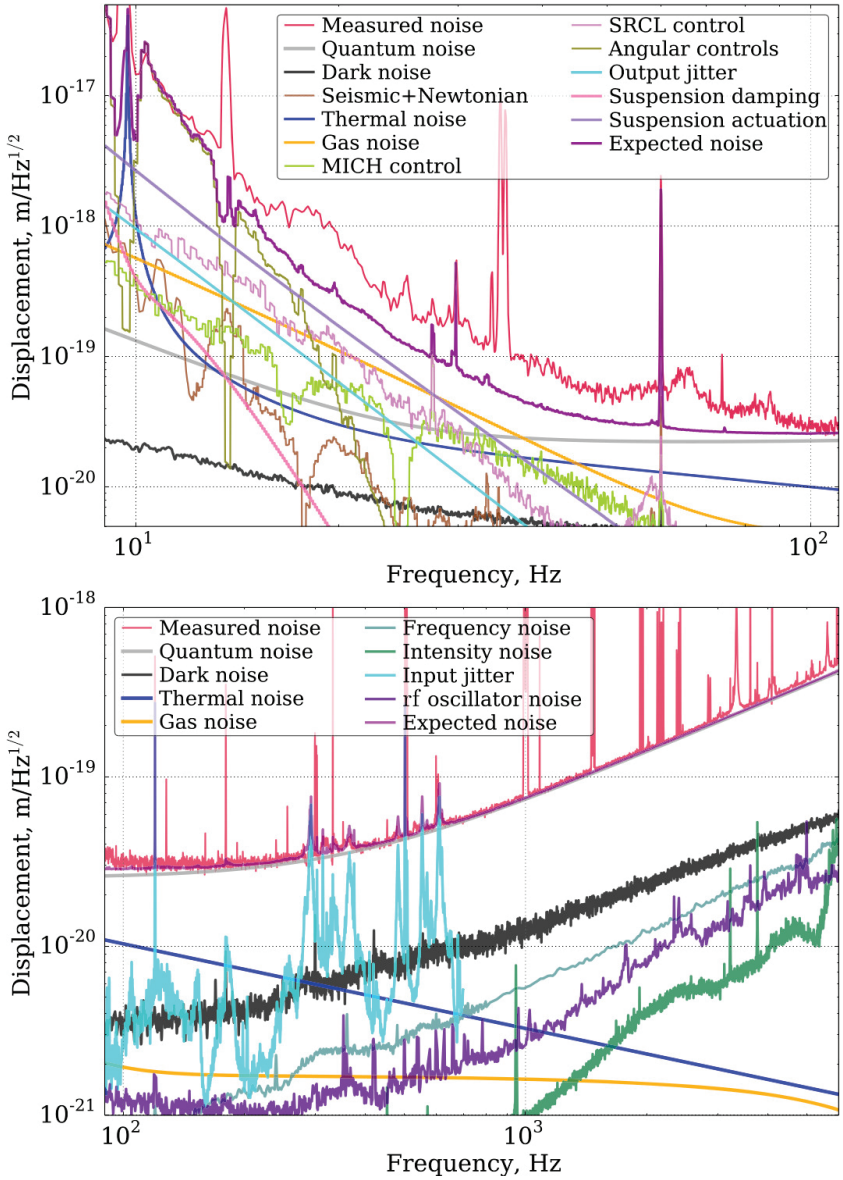

Figure 2.7: Summary of the sources of noise for the LIGO Livingston Observatory at low frequency on top and LIGO Hanford Observatory at higher frequency on the bottom. Figure reproduced from Ref. [124].

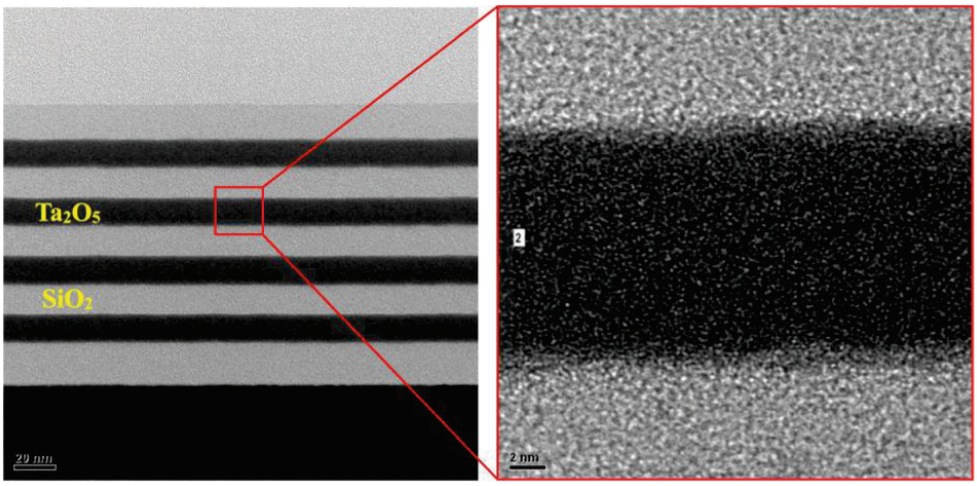

Figure 2.8: TEM micrographs of a thin film Ta_2O_5/SiO_2 multilayer. Figure reproduced from Ref. [201].

2.3 Conclusion & Scope

We saw that numerous works have been dedicated to oxide glasses such as SiO_2 and Ta_2O_5 but also, more generally, to the study of dissipation in glasses. These studies showed that dissipation has multiple sources, in part due to the complex multi-scale organization of glasses. Despite these efforts, the origins of dissipation in the different frequency ranges and at different temperatures are not fully understood and several issues and questions emerge from the above review:

(1) There is a lack of dissipation measurement in SiO_2 in the frequency and temperature range of interest for applications such as GW detectors. Many studies focused on low-T to understand the quantum regime and thermal anomalies present in glasses such as the above-mentioned plateau in dissipation [87, 91]. While others investigated dissipation at frequency >MHz where phenomena such as Akhiezer damping or Rayleigh scattering are, in addition to TARs, a source of dissipation [193, 106, 47]. The reason for this limited amount of measurements is probably the sensitivity required to follow closely the drop from $Q^{-1} \approx 10^{-3}$ to $Q^{-1} \approx 10^{-7}$ seen between 50K and 300K. Experimentally, the sensitivity is limited by losses coming from the experimental apparatus (and O-H impurities in the case of SiO_2) that contribute more to dissipation than SiO_2 itself [67]. In addition, the origin of this drop is not inderstood and it would be interesting to measure dissipation numerically and see if the maximum seen at 50 K and the drop that follows can be reproduced and explained.

(2) As experimental measurements are spatially averaging the properties of glasses, it is not yet possible to probe individual TAR and observe the atomic motion corresponding to a single event. However, these elementary mechanisms can be reproduced and observed using numerical tools,

therefore it would be interesting to observe to which elementary motions the TARs present in SiO_2 correspond and identify which of these TARs contribute significantly to dissipation.
(3) Still due to the averaging properties of experimental techniques, many hypotheses were used to take into account the wide variety of TARs present in glasses when fitting the TLS model to attenuation data. These approximations are mostly used to simplify the complicated link existing between the asymmetry of TLSs and the height of their energy barriers. For example, by considering that all TLSs are symmetric at low energy barriers [28, 193], that the asymmetry can be linked to the energy barrier through a polynomial function as in the Soft Potential model [94, 193], that the distribution of Δ and V are uncorrelated [188, 78] or simple function of temperature [187]. Even in numerical simulations, the use of hypothesis such as averaging the sensibility to the deformation of the TLSs was needed to overcome the limited statistical distribution obtained on small numerical systems and obtain dissipation curves in agreement with experimental measurements [78]. This raises the question of knowing if a reasonable value of dissipation can be obtained numerically without making assumptions in the application of the TLS model.
(4) At high frequency, above the IR limit, $S(q,\omega)$ shows a very broad peak, which results from the convolution of several excitations that cannot technically, nor should theoretically, be fitted as a damped harmonic oscillator (DHO), as recently mentioned in the conclusions of Refs. [29, 41, 13, 110]. To overlook this limitation gives improper values for dissipation. Then, how can we describe dissipation in glasses above the Ioffe-Regel limit where phonons are ill-defined and which happens to often be a region of high dissipation where the equivalence between Eq. 2.1 and 2.3&2.5 does not hold ?
(5) Doping Ta_2O_5 with TiO_2 leads to a reduction of dissipation at room temperature. However, the origin of this reduction remains unclear, even if recent works have shown the changes undergone by the MRO of Ta_2O_5 when doped with TiO_2 [189]. Atomic-scale models have been produced using first-principles [18] and empirical potentials [189], but the systems were small (<2,000 atoms) and the quenching rates used to produce the glasses from the liquid phase were very high (10^{13} K.s^{-1}). Therefore, a complete analysis of the poperties of large well-relaxed numerical glass of Ta_2O_5 and TiO_2 doped Ta_2O_5 are needed.
The present manuscript delves into these issues using equilibrium and non-equilibrium molecular dynamics applied to models of amorphous SiO_2, Ta_2O_5 and TiO_2-doped Ta_2O_5. The question of dissipation is addressed numerically and theoretically at the two extremes, low and high frequencies, as they are the two frequency ranges that can be reached using molecular dynamics. During this whole study, we made sure to use multiple large simulation cells to reach statistical significance. In addition, we privileged quenching rates as low as computationally possible to obtain glasses whose structures are as relaxed as possible.

CHAPTER 3

NUMERICAL METHODS

3.1 Molecular Dynamics

Molecular dynamics (MD) is the main numerical method used in the present study and the following sections will detail the technical elements implemented in the present MD code. The goal of MD is to predict the time trajectory of ensembles of atoms in interaction [7, 68]. In MD, time is discretized and at each time step, usually of the order of a femtosecond, the forces between atoms are computed from interatomic potentials. The displacement of each atom is then computed by solving Newton's equations of motion using a finite difference algorithm. In the present MD code, we will use the Velocity variant of the Verlet algorithm which calculates the position, r, and velocity, v, in a staggered way through the use of an intermediary velocity v':

$$v' = v(t) + \frac{dt}{2m} F(r(t)) \tag{3.1}$$

$$r(t+dt) = r(t) + dtv' \tag{3.2}$$

$$v(t+dt) = v' + \frac{dt}{2m} F(r(t+dt)) \tag{3.3}$$

One could expect higher order algorithms such as Runge-Kutta methods to be more precise than the $\mathcal{O}(dt^4)$ of the Verlet algorithm. However, unlike the Runge-Kutta methods, the error of the Verlet algorithm does not grow systematically on a large number of steps. In addition, the Verlet algorithm is time reversible and preserves the volume in the phase space of the system (symplectic integrator) [77].

3.1.1 Temperature constraints

When performing MD, it is common to impose constraints on the system to obtain a given temperature (T) or pressure (P). Computations are mostly carried out in the Microcanonical (NVE) and Canonical (NVT) ensemble in which entropy and free energy are the thermodynamic potentials. In an equilibrium MD simulation, integrating the equations of motion insures the NVE ensemble. But, in situations where mechanical energy is transformed into heat (e.g. when a deformation is applied), it may become necessary to control the resulting increase in temperature. To do so, a thermostat is used.

In the present work, three thermostats were implemented: the Andersen thermostat based on re-setting the velocity of a fraction of the atoms from a Maxwell distribution each n time step, the Nose-Hoover thermostat where a virtual mass determines the strength of interaction between a bath at the wanted temperature and the system and finally, the Langevin thermostat. This last thermostat is based on the stochastic Langevin dynamics and aims to mimic the interaction of the atoms with a bath composed of smaller particles having the desired temperature. This is done through the addition of two terms to the equations of motion:

$$m\ddot{r} = F - m\gamma\dot{r} + F_{th}. \tag{3.4}$$

The second term on the RHS, $m\gamma\dot{r}$, where γ is referred to as Langevin friction and has the unit of a frequency, describes the friction that the atoms sustain when moving through the bath. The third term, F_{th}, is a random force whose correlation time is infinitely short (white noise). It represents the collisions between the atoms and the numerous particles constituting the bath, each collision changing slightly the momentum of the atoms. The Langevin friction, γ, is related to the white noise, F_{th}, through the fluctuation-dissipation theorem [97] such that:

$$\langle F_{th}(t).F_{th}(t')\rangle = A\delta(t-t'), \tag{3.5}$$

where

$$A = 2m\gamma k_b T. \tag{3.6}$$

The use of the Langevin thermostat presents an interest over the Andersen or the Nose-Hoover thermostats as it allows the development of analytical calculations from the equations of motion (as it will done in Appendix A).

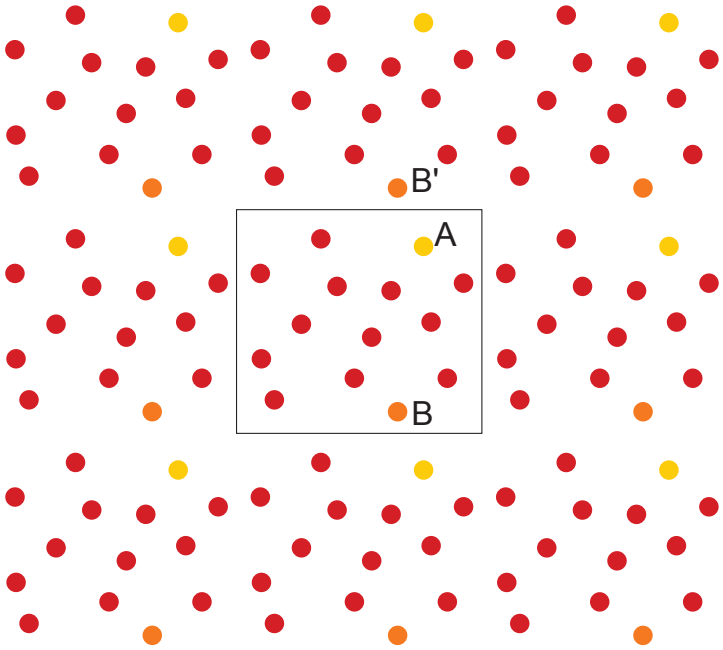

Figure 3.1: Schematic representation of periodic boundary conditions in 2D. The particle A in the original cell interacts with the particle B via its image B' due to the PBC.

3.1.2 Periodic Boundary Conditions

In the present study, we will consider 3D parallelepipedic cells of length L of the order of a few nanometers containing a few thousands particles. In such small systems, the boundaries represent a large part of the sample, and the surface properties dominate the properties of the bulk glass. In order to avoid surface effects, we used periodic boundary conditions (PBC) in the X, Y and Z direction. PBC are used to simulate an infinite system formed by the repetition in space of the original cell as represented in Fig. 3.1. At every time step, the position of all particles is brought back in the initial cell through the transformation:

$$r_i = \begin{cases} r_i, & \text{if } 0 < r_i < L \\ r_i - L, & \text{if } r_i > L \\ r_i + L, & \text{if } r_i < 0 \end{cases} \tag{3.7}$$

To compute the vector between particles, the minimum-image convention is used:

$$r_{ij} = \begin{cases} r_j - r_i, & \text{if } -\frac{L}{2} < r_j - r_i < \frac{L}{2} \\ r_j - r_i - L, & \text{if } r_j - r_i > \frac{L}{2} \\ r_j - r_i + L, & \text{if } r_j - r_i < -\frac{L}{2} \end{cases} \tag{3.8}$$

A particle at the border of the cell will interact with particles at the opposite of the original cell as if they were close to it, as represented by the atoms A and B' in Fig. 3.1.
Under PBC, the original cell acts similarly to the primitive cell of a crystal due to its virtual repetition in space. It is therefore important, when studying glasses, to consider a system "large enough" because if the system contains less than a hundreds of atoms, the amorphous solid surrounded by its virtual images will present the properties of a crystal (e.g. define peaks at long-range in the pair distribution function). This is especially true for compounds presenting large primitive cell such as crystalline Ta_2O_5 [113, 83].

3.1.3 The SLLOD Equations of Motion

A MD simulation in which an external field is applied to the system is referred to as a Non-Equilibrium Molecular Dynamics (NEMD). In the case of a displacement field, the basic Verlet algorithm cannot be used since it does not account for the displacement added to the trajectories by the field. A set of equations, referred to as SLLOD equations, has been developed to integrate the equation of motion in this case [7, 58]:

$$\dot{r} = \frac{p}{m} + r\nabla u \tag{3.9}$$

$$\dot{p} = F - p\nabla u, \tag{3.10}$$

where r and p represent the position and momenta vector in the laboratory reference frame. $\dot{r}$ is the time derivative of the position, but is not strictly v as can be seen from Eq. 3.9. u is referred to in the liquid community as the streaming velocity (such as in a laminar flow) and represents the deformation field applied to the solid. Therefore, $r\nabla u$, in the first equation, describes the drag motion atoms undergo due to the imposed displacement field while $p\nabla u$, in the second equation, expresses the additional momenta carried by the atoms due to the external field.
In the present study, only strain fields will be used through changes of the cell size and shape as, for example, in the case of hydrostatic deformation. In this context, the SLLOD equations will be written

$$\dot{r} = \frac{p}{m} + \dot{\epsilon} r \tag{3.11}$$

$$\dot{p} = F - p\dot{\epsilon} - \gamma p + F_{th}, \tag{3.12}$$

where ϵ is a deformation tensor (in the case of a hydrostatic deformation, only the diagonal term ϵ_{xx}, ϵ_{yy} and ϵ_{zz} are none zero). As mentioned in the previous section, an imposed deformation will induce a heating of the system that is controlled, in the present study, with a Langevin thermostat of frequency γ. From this set of equation, a second-order differential equation of

motion can be obtained. Indeed, deriving Eq. 3.11 with respect to time, we obtain

$$\dot{p} = m\ddot{r} - m\dot{\epsilon}\dot{r} - m\ddot{\epsilon}r. \tag{3.13}$$

Then, replacing p and $\dot{p}$ in Eq. 3.12 gives the equation of motion that will be integrated in Chap. 5:

$$m\ddot{r} = F + mr(\ddot{\epsilon} + \dot{\epsilon}^2) - m\gamma(\dot{r} - \dot{\epsilon}r) + F_{th}. \tag{3.14}$$

The term $mr\ddot{\epsilon}$ is the acceleration due to the drag motion while $(\dot{r} - \dot{\epsilon}r)$ is the velocity in the moving frame of reference, showing that the thermostat takes properly into account the velocities due to the deformation. In the rest of the present study, only deformations of small amplitude will be imposed, therefore the second order term $mr\dot{\epsilon}^2$ is small and will be ignored.
When performing analytical calculations in the harmonic approximation for a solid under deformation, we will encounter the need to compare the position of an atom $r_i(t)$ to its equilibrium position R_i. However, under deformation, R_i refers to a position in the undeformed cell while $r_i(t)$ refers to a position in the cell under loading $\epsilon(t)$ (and thus of different size $L(t)$). This creates an issue when computing distances using the minimum image convention . To overcome this limitation, we will define the position of an atom i as the sum of two terms:

$$r_i(t) = (1 + \epsilon(t))R_i + x_i(t). \tag{3.15}$$

where R_i represents the equilibrium position of atom i in the initial undeformed cell while $x_i(t)$ is the non-affine displacement in the current cell. In the harmonic approximation, we will express the quantities (force and energy), considering only difference between different atoms in their reference positions ($R_{ij} = R_j - R_i$) and non-affine displacements ($x_{ij} = x_j - x_i$) (more details will be given in Chap. 5).

3.1.4 Interatomic Potentials

In order to use the Verlet algorithm described above, the forces present in-between atoms have to be known. In classical MD, these forces are computed using empirical or semi-empirical potential functions that take as input the position of the atoms. The constant parameters of the potential functions are fitted on *ab initio* calculations or experimental data such as pair distribution functions, angle distributions and elastic constants [7]. The systems obtained using these potentials are simili systems that are approximations of the original medium. The most generic of these potentials is the Lennard-Jones pair potential used to describe Van der Waals interactions in neutral systems. A slightly more complex potential, that will be used in the rest

of the present study, is the van Beest, Kramer, and van Santen (BKS) potential. This potential was developed in 1990 to describe silica and aluminophosphates and is based on both *ab initio* simulations and experimental data [194]. In its original form, it reads:

$$V(r_{ij}) = \frac{q_i q_j e^2}{r_{ij}} + A_{ij}\exp(-B_{ij}r_{ij}) - \frac{C_{ij}}{r_{ij}^6}, \tag{3.16}$$

The first term represents the Coulomb interaction between atoms i and j carrying the fractional charges q_i and q_j respectively. The second term represents the short-ranged Pauli repulsion and the third represents the attractive van der Walls interaction, these last two terms being known as the Buckingham potential. A known drawback of using the classic form of the Coulomb interaction, is its slow convergence as we consider interactions between an initial atom and atoms further and further away. In addition, the Coulomb term decreases in $1/r$ and the sum of long range interactions can diverge in charged systems [7]. A solution to the slow convergence is known as the Ewald summation technique [59], where the sum of all Coulombic interactions is decomposed into a real space and a Fourier part. However, we will prefer here another method less computer intensive, called the Wolf truncation, proposed by Dieter Wolf in Ref. [204]. The Wolf truncation approximates the Coulomb interactions as:

$$\frac{1}{r_{ij}} = \begin{cases} \left(\frac{1}{r_{ij}} - \frac{1}{r_{cw}}\right) + \frac{1}{r_{cw}^2}(r - r_{cw}), & \text{if } r < r_{cw} \\ 0, & \text{if } r > r_{cw} \end{cases} \tag{3.17}$$

where r_{cw} is a cut-off for the Coulomb interaction. For SiO_2, values as small as $r_{cw} = 10.17$ Å are enough for this approximation to give good results [34]. The Wolf truncation can be understood physically as the screening of distant charges by the closest ones. We estimate that, although the present systems are relatively small, our implementation of the Wolf truncation allows to gain about a factor 2 compared to the Ewald summation. In addition, it leads to analytical pair potentials, which simplifies the computation of Hessian matrices.

To further optimize the potential, we used the smoothing function and additional repulsive parts proposed by Carré *et al.* [34] and already employed in Refs. [118, 96] to model SiO_2 glasses. The smoothing function allows to use a short cut-off for the close range interactions by making sure that the potential goes smoothly to zero as $r \to r_c$. For SiO_2, r_c was set to 5.5 Å. The additional repulsive parts at small range ($r < r_{c,Rep}$) make sure that the atoms do not collapse together at

	A_{ij} (eV)	B_{ij} (Å^{-1})	C_{ij} (eV.Å^6)	$r_{c,Rep}$ (Å)
O-O	1388.773	2.7601	175.0	1.75
Si-O	18003.7572	4.8733	133.5381	1.27
Si-Si	872360308.1	15.221	23.299907	0.0

Table 3.1: Values of the parameters for the BKS potential used to model glassy SiO_2.

high pressure or high temperature. With these two additions, the BKS potential reads:

$$V(r_{ij}) = V_{coul}(r_{ij}) + V_{Buck}(r_{ij}) + V_{Rep}(r_{ij}) \tag{3.18}$$

$$V_{coul}(r_{ij}) = q_i q_j e^2 \left[\left(\frac{1}{r_{ij}} - \frac{1}{r_{cw}} \right) + \frac{1}{r_{cw}^2}(r - r_{cw}) \right] G_{cw}(r_{ij}) \tag{3.19}$$

$$V_{Buck}(r_{ij}) = \left[A_{ij} \exp(-B_{ij} r_{ij}) - \frac{C_{ij}}{r_{ij}^6} - \left(A_{ij} \exp(-B_{ij} r_c) - \frac{C_{ij}}{r_c^6} \right) \right] G(r_{ij}) \tag{3.20}$$

$$V_{Rep}(r_{ij}) = \left(\frac{D_{ij}}{r_{ij}} \right)^{12} + E_{ij} r_{ij} + F_{ij} \tag{3.21}$$

where

$$G_{cw}(r_{ij}) = \exp\left(-\frac{\gamma_{cw}^2}{(r - r_{cw})^2} \right) \tag{3.22}$$

$$G(r_{ij}) = \exp\left(-\frac{\gamma^2}{(r - r_c)^2} \right) \tag{3.23}$$

The parameters used to model SiO_2 can be found in Tab. 3.1 while D, E, F are adjusted on the first and second derivatives of the potential to be continuous when $r \to r_{cw}$. The potential energy as a function of r_{ij} for this set of parameters and a cut-off at $r_{cw} = 10.17$ Å can be seen in Fig. 3.2.

Other potentials exist to describe SiO_2 such as Tersoff potential based on the concept of bond order [185], the fluctuating charge potential with a Morse stretch term for the short-range interactions proposed by Demiralp, Cagin, and Goddard (DCG) [46], and a polarized force field proposed by Tangney and Scandolo (TS) [177]. Despite its weakness in the reproduction of the vibrational density of states (especially in the quartz phase) and thus thermal conductivity [205], the present BKS potential reproduces accurately the structure of amorphous SiO_2 [169] and is less computer intensive than Tersoff potential. The simplicity of its form and convenient extension to other oxide glasses made us choose this potential as a unifying scheme for the present study.

To model Ta_2O_5 and TiO_2 glasses, we used a modified version of the above mentioned BKS potential that includes an additional Morse term proposed by Trinastic *et al.* in Ref. [190] to

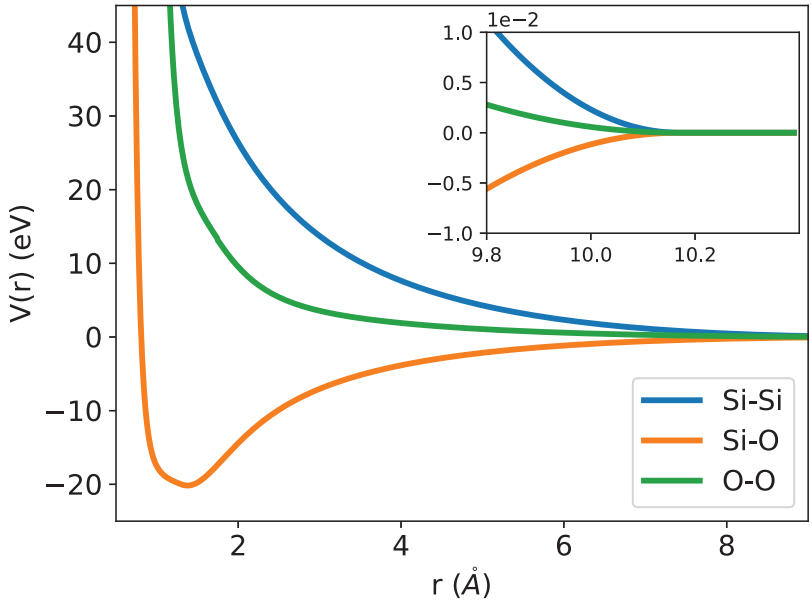

Figure 3.2: BKS potential for SiO_2 as a function of r_{ij} using the parameters of Tab. 3.1. The inset shows a close up of the region around $r_{cw} = 10.17$ Å.

represent the covalent interactions between Ti-O and Ta-O:

$$V(r_{ij}) = V_{coul}(r_{ij}) + V_{Buck}(r_{ij}) + V_{Rep}(r_{ij}) + V_{Morse}(r_{ij}) \tag{3.24}$$

$$V_{Morse}(r_{ij}) = H_{ij}\left(1 - \exp\left(-a_{ij}(r_{ij} - I_{ij})\right)\right)^2 \tag{3.25}$$

The parameters used to model Ta_2O_5 and TiO_2 are reproduced from Ref. [190] and presented in Tab. 3.2. They were obtained by fitting crystal lattice parameters and elastic constants. Titanium oxide contains four-folded Ti atoms in the rutile, anastase and brookite crystalline forms but are five- or six-folded in amorphous TiO_2. Thus, two sets of parameters exist to model Ti-O interaction. In the present study, the set of parameters promoting five- and six-folded atoms was chosen, in agreement with experimental results showing that Ti atoms have similar coordination as Ta atoms in amorphous Ta_2O_5-TiO_2 [17]. After thorough testing, the cut-off radius of the potential, r_{cw} was set to 15 Å, larger cut-offs leading to similar glass structures. The cut-off of the short-range of the potential was set to 5.5 Å, giving an equilibrium density consistent with experiments, as will be mentioned in Chap. 4. The resulting potential energy curve can be seen in Fig. 3.3.

	A_{ij} (eV)	B_{ij} (Å^{-1})	C_{ij} (eV.Å^6)	$r_{c,Rep}$ (Å)	H_{ij} (eV)	a_{ij} (Å^{-1})	I_{ij} (Å)
Ta-O	10067.01	7.5815	6.05	0.4308	0.3789	1.6254	2.5447
Ti-O	5505.12	4.4385	20.0	0.87	0.5478	1.9	1.96

Table 3.2: Values of the parameters for the M-BKS potential to model Ta_2O_5 and TiO_2 glasses.

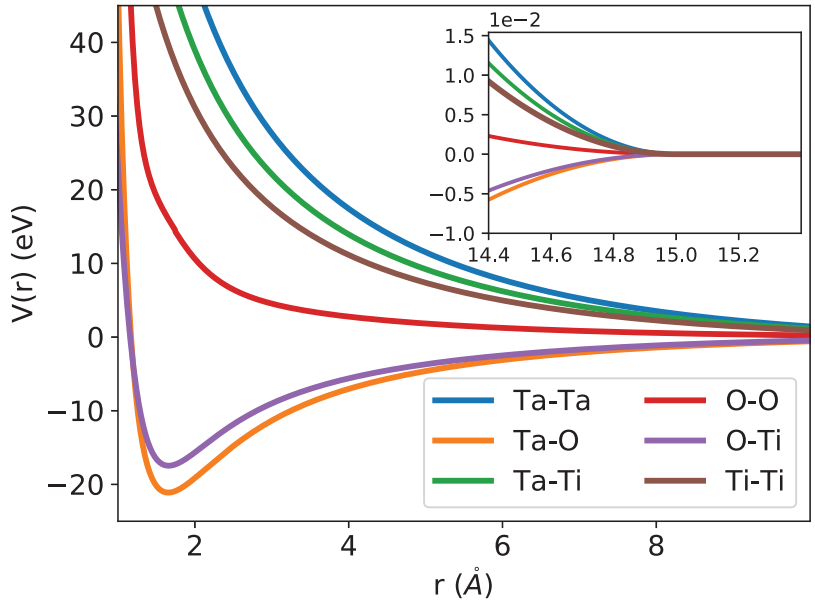

Figure 3.3: M-BKS potential for Ta_2O_5 and TiO_2 as a function of r_{ij} using the parameters of Tab. 3.2. The inset shows a close up of the region around $r_{cw} = 15$ Å.

3.2 Synthesizing Glasses

As mentioned in Sec. 2, glasses result from the rapid cooling of a melt, a cool down so fast that it does not give enough time for the atoms to form an energetically optimal arrangement (ultimately, the crystal positions). Since the structure of glasses is not based on a unit cell, we have a priori no idea of how the atoms should be ordered to obtain a glass. To overcome this limitation, the simplest solution is to mimic nature and start from a melt. To create a melt, it is sufficient to place atoms at random in the simulation box with the desired density and stoichiometry. A random placement of the atoms will result in a high potential energy quickly transformed into kinetic energy sufficient to melt the system. It is also possible to start from the crystalline structure of the compound if it exists; however, considering the high starting temperatures in the present study (until 15.000 K during the first time steps), it does not present any advantage compared to the random placement since all previously existing structural correlations would be lost in the melting process. The second step is to cool down the melt fast enough to avoid crystallization. Fortunately, the time scales reached in MD allow only quench rates going from 10^{15} to 10^9 K/s

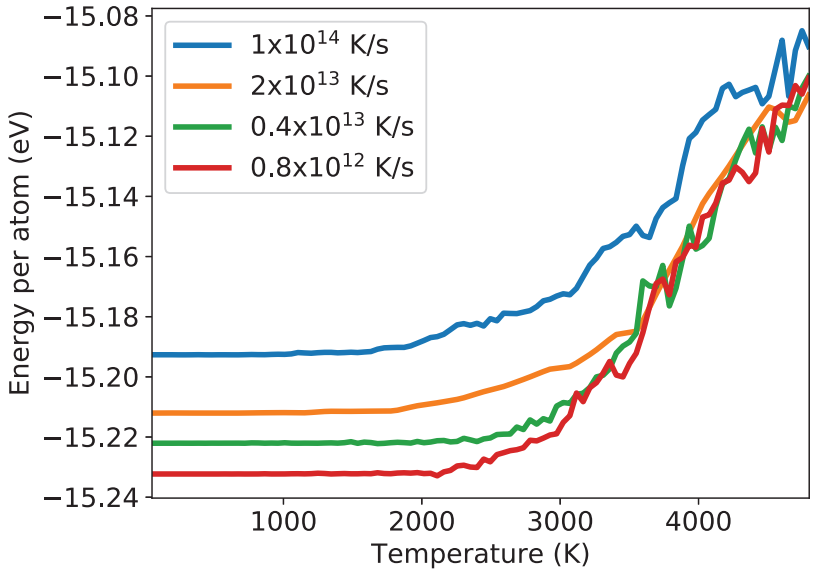

Figure 3.4: Potential energy of the underlying inherent structures during the quench of SiO_2 melts from 5000 K to 0 K at four different quenching rates. The SiO_2 melts contain 3,000 atoms for a cell size $L = 34.77$ Å.

at best. These are several order of magnitudes faster than the fastest quench rate produced experimentally (10^5 K/s [50]) and almost always fast enough to avoid crystallization (except for mono-atomic LJ systems).

In the present study, all samples were generated following this method. Starting from a melt containing several thousand particles, the system is cooled down to 0 K using a thermostat at a constant quench rate. For some simulations, the cell size was also dynamically adjusted to maintain zero internal pressure during cooling and obtain the equilibrium density of the potential. When the temperature of the system is about to reach 0 K, the energy of the system is minimized using damped dynamics to ensure that the system is in an IS. This minimization is performed by running a standard NVE simulation where the velocities are set to zero whenever the sum on all the atoms of $\vec{v} \cdot \vec{F} < 0$, that is, each time the system ascends the PEL. The minimization continues until the sum of the atomic forces passes under 10^{-4} eV/Å.

Fig 3.4 represents the potential energy of a SiO_2 system minimized at regular intervals (to ensure that the system is in an IS) during cooling. This figure shows that when the temperature decreases, the potential energy decreases also until the system gets trapped in a basin from which it cannot escape due to its lack of kinetic energy [160]; this regime can be seen by the almost constant energy at low temperature and is dominated by thermally activated relaxation that will be the point of interest of the next section. The quench rates were varied from 10^{14} K/s to 10^{11} K/s, slower quenching allowing to go deeper in the PEL, reaching less energetic states. The

decrease of energy at 0 K with the lowering of the quenching rate is due to the better ordering of the atoms as they are given more time to rearrange. For example, in SiO_2 glasses, it is common to find five folded Si atoms when the system is quenched at 10^{14} K/s whereas they are very rare at 10^{11} K/s.

3.3 Exploring the Potential Energy Landscape

In a disordered system, one has a priori no knowledge about the structure of the PEL around the current IS. The only information available at an IS is its potential energy and the Hessian matrix whose eigenvalues give the curvature in the 3N directions of the PEL. The first step to explore the PEL is to leave this initial IS to find the energy barriers and new IS surrounding it. To do so, two different methods were used.

3.3.1 Finding new inherent structures using Molecular Dynamics

The first technique consists in using MD to generate thousands of trajectories at constant temperature starting from a known IS, hoping to see thermally activated events during the time of the simulations. To generate a trajectory, random velocities are assigned to the atoms at $t = 0$ before the system is let to evolve at constant energy. Along each trajectory, the energy is minimized every 40 fs (40 time-steps) and the current IS is compared to the initial IS. If the system is back in the initial IS, the run continues until a new configuration is obtained or until the run reaches 10 ps. Once a sufficient number of final configurations are obtained, they are compared using a distance criterion of 1.0 Å, low enough to eliminate duplicates, giving a list of unique configurations.

To better visualize the present technique, we represented in Fig. 3.5 the variations in potential energy of a SiO_2 glass during a MD run at constant temperature (300 K). The potential energy curve is obtained by cloning every 10 time-step the current configuration and minimizing its energy (after which the original simulation continues at 300 K). The lower plot represents the norm of the distance between the actual and initial IS, showing that each energy step represents a change in the atomic positions and thus a change of IS (i.e. change of basin caused by thermal activation). In the present sequence of jumps, the system explores three different states: the initial one, and two others that are explored twice each. It is interesting to notice that the system comes back to its initial state after exploring a more energetic state, possibly because the initial IS is the lowest energy state in this region of the PEL. Another interesting observation is that the distance between the initial and current ISs is not necessary correlated with the height of the energy barrier overcame to be in the current IS. For example, the first transition shows a smaller barrier than the third, but larger atomic displacements.

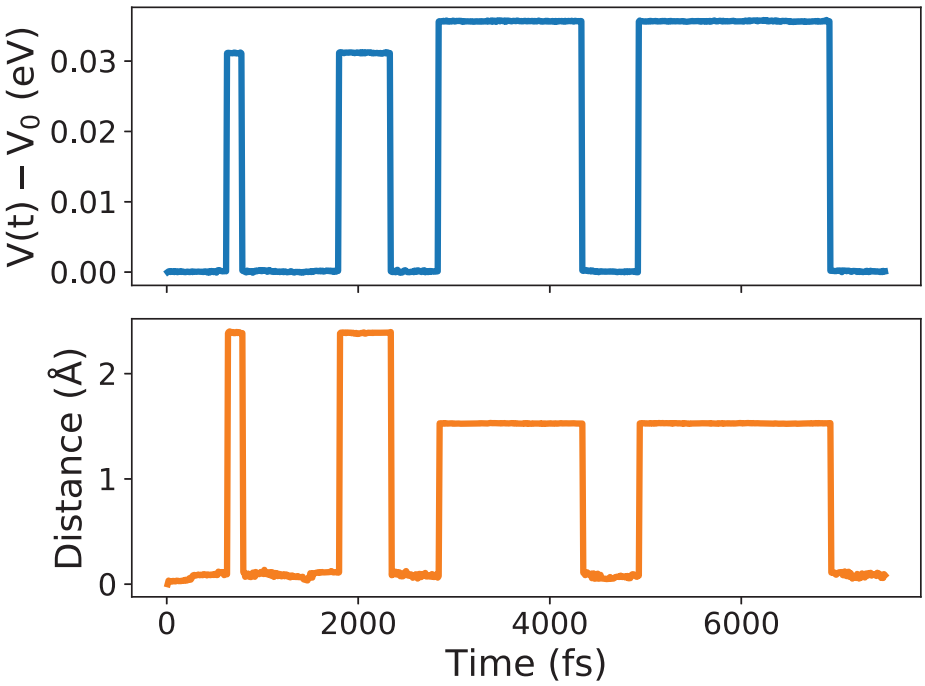

Figure 3.5: Upper curve: time evolution of the potential energy of the whole simulation cell with respect to the potential energy of the initial state V_0. Lower curve: time evolution of the norm of the distance vector between the current atomic configuration and the initial one. Both curves are obtained through a MD run performed at constant temperature (300 K) during which energy is minimized every 10 fs using a damped dynamic.

The drawback of this technique is that the probability of jumping above a barrier of given energy is a function of the temperature at which the simulation is run. A temperature too low will not allow the system to pass any barrier but if one tries to increase the temperature to probe all surrounding barriers, the system will melt. In addition, as mentioned in Sec. 2, the probability of passing a barrier of height V is proportional to $\exp(-V/k_bT)$, as a result, most of the searches end up passing through the same low energy barriers. However, this method has two strong advantages compared to the ART method that will be presented next: (1) It follows a physical dynamics and probes paths in the PEL along which the system goes naturally. (2) As a direct consequence, it is good for probing low energy barriers and close local minima that influence the material properties at room temperature and below.

3.3.2 Nudged Elastic Band Method

Once a consequent list of new IS is obtained using MD, we are interested in finding the minimum energy pathway linking the original IS to the new IS, in order to identify the saddle configuration and its energy to compute the corresponding energy barrier. To do so, we used the Nudged Elastic

Value	Parameter
51	Number of NEB images
0.01 eV	Force threshold for the NEB minimization
1.0 eV/Å	Virtual spring constant
5	Number of time step after which the vector normal to the spring chains is updated

Table 3.3: Parameters of the NEB method used in the present study.

Band (NEB) method [129, 130] through one of its derivative: the Climbing Nudged Elastic Band (C-NEB) [81]. The NEB method works as follow: n atomic configurations are created as linear combinations of the initial and final IS. These intermediate images can be seen as regularly spaced snapshots along the path that the atoms have to follow in order to reach the final IS as represented in Fig. 3.6. Initially, the linearly spaced images have no reason to be the path of minimum energy, therefore, an iterative algorithm is used: each of the n images is linked to the two images surrounding it with virtual springs of stiffness k. Thus, the force acting on each image comes from these springs and from the inter-atomic forces. The minimization algorithm acts by moving the images on the PEL in order to minimize both of these forces. To do so, the atomic forces acting on the images are projected on the normal to the spring chain, in a process referred to as "nudging". Nudging allows the images to find the path of minimum energy while the springs, whose forces are parallel to the spring chain, are used to maintain a constant separation between the images. Once the forces acting on the chain of images pass below a chosen threshold of 0.01 eV, the images are considered to be on the minimum energy pathway. A drawback of this method is that most of the time, none of the n generated images end up at the saddle point. To overcome this limitation, the image with the highest initial energy is selected and the force acting on it is defined as the force due to the potential with the component along the spring chain inverted. The force acting on this image is thus biased to climb the PEL until it reaches the saddle point. In addition, this maximum energy image is not affected by the spring forces as it would drive it away from the saddle point. The resulting climbing motion gave the name of this method: Climbing NEB.

The parameters used for the C-NEB in the present study are presented in Tab. 3.3. The number of images was chosen to have a smooth description of the minimum energy pathway in the PEL while having an image at the saddle point. The spring constant is chosen rather stiff as to have a constant separation between images.

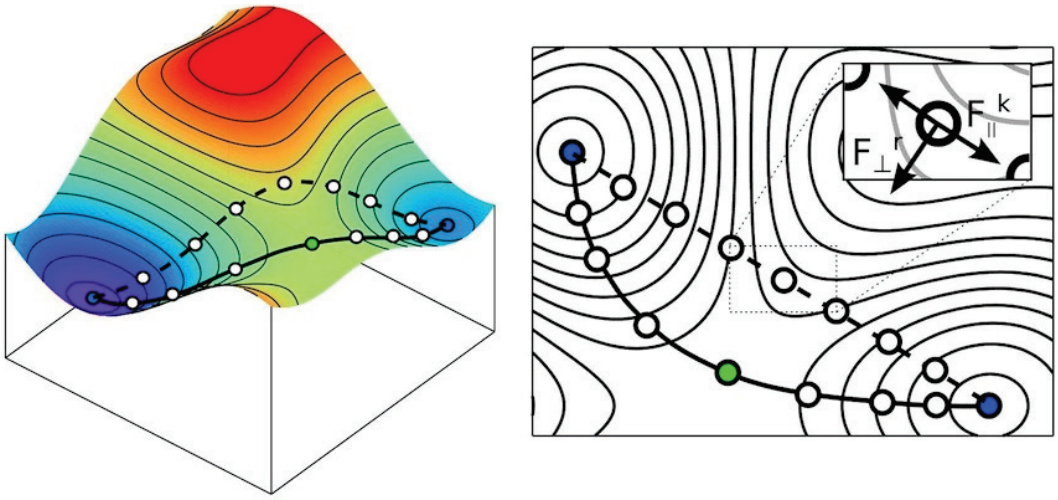

Figure 3.6: NEB method on a system with 2 degrees of freedom. The circles linked by a dashed line represent the initial images while the ones linked by a continuous line are obtained once convergence is reached. The saddle point is represented by a green circle. The inset of the right figure shows the atomic forces $F_{\perp}^{k}$ normal to the chain and the forces of the chain itself $F_{\parallel}^{r}$ parallel to the chain. Figure reproduced from Ref. [2].

3.3.3 The Activation Relaxation Technique

The second method we used to explore the PEL is the activation relaxation techniques (ART) developed in 1996 by N. Mousseau and G. T. Barkema [14, 134], and implemented in the present work in its more recent version: ART Nouveau [116], which includes the Lanczos algorithm and curvature calculations. The ART algorithm is a two step process:

(1) The activation step: starting from a known IS, a cluster of atoms is moved along a random displacement vector, $\vec{U}$, in the PEL, which results in an increase of potential energy. The whole system is then allowed to relax for a limited number of steps in the hyperplane normal to $\vec{U}$, to ensure that the system follows the slope leading to a saddle point instead of exploring regions of high energy. This cycle of displacements along $\vec{U}$ followed by short relaxations continues until the system leaves the initial basin and enters a region where the PEL presents a direction of negative curvature. In principle, a diagonalization of the Hessian is required to obtain the local curvatures. However, a full diagonalization at each step would be very computationally intensive. To solve this issue, ART Nouveau includes the Lanczos algorithm which returns only the smallest eigenvalue for a fraction of the cost of the full diagonalization, if one accepts a decrease in numerical accuracy [99]. The second part of the activation step is to move the system in the direction of the negative curvature until a saddle is reached. To do so, the vector corresponding to the negative eigenvalue is verified to be in the direction opposite to the atomic forces (ascending direction in the PEL). This new displacement vector is then followed until the saddle is reached,

Value	Parameter
5	Number of perpendicular relaxation steps during the escape from the initial basin
5	Number of perpendicular relaxation steps during convergence to the saddle point
0.125	Size of the step along $\vec{U}$ during the escape from the initial basin
0.025	Size of the step along $\vec{U}$ during convergence to the saddle point
-2.0	Cut-off of the curvature needed to start convergence
2.5 Å	Radius of the cluster in which the atoms follow $\vec{U}$
0.1 eV	Threshold of the maximum energy relative decrease during planar minimization

Table 3.4: List of the parameters used for the ART in the present study.

that is, until all atomic forces are below a threshold.
(2) The relaxation step: once at the saddle point, a gentle push ($0.025\vec{U}$) along the direction of negative curvature followed by damped dynamics leads the system to a new IS. Besides, a push in the opposite direction is used to verify that the saddle point is also connected to the initial state and thus check that the system did not stray in the PEL during the activation step.
Despite its initial simplicity, the ART requires the careful tweaking of a large number of parameters summarized in Tab. 3.4. Even after thorough testing, no more than 30% of the searches lead to the discovery of new minima in the present oxide glasses (in the present study, we explored the parameter space and settled for the set of parameter presenting the highest success rate). Most of the failed attempts are due to the system being unable to leave its initial basin, which happens when during the activation step, the relaxations perpendicular to $\vec{U}$ prevent the system to ascend in the PEL.
The displacements along a randomly chosen vector proposed by ART allow the discovery of transitions that would be seen rarely in a MD run due to their high energy. However, in our situation, this is also a drawback since as will be seen in Sec. 6.2, most of these transitions are too high in energy to play a role at the temperatures we are interested in.
However, the ART method has two advantages compared to the MD technique presented above: (1) As the initial displacement follows a random direction centered on an random cluster of atoms, the events have a low probability of being found multiple times. Therefore, ART is efficient at building quickly a catalog of events. (2) ART provides the atomic configuration at the saddle point and thus requires the use of the NEB method only if one wants the full minimum energy path between the initial and final states.

CHAPTER 4

STRUCTURAL AND VIBRATIONAL PROPERTIES OF Ta_2O_5 AND TiO_2 DOPED Ta_2O_5

Before diving into the study of energy dissipation, we need to better understand the structure and vibrational characteristics of oxide glasses since these properties are at the root of energy dissipation at high and low-frequencies. Of the two glasses we will consider in the present study (SiO_2 and Ta_2O_5), only SiO_2 glasses have been properly studied and described. In addition, as mentioned in Chap. 2, the doping of Ta_2O_5 with TiO_2 seems to lead to a reduction of dissipation, linked to changes in the structure of the glass. Therefore, the present chapter will be dedicated to the study of Ta_2O_5 numerical glasses and the impact of TiO_2 doping on their structural and vibrational properties. Comparing our results with experimental data, we will verify the realism of the pair potential and propose a reinterpretation of the Raman spectra of amorphous Ta_2O_5. This chapter is organized as follow: the details of the simulations and the structural characterization are given in Sec. 4.1, while Sec. 4.2 presents the vibrational properties and compares the vibrational spectra of numerical glasses with experimental Raman measurements.

4.1 Structural Characterization

Five series of 10 samples corresponding to pure Ta_2O_5, Ta_2O_5 doped with 20% TiO_2, Ta_2O_5 doped with 50% TiO_2, Ta_2O_5 doped with 75% TiO_2 and pure TiO_2 were generated by cooling high-temperature liquids containing in average $N = 4,700$ atoms at a constant quench rate from 7,000 K to 0 K. During cooling, the cell sizes were dynamically changed in order to maintain zero internal pressure. Each quench was followed by an energy minimization, which continued until the maximum atomic force passed below 10^{-4} eV/Å. For all simulations, we used an Andersen

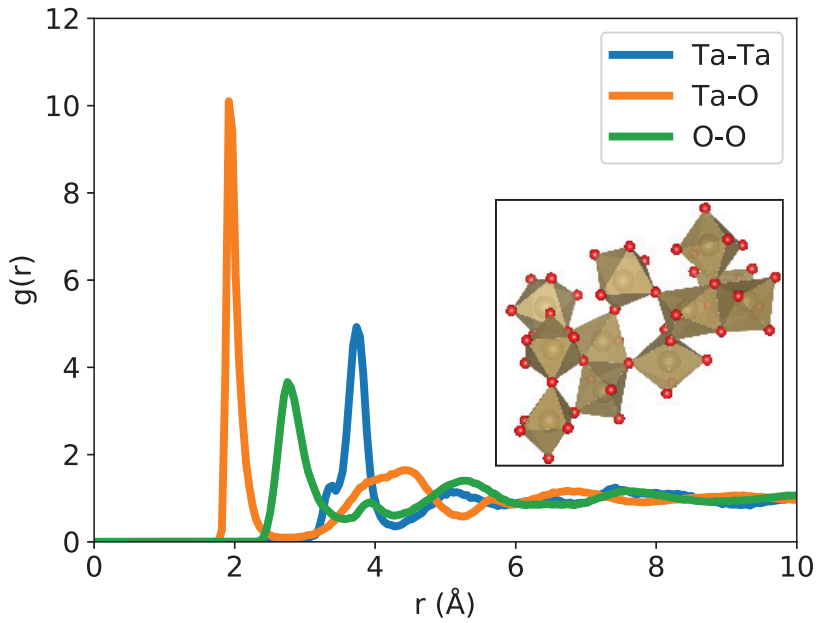

Figure 4.1: Pair distribution function in amorphous Ta_2O_5. The inset shows a small section of a sample, with the O atoms in red, and the Ta-centered polyhedra in brown.

thermostat with a frequency of 1 THz while the interactions between tantalum, titanium and oxygen atoms were modeled using the M-BKS potential described in Sec. 3.1.4. As the structure and vibrational properties are only weakly dependent on the quench rate, we will consider here only the lowest rate, 7.10^{11} K/s.

4.1.1 Tantalum Pentoxide (Ta_2O_5)

We first consider pure Ta_2O_5 glasses whose sample averaged pair distribution is plotted in Fig. 4.1 and confirms the amorphous structure of the solid. The pair distribution function has a first maximum at 1.92 Å for Ta-O bonds, 3.76 Å for Ta-Ta bonds and 2.76 Å for O-O bonds. These values agree with those reported in the latest experimental study [19]: from 1.92 to 1.99 Å for Ta-O and from 3.14 to 3.88 Å for Ta-Ta. The average final density on the Ta_2O_5 samples is 7.96 g/cm^3 at 0 K, slightly higher than the few experimental densities obtained in thin films, which range from 7.68 g/cm^3 [18] to 7.32 g/cm^3 [109]. However, to our knowledge, no bulk amorphous Ta_2O_5 has ever been synthesized and we are not aware of any measurement in TiO_2-doped Ta_2O_5 glasses. As in the glass structure, all Ta atoms are surrounded by first-neighbor O atoms. We consider here only the Ta-O first-neighbor pairs, defined using the first minimum of the Ta-O pair distribution function, to build the nearest-neighbor analysis presented in Tab. 4.1. We see that about 70% of the Ta atoms are surrounded by six first-neighbor O atoms, forming Ta-centered octahedra

Tantalum	%	Oxygen	%
Coord. 4	0.5	Coord. 2	69.9
Coord. 5	28.5	Coord. 3	30.1
Coord. 6	69.4		
Coord. 7	1.6		

Table 4.1: Distribution of average coordination numbers in Ta_2O_5. Only the first-neighbor Ta-O bonds are considered, where a pair of atoms are considered first neighbors if their bond length is in the first peak of the pair distribution function.

as illustrated in the inset of Fig. 4.1. There are about 30% Ta atoms with five first-neighbor O atoms, forming bipyramids. The stability of the high Ta-coordination, also found in the Ta_2O_5 crystalline structure [83, 108], is due to the pseudo-covalent term added to the BKS potential (see Eq. 3.24) [190]. We checked that if this term is removed during quench, tetrahedral networks typical of silica are obtained [197] .

Looking at the MRO, we observed that about 80% of the octahedra are linked together by a vertex, about 12% share an edge and 0.5% share a face (two or three oxygen atoms are then shared between two Ta atoms). Examples are seen in the inset of Fig. 4.1. These structural variations are required by the stoichiometry, since a composition of Ta_2O_5 cannot be constructed solely by vertex-sharing octahedra, which would result in a Ta_2O_6 composition. This is different from SiO_2, where the local tetrahedral structure is consistent with the glass stoichiometry, leading to defect-free glasses entirely made of vertex-sharing tetrahedra.

The angular distribution analysis presented in Figs. 4.2 & 4.3 shows that the inside of each octahedron is ordered, with O-Ta-O angles (inter-polyhedra angles), forming either 90° or 180° bonds. The distribution drops to 0 near 180° because of the disappearance of the solid angle in this direction (since the area element $d\Omega = \sin\phi d\theta d\phi$ is a function of ϕ). This artifact can be avoided by biasing the distribution with the sine of the angle ($f(\phi)' = f(\phi)/\sin\phi$), but then the maxima at 90 and 180° are of similar heights, while we expect the maximum at 90° to be higher than at 180° since there are 4 times more 90° angles than 180° angles in an octahedron. The connectivity between octahedra on the other hand is less organized, as shown by the broad distribution of Ta-O-Ta angles (inter-polyhedra angles), in Fig. 4.3. We checked that the maximum at 105° is created by O-3Ta (i.e. O atoms with 3 Ta neighbors) and thus the presence of octahedra sharing an edge with one of the local Ta-O bond stretched due the three-fold configuration of the O atom. The broad peak between 120° and 180° is formed by O-2Ta and shows that amorphous Ta_2O_5 is a network of interconnected octahedra forming a chain-like structure reminiscent of the structure of crystalline Ta_2O_5 [83, 174].

Using quasistatic simulations, we computed the Young's modulus of Ta_2O_5 through a linear fit on the mechanical response in traction and found a value of 146.0 GPa, close to the experimental

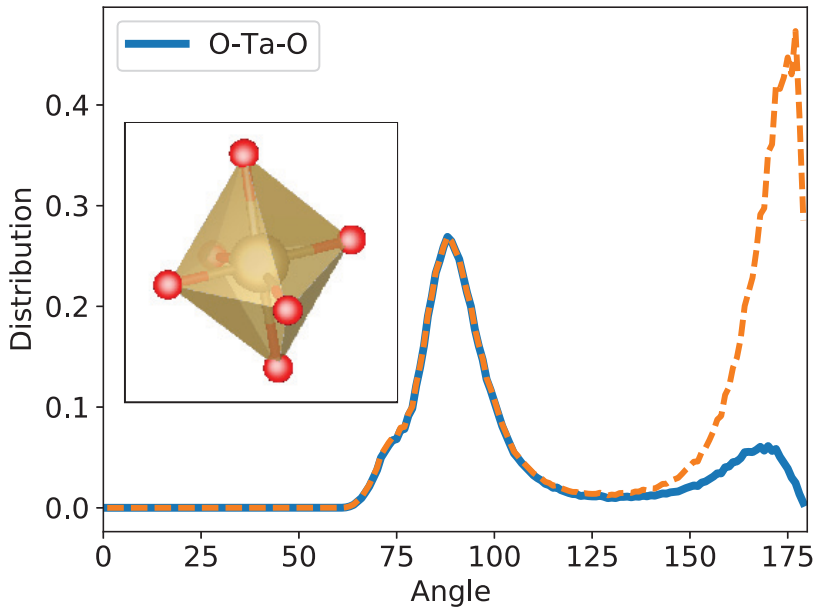

Figure 4.2: Angular distribution of the O-Ta-O bonds in Ta_2O_5 (intra-polyhedron bonds). The dashed line represents the angular distribution of bonds corrected to take into account the solid angle disappearance at 180°.

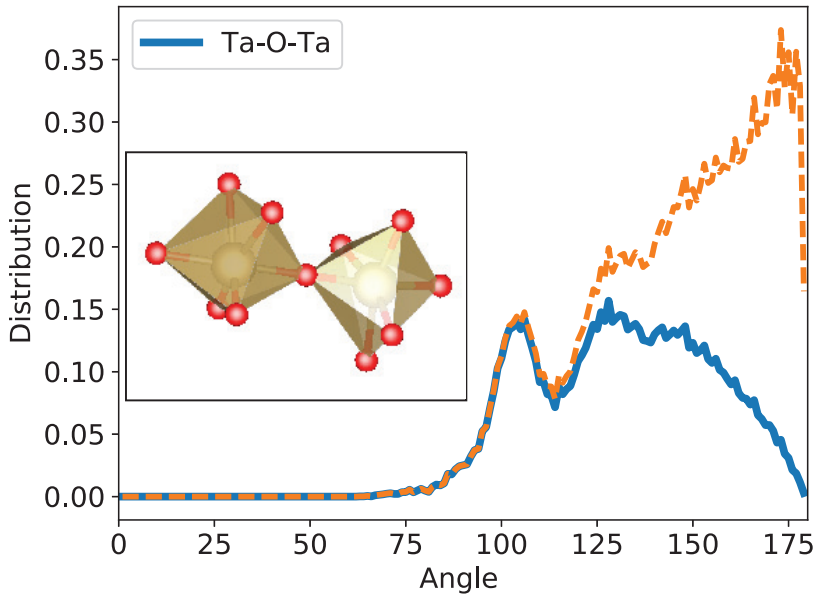

Figure 4.3: Angular distribution of the Ta-O-Ta bonds in Ta_2O_5 (inter-polyhedron bonds). The dashed line represents the angular distribution of bonds corrected to take into account the solid angle disappearance at 180°.

Tantalum	%	Titanium	%	Oxygen	%
Coord. 4	1.1	Coord. 4	4.1	Coord. 2	33.9
Coord. 5	27.6	Coord. 5	45.0	Coord. 3	65.0
Coord. 6	68.7	Coord. 6	50.4	Coord. 4	1.2
Coord. 7	2.6	Coord. 7	0.5		

Table 4.2: Distribution of average coordination numbers in Ta_2O_5-TiO_2. Only the first-neighbor Ta-O and Ti-O bonds are considered.

value of 140 ± 15 GPa found by nanoindentation of Ta_2O_5 thin films [5].
The good agreement between the structures generated here and their mechanical properties, with the data provided in the limited experimental literature shows that the present modified BKS potential produces realistic amorphous structures of Ta_2O_5.

4.1.2 Titanium doped Tantalum Pentoxide (Ta_2O_5-TiO_2)

Next, we focus on the samples containing 20% of Ti. The 10 glasses obtained after quench for this doping concentration have an average density of 8.00 g/cm^3 for a cell size of about 39.0 Å. In Fig. 4.4, the pair distribution functions show similar profiles for the Ta-O and Ti-O bonds. Considering the representation of the Ta_2O_5-TiO_2 glass in the inset of Fig. 4.4, we see that the Ti atoms play the same role as Ta atoms, occupying the center of six- and five-folded polyhedra. However, the first peak of the pair distribution function is slightly sharper for Ti-O bonds, indicating that Ti atoms produce a more homogeneous first-neighbor structure, as already reported by Bassiri *et al.* [18]. The maximum of the pair distribution function is at 1.99 Å for both Ta-O and Ti-O and 3.74 Å for Ta-Ta, in agreement with the experimental results reported in Ref. [18]. However the maximum of the pair distribution function is at 3.65 Å for Ti-Ta, which is slightly larger than the experimental value of 3.29 Å. Looking at the number of nearest neighbors in Table 4.2, we see that the environment of the Ta-atoms is not much different from Ta_2O_5 since the fractions of five- and six-folded polyhedra remain close to 30 and 70 % respectively. On the other hand, Ti atoms form almost as many five- and six-fold polyhedra. In Ta_2O_5-TiO_2, more polyhedra share edges and faces as a consequence of the larger fraction of three-folded O atoms (65.0 % in Ta_2O_5-TiO_2 versus 30.1 % in Ta_2O_5).
The bond angle distribution for Ta_2O_5-TiO_2 (Figs. 4.5 and 4.6) shows an internal organization of the Ta- and Ti-centered polyhedra close to that obtained for Ta_2O_5, with intra-polyhedra angles mainly oriented at 90° and 180°. However, the distributions are slightly more heterogeneous than in pure Ta_2O_5, which is shown by broader peaks at 90° and 180°. A split maximum exists in the O-Ti-O angle distribution around 90°. Fig. 4.7 represents the angle distribution for Ti-5O and Ti-6O and reveals that the six-folded Ti atoms contribute evenly between 75° and 90° where the five-folded ones are responsible for the second maximum at 90°. One could expect a peak at 120°

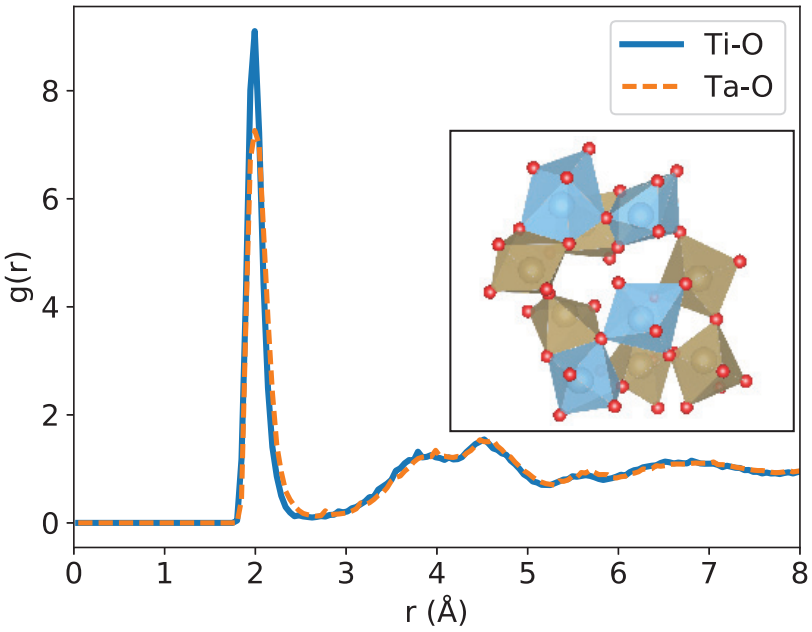

Figure 4.4: Ti-O and Ta-O pair distribution functions in Ta_2O_5-TiO_2 (20 % Ti). The inset shows a small section of a sample, with the O atoms in red, the Ta-centered polyhedra in brown and the Ti-centered polyhedra in blue.

as most of the Ti are five-folded, however, a visual inspection of the samples, as in the inset of Fig. 4.7, shows that the oxygens are placed anisotropicaly around the five-folded Ti atoms in such a way that the O-Ti-O angles are closer to 90° or 180°. The inter-polyhedra Ta-O-Ti, Ta-O-Ta and Ti-O-Ti angle distributions show two peaks at 100° and 125°. The former was already present in Ta_2O_5 and the latter reflects the shift from 30% of three-folded oxygen atoms in Ta_2O_5 to 60% in Ta_2O_5-TiO_2. Ta_2O_5-TiO_2 glasses retain a structure of network of polyhedra but the higher connectivity of the oxygen atoms implies a structure less close to the chain-like structure of crystalline Ta_2O_5.

4.2 Vibrational Properties

The vibrational response of amorphous Ta_2O_5 and TiO_2-doped Ta_2O_5 glasses has not been reported before. It is important to remind the reader that phonons are not defined in amorphous materials above the Ioffe-Regel limit, where the notion of wavevector becomes ill-defined [22, 21, 41]. We will prefer the term of vibration.

To obtain the vibrational eigenmodes, we compute the dynamical matrix (also referred to as the stiffness or Hessian matrix) by taking the second derivative of the analytical expression of the Wold-truncated modified BKS potential [52, 10]. The matrix is defined from the potential energy

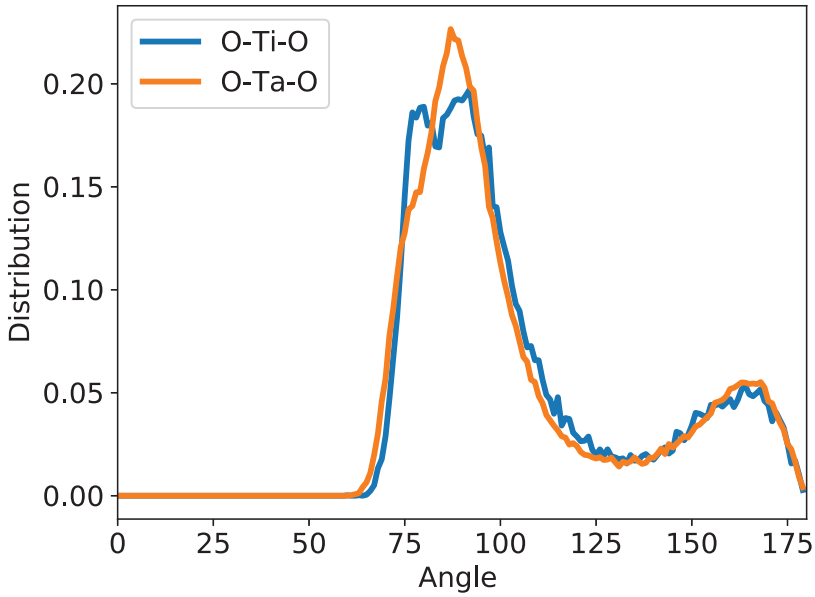

Figure 4.5: Angular distribution of O-Ta-O and O-Ti-O bonds (intra-polyhedron bonds) in Ta_2O_5-TiO_2 (20 % Ti).

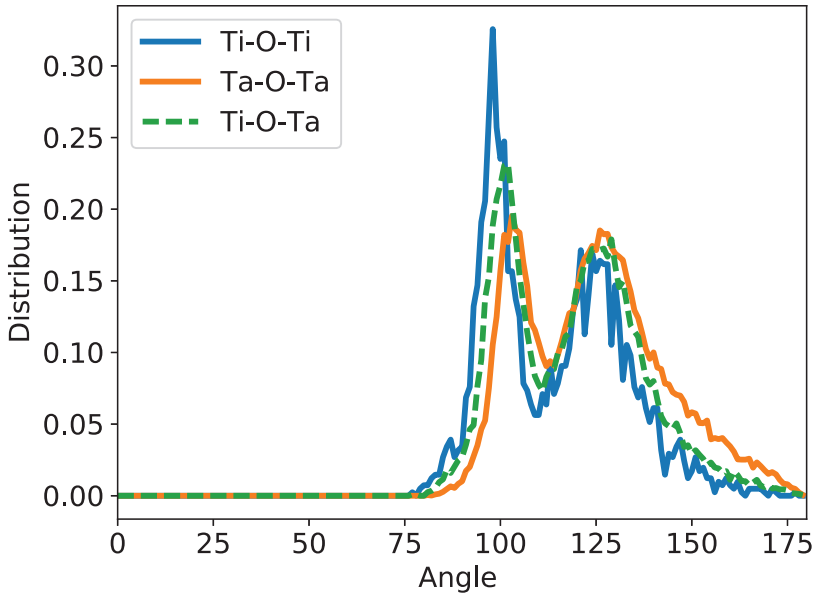

Figure 4.6: Angular distribution of Ta-O-Ta, Ti-O-Ta and Ti-O-Ti bonds (inter-polyhedron bonds) in Ta_2O_5-TiO_2 (20 % Ti).

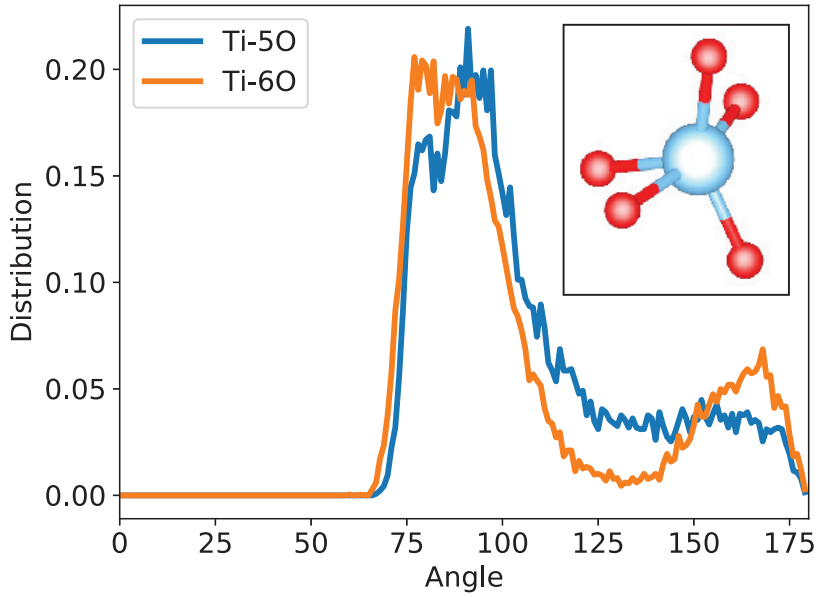

Figure 4.7: Angular distribution of bonds for 5- and 6-folded Ti atoms in Ta_2O_5-TiO_2 (20 % Ti). The inset shows a Ti-5O cluster with anisotropic placement of the O atoms around Ti. This configuration prevents 120° angles that should be expected from a five-folded atom.

E_{pot} of the system as :

$$D_{ij}^{\alpha\beta} = \frac{1}{\sqrt{m_i m_j}} \frac{\partial^2 E_{pot}}{\partial x_i^\alpha \partial x_j^\beta}, \tag{4.1}$$

where i and j refer to atoms and α and β to directions of space. We performed direct diagonalization of the dynamical matrix using the LAPACK package [1], from which we obtain the $3N-3$ eigenvectors (discarding the 3 translational modes allowed by the PBC) and their $3N-3$ corresponding eigenvalues, which are the square of the vibrational frequencies. Plotting the frequency distribution of these modes for Ta_2O_5 and Ta_2O_5-TiO_2, we obtain the vibrational density of states (VDOS) presented in Figs. 4.8 and 4.9. In addition, we plot the partial VDOS, which represents the weighted displacements carried by Ta, Ti or O atoms, defined as:

$$VDOS(\omega) = \frac{1}{3N-3} \sum_i^M \sum_n^{3N-3} |e_i^n|^2 \delta(\omega - \omega_n), \tag{4.2}$$

where e_i^n is the displacement of the ith particle in the nth mode restricted to i being either Ta, Ti or O atoms, and M the number of the corresponding type of atoms. As seen in Fig. 4.8, for Ta_2O_5, the Ta atoms are the main carriers of vibrations at low frequencies ($< 6 \sim 7$ THz), while the O atoms are dominant at higher frequencies. This is coherent with the difference of

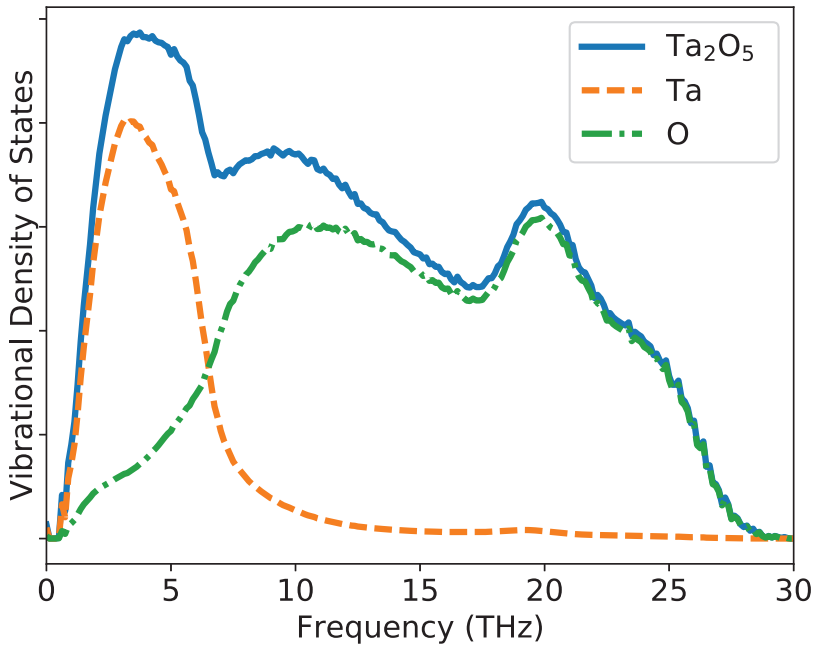

Figure 4.8: Full and partial vibrational density of states of Ta_2O_5.

mass between Ta (heavier) and O atoms. In Ta_2O_5-TiO_2, the Ti particles carry the displacements around 8.5 THz, which is between the Ta- and O-dominated ranges of frequencies. Fig. 4.10 shows the evolution of the VDOS for different Ti compositions. As expected from the partial VDOS in Fig. 4.9, when the % of Ti atoms increases, the first peak, which arises from the vibrations of the Ta atoms decreases while the presence of additional Ti atoms add frequencies between 5 and 15 THz. In addition, the O peak at 19 THz is slightly shifted towards higher frequencies.

To characterize the vibrational eigenmodes, we computed the participation ratio (PR), which expresses the fraction of particles taking part to the motion for a given mode. The PR is defined as:

$$PR(\omega) = \frac{1}{N} \frac{(\sum_{i=1}^{N} \|\vec{e_i^n}\|^2)^2}{\sum_{i=1}^{N} \|\vec{e_i^n}\|^4} \delta(\omega - \omega_n). \tag{4.3}$$

For Ta_2O_5, the PR plotted in Fig. 4.11 shows four different regimes: (1) From 0 to 2 THz, there is a mix of high PR delocalized modes and low PR modes that correspond to soft modes. The delocalized modes are plane waves spanning the entire system leading to a wavelength-dependent high PR. Soft modes are the superposition of delocalized modes of long wavelength with localized displacements involving only small groups of atoms. These modes are known to be the markers of imminent plastic deformation (their frequency tends to zero when the system approaches a plastic event) [179, 117, 151].(2) From 2 to 6 THz, the PR increases slowly from 20 to 25 %

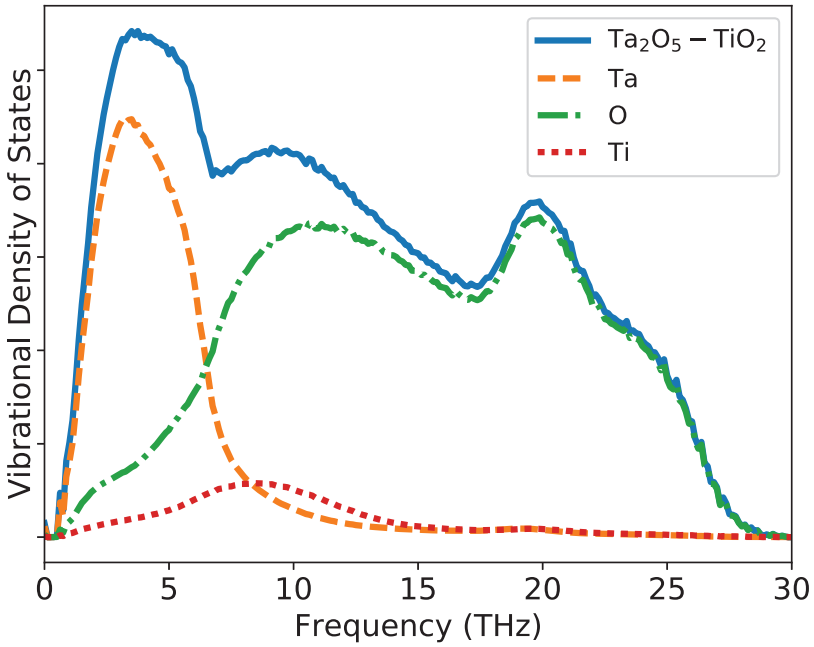

Figure 4.9: Full and partial vibrational density of states of Ta_2O_5-TiO_2 (20 % Ti).

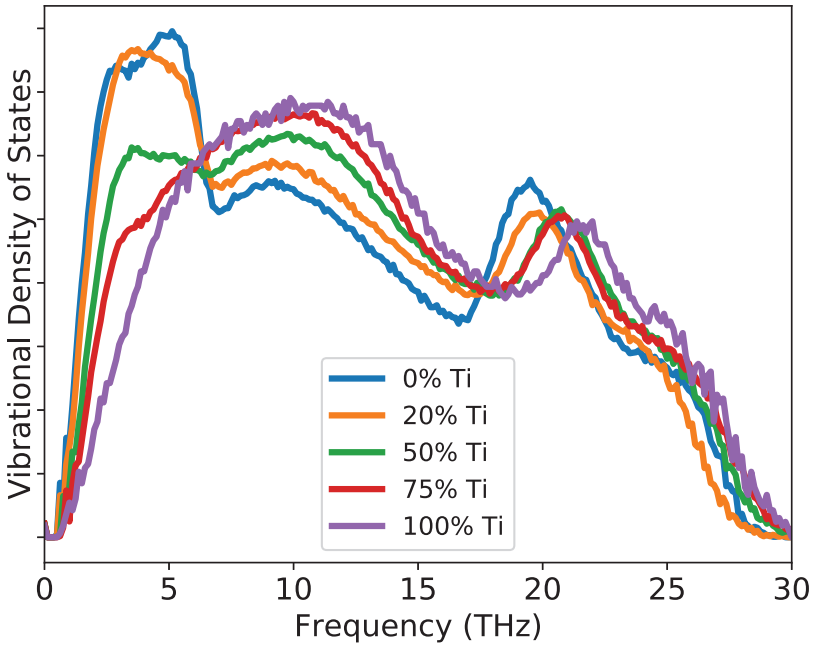

Figure 4.10: Vibrational density of states in Ta_2O_5-TiO_2 with different % of Ti atoms.

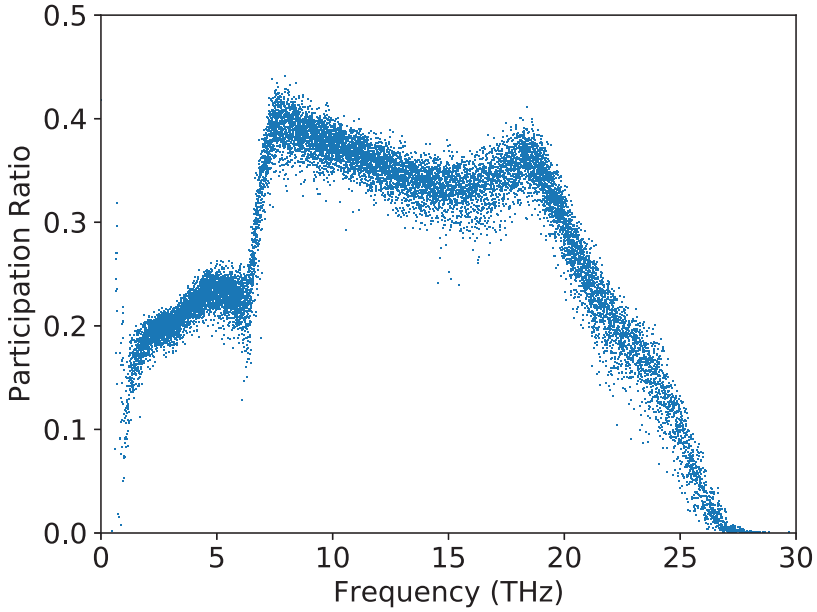

Figure 4.11: Participation ratio in Ta_2O_5. Each dot represents an eigenmode.

before dropping down to 14 % at 6.5 THz. This region is dominated by the Ta vibrations and the relatively low PR is due to the fact that Ta atoms represent only 2/7th of the total number of atoms. The drop in PR corresponds to the crossover frequency between Ta- and O-dominated vibrations (see Fig. 4.8), a frequency range where neither the Ta nor the O can carry vibrations.(3) From 6 to 19 THz, there is a plateau between 30 and 40 % including some modes going as low as 24 %. This regime matches the frequency range where the O atoms carry the vibrations and the light drop in PR matches the decrease seen in the partial VDOS of O. (4) From 19 to 30 THz, the PR shows a continuous decay down to 0% at about 30 THz, corresponding to modes more and more spatially focused. These high-frequency modes are equivalent to optic modes in crystalline materials [119].

Looking at the PR for Ta_2O_5-20%TiO_2 in Fig. 4.12, we see that the TiO_2 doping removes the drop previously observed at 6 THz. As seen in the partial VDOS of Fig. 4.9, the Ti atoms fill the vibrational gap in this frequency range. No other significant differences are observed between the Ta_2O_5 and Ta_2O_5-TiO_2 spectra.

4.2.1 Interpretation of the Raman spectra of Ta_2O_5

In absence of experimental data for the VDOS of glassy Ta_2O_5, we compare our calculations with experimental Raman data. It should be noted that most interpretations of Raman data [128, 49, 48, 138, 93, 108] are based on an analogy of other oxide compounds such as V_2O_5 due to

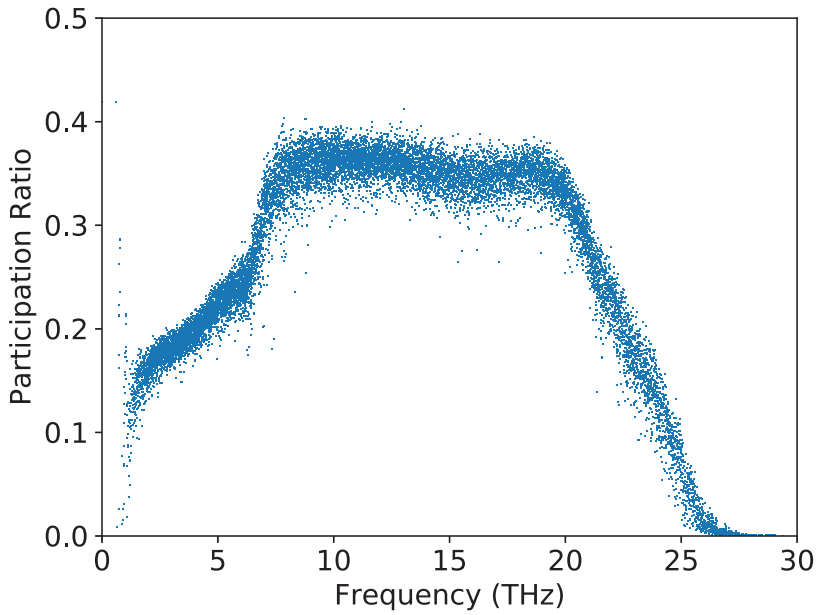

Figure 4.12: Participation ratio in Ta_2O_5-TiO_2 (20 % Ti). Each dot represents an eigenmode.

the limited knowledge available on the structure of amorphous Ta_2O_5. The present Raman measurements were performed on a 15 μm thick glassy Ta_2O_5 layer deposited through ion beam sputtering. Spectra were recorded at room temperature with a confocal LabRAM HR Evolution micro-spectrometer. Measurements were carried out using a YAG:Nd3+ laser line at 532 nm, from 5 to 1500 cm-1 with a 2.5 mW laser power at focal point. A confocal pinhole diameter was set at 75 μm allowing to probe only the thin layer and no its substrate. Fig. 4.13 compares the computed VDOS with the experimental reduced Raman intensity (i.e. the measured intensity divided by the thermal population factor $n(\omega,T)+1$ for Stokes scattering). Although the Raman response provides an indirect picture of the VDOS (through polarizability modulation), the two curves show good qualitative agreement in terms of their main features and respective intensities.

To identify the atomic origin of the different features of the Raman spectra, we plot in Fig. 4.15 the partial VDOS for O atoms projected on the rocking, stretching and bending motions illustrated in Fig. 4.14. For the two folded oxygens, the motion of the oxygen atom for each mode is projected on three different vectors as done in Refs. [181, 168] for silica. For the three folded oxygens, bond bending is obtained by projecting the motion of the O atom on a unit vector perpendicular to the plane of the three Ta neighbors, while the remaining part of the motion is an in-plane vibration, which corresponds to the stretching of the bond. We did not find an equivalent of rocking motion for O-3Ta bonds.

The most prominent feature seen in the Raman spectrum of Fig. 4.13 is the band at 20 THz ($\sim$ 670 cm^{-1}). This band is present in the partial VDOS of Fig. 4.15 at the same frequency

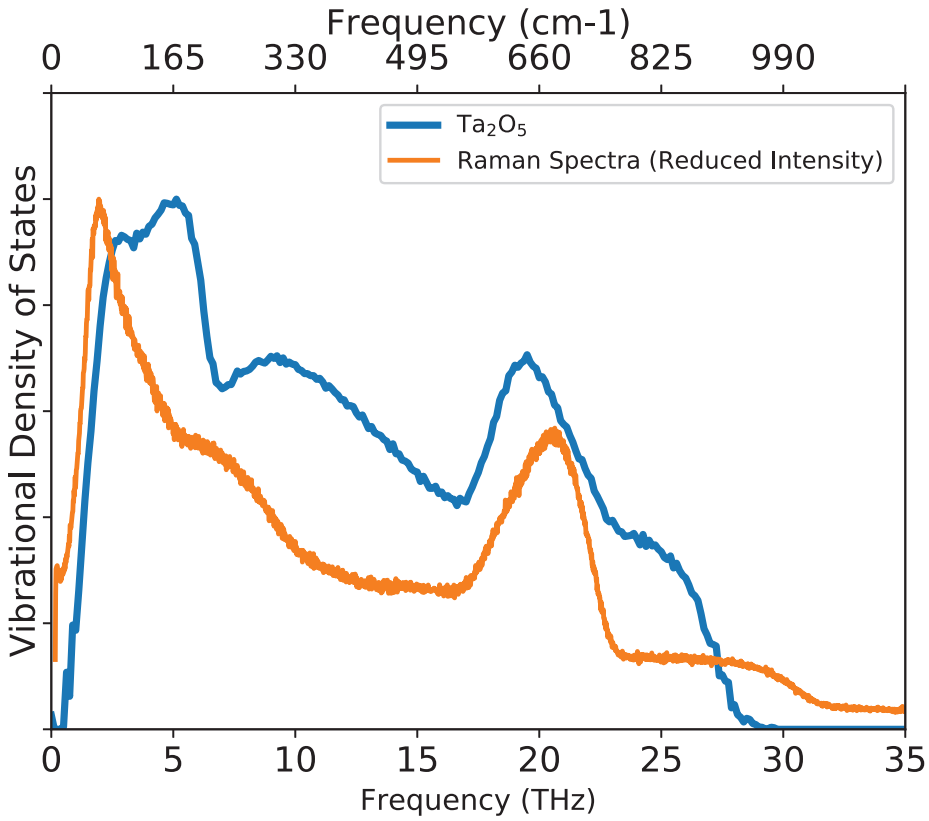

Figure 4.13: Full vibrational density of states in Ta_2O_5 (in blue) superimposed with the Raman spectra of Ta_2O_5 (in orange).

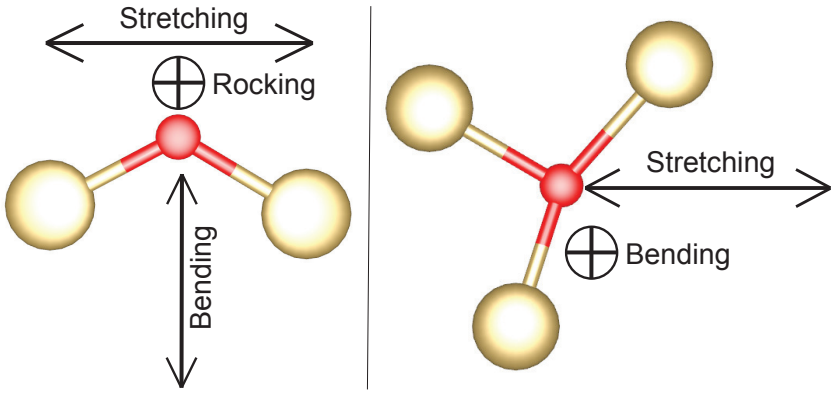

Figure 4.14: Sketch of O-2Ta and O-3Ta bonds with the vectors used to decompose the bond deformation into bending, stretching and rocking components.

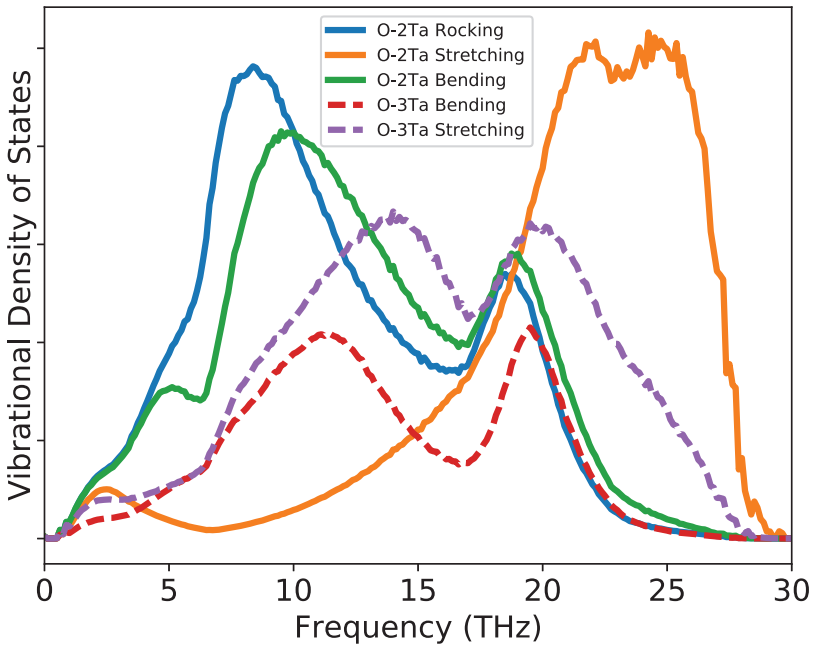

Figure 4.15: Decomposition of the vibrational density of states in a Ta_2O_5 glass onto the rocking, stretching and bending of O-2Ta bonds, and on the bending and stretching of O-3Ta bonds.

and corresponds to maxima for both O-3Ta bending and stretching, which agrees with former interpretations of Raman spectra [128, 49, 138]. At higher frequencies, above 24 THz (~ 800 cm^{-1}), the Raman spectrum shows a shoulder, also present in the calculated VDOS albeit less extended towards the high frequency end. According to the partial VDOS of Fig. 4.15, this shoulder is due to the stretching of O-2Ta, which is again in agreement with the literature [128, 49, 138].

Below 7 THz (~ 230 cm^{-1}), the Raman spectrum essentially consists of a sharp band peaking at 2 THz (~ 70 cm^{-1}), while in this frequency range the calculated VDOS shows a wider dual maximum. The accepted interpretation of the Raman band below 3 THz is that the vibrations arise from inter-polyhedra interactions or/and charged clusters [49, 48, 138, 93]. However, Fig. 4.8 shows that from 0 to 5 THz, the vibrations are essentially carried by the Ta atoms that can be viewed as optical-like modes lying in the low frequency range due to the large mass of the Ta atoms. This is confirmed by the observation of low frequency narrow bands in the Raman spectra of crystalline Ta_2O_5 [93]. Therefore the sharp band observed in the low frequency Raman spectrum of Ta_2O_5 does not seem to be linked to inter-polyhedra interactions. Note that the absence of a double band in the Raman spectrum, unlike the VDOS, can be due to polarization effects (i.e. Raman selection rules) not accounted for in the VDOS calculations. It is worth mentioning that the low frequency range near 2 THz (~ 70 cm^{-1}) is typical of the excess VDOS (boson peak) for inorganic glasses. However, due to the low-lying optical-like vibrations of the

heavy Ta atoms, it is impossible to clearly identify a boson peak for Ta_2O_5 though it may lie underneath the low frequency bands. A clarification of this matter would require to investigate lower frequency vibrations (i.e. below 0.5 THz), which is not possible with the present calculations due to the limited box size of the samples. Note that the slight discrepancy between the VDOS and the Raman curves observed towards the lowest frequency edge below 2 THz can also be due to the presence of quasielastic scattering in the Raman signal, which is ascribed to anharmonic motions that are not modelled by our calculations.
Finally, from 3 to 13 THz (~ 100-430 cm^{-1}), the Raman spectrum shows a shoulder also seen in the VDOS, although at slightly larger frequencies. The Raman band at these frequencies is usually explained by internal O-Ta-O bending, as is the case in similar oxides at these frequencies [49]. The partial VDOS plotted in Fig. 4.15 shows that most of the vibrations in this frequency range are indeed carried by the bending and rocking motions of O-2Ta, thus in agreement with the Raman interpretation.

4.3 Summary

In this chapter, we studied the structure of Ta_2O_5 and TiO_2 doped Ta_2O_5 numerical glasses. We showed that these materials are formed of chain-like structures of octahedra linked by a vertex, an edge or a face. We also showed that doping amorphous Ta_2O_5 with TiO_2 does not alter the glass structure in a strong way as Ti atoms form equally five- and six-folded polyhedra that perturb but do not break the network of the glass.
Performing a vibrational eigenmode analysis and projecting the eigenmodes on the rocking, stretching and bending motions of the Ta-2O and Ta-3O bonds, we provide an atomic-scale analysis that substantiates the interpretations of Raman spectra of amorphous Ta_2O_5 used to characterize the short- and medium-range orders in glasses. This eigenmode analysis also reveals the key role played by Ti atoms in the 5 to 12 THz range.

CHAPTER 5

HIGH FREQUENCY ENERGY DISSIPATION

This chapter will be dedicated to the study of dissipation at high frequency (in the range of THz). From the point of view of potential applications, the present chapter is not pertinent, as only a handful of devices work at such high frequencies. However, the interest of the theoretical issue and the potential repercussion the present work can have in the field of high-frequency scattering method (notably Brillouin and Inelastic X-ray scattering), where the attenuation of acoustic vibrations is used to explore the structure of glasses, make it an interesting problem to tackle.

In the THz regime, dissipation comes from the coupling between passing mechanical waves (ultrasonic sound waves) and the vibrational eigenmodes of the system. However, we saw in Chap. 2 that studying dissipation in disordered solids through the dynamical structure factor $S(q,\omega)$ is limited to frequencies below the Ioffe-Regel (IR) limit, since above, the spectra at fixed wave-vector q cannot be fitted by only one damped harmonic oscillator (DHO). To avoid this limitation, we will implement numerical mechanical spectroscopy to measure directly energy dissipation. In addition, we will propose an analytical development in the harmonic approximation to substantiate our numerical experiment and expose the structural origin of energy dissipation in SiO_2 and Ta_2O_5 glasses.

The details of the simulations are given in Sec. 5.1 while the analytical calculations are presented in Sec. 5.14. The results of the simulations are compared to experimental data and dissipation given by the analytical expression in Sec. 5.2. Finally, in Sec. 5.3, we discuss the properties of dissipation deduced from the analytical expression for SiO_2 and Ta_2O_5 glasses.

5.1 Methodology

5.1.1 Mechanical spectroscopy

Mechanical spectroscopy was simulated by imposing cyclic deformations to the simulation cell and following the resulting internal stress to compute the complex modulus as a function of the loading frequency. This method only considers the first harmonic of the decomposition in Fourier series of the constraint and therefore requires to be in the linear response regime. In the following, we mainly consider the case of isostatic deformations. We also performed simple shear deformations, but they resulted in qualitatively similar results and will only be briefly discussed in the last sections of the present chapter.

For isostatic deformations, the simulation cell is subjected in the X, Y and Z directions to a sinusoidal applied strain

$$\epsilon(t) = \epsilon_0 \sin(\omega t), \tag{5.1}$$

with a frequency $\omega/2\pi$ varying from 0.1 to 50 THz and an amplitude $\epsilon_0 = 0.007$ chosen such that the deformation remains elastic in the quasistatic limit. The system is thermostated in order to dissipate the heat produced during the deformation cycles and maintain a constant temperature, which was varied from 10 K to 700 K. We compared different thermostats (Andersen, Nose-Hoover, Langevin) with different strengths but did not find any marked influence on the computed dissipation. In the following, we will consider a Langevin thermostat, which allows for analytical calculations developed in Sec. 5.1.3 and limit our study to the high temperature regime of classical mechanics [15]. Atomic trajectories are integrated using the SLLOD equations for isostatic tractions and compressions presented in Sec 3.1.3.

The Langevin friction, γ, was varied between 0.1 and 10 THz. Below 0.1 THz, the thermostat is too weak to maintain a constant temperature and above 10 THz, the forcing is too strong and affects the dynamics of the glass (the influence of the friction parameter is further discussed in Sec. 5.2). The time step of the simulations was 1 fs when the forcing frequency was 1 THz or below. Above 1 THz, the time step was set to $10^{-3}/\omega$ in order to maintain a constant strain increment per simulation step.

We follow the time-evolution of the pressure $P(t)$, which, in the stationary regime, is a periodic function of same period as the applied strain, $T = 2\pi/\omega$, with cycle-dependent fluctuations illustrated in Fig. 5.1. In the following, we consider the smooth periodic part of the pressure averaged over multiple cycles (dark blue line in Fig. 5.1):

$$\langle P \rangle(t) = \lim_{N \to +\infty} \frac{1}{N} \sum_{n=0}^{N} P(t + nT). \tag{5.2}$$

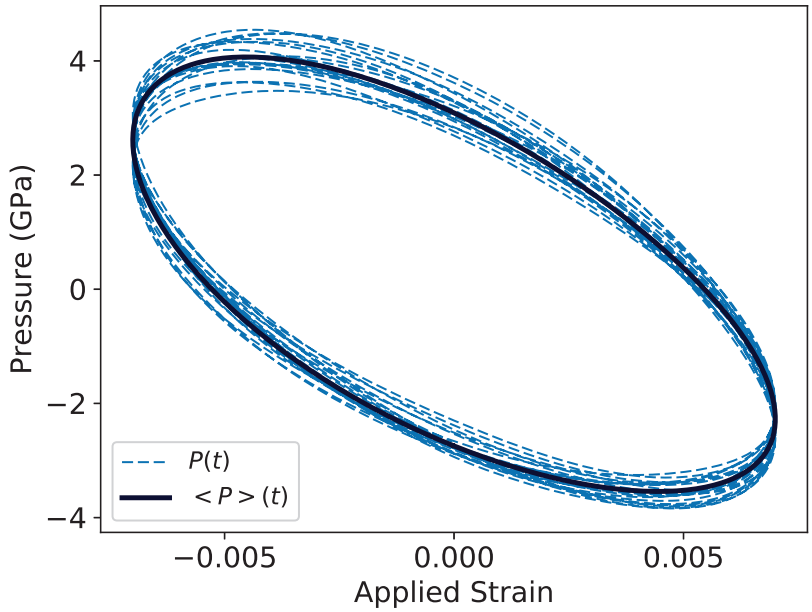

Figure 5.1: Evolution of the hydrostatic pressure during cycles of isostatic applied strain. The dashed curves show the instantaneous pressure. The solid curve is the average computed over 250 cycles.

From Sec. 2.2, we know that dissipation is related to the loss angle ϕ between the pressure, $\langle P\rangle(t) \propto \sin(\omega t + \phi)$, and the applied strain $\epsilon(t)$:

$$\begin{aligned} Q^{-1}(\omega) &= \tan(\phi) \\ &= \frac{1}{\omega}\frac{\int_0^T \langle P\rangle(t)\dot{\epsilon}(t)\,\mathrm{d}t}{\int_0^T \langle P\rangle(t)\epsilon(t)\,\mathrm{d}t}. \end{aligned} \tag{5.3}$$

It is with this formula that dissipation will be computed.

The spectroscopic simulations were performed during 300 deformation cycles, the value of the energy dissipation usually converging after about 50 cycles, after which the glass enters a stationary regime where all measurements were carried out.

5.1.2 Harmonic approximation

In order to separate harmonic and anharmonic effects, mechanical spectroscopy was also applied to harmonic systems, where the interaction between particles was approximated using the dynamical matrix of the system,

$$\tilde{D}_{ij}^{\alpha\beta} = \frac{1}{\sqrt{m_i m_j}}\frac{\partial^2 E}{\partial r_i^\alpha \partial r_j^\beta} = \frac{1}{\sqrt{m_i m_j}} D_{ij}^{\alpha\beta}, \tag{5.4}$$

where indices i and j refer to atoms and α and β to Cartesian coordinates. The dynamical matrices were computed, as in the previous chapter, on the equilibrium configurations obtained after energy minimization. The potential energy, E, was computed using the Wolf-truncated BKS potential, which is an analytical pair potential and thus yields an analytical expression for the dynamical matrix.

The potential energy in the harmonic approximation is expressed as

$$E = \frac{1}{2} \sum_{i\alpha j\beta} D_{ij}^{\alpha\beta} (r_i^\alpha - R_i^\alpha)(r_j^\beta - R_j^\beta), \tag{5.5}$$

where r_i^α (resp. R_i^α) represents the actual (resp. initial) position of atom i. However, as the cell is deformed, r_i^α is the position in the current cell of size L(t) while R_i^α is the position in the initial cell of size L(0). Therefore, computing $r_i^\alpha - R_i^\alpha$ raises an issue due to the minimum image convention as discussed in Sec. 3.1.3. To bypass this issue, the potential energy of the system was approximated as:

$$E = -\frac{1}{4} \sum_{i\alpha j\beta} D_{ij}^{\alpha\beta} (r_{ij}^\beta - R_{ij}^\beta)(r_{ij}^\alpha - R_{ij}^\alpha) \tag{5.6}$$

where r_{ij}^α (resp. R_{ij}^α) is the separation between atoms i and j in direction α in the deformed (resp. initial) cell, using the minimum image convention to account for the periodic boundary conditions. The corresponding expressions for the atomic forces and pressure are given in Appendix A.

5.1.3 Analytic expression

The dissipation computed numerically from Eq. 5.3 can be expressed analytically in the harmonic approximation and linear response regime when a Langevin thermostat is assumed. The calculations are detailed in Appendix A in the case of isostatic deformations.

In the general case (deformation following an arbitrary strain tensor ϵ), dissipation is calculated as the ratio of the imaginary and real parts of the complex modulus, which relates here, to the Fourier transforms of the periodic applied strain $\epsilon_{\kappa\xi}(\omega)$ to the cycled-averaged internal stress $\langle\sigma_{\alpha\beta}\rangle$. For that, the cycled-averaged stress in the harmonic approximation is projected on the normal modes of the glass and expressed as the sum of an affine and non-affine contribution:

$$\langle\sigma_{\alpha\beta}\rangle(\omega) = C^\infty_{\alpha\beta\kappa\xi}\epsilon_{\kappa\xi}(\omega) - \frac{2}{V_0}\sum_m C_m^{\alpha\beta}\langle s_m\rangle(\omega), \tag{5.7}$$

where $\omega/2\pi$ is the forcing frequency, s_m the mass-scaled amplitude of the mth normal mode defined in Eq. A.11 and V_0 the volume of the reference undeformed cell. The first term in the RHS of Eq. 5.7 is the affine Born contribution, with $C^\infty_{\alpha\beta\kappa\xi}$ the affine elastic modulus obtained

when all atoms are forced to follow the macroscopic applied uniform deformation $\epsilon_{\kappa\xi}$:

$$C^{\infty}_{\alpha\beta\kappa\xi} = -\frac{1}{4V_0}\sum_{ij}\left[D^{\alpha\kappa}_{ij}R^{\beta}_{ij} + D^{\beta\kappa}_{ij}R^{\alpha}_{ij}\right]R^{\xi}_{ij} + \left[D^{\alpha\xi}_{ij}R^{\beta}_{ij} + D^{\beta\xi}_{ij}R^{\alpha}_{ij}\right]R^{\kappa}_{ij}. \tag{5.8}$$

The second term in the RHS of Eq. 5.7 is the non-affine contribution, which is expressed as a sum over the normal modes of the system:

$$C^{\alpha\beta}_{m} = \frac{1}{2}\sum_{ij\kappa}\left[D^{\alpha\kappa}_{ij}R^{\beta}_{ij} + D^{\beta\kappa}_{ij}R^{\alpha}_{ij}\right]\frac{e^{\kappa}_{j}(m)}{\sqrt{m_j}}. \tag{5.9}$$

Here, $e^{\kappa}_{j}(m)$ is the component on atom j and direction κ of the mth eigenvector of the mass-scaled dynamical matrix $\tilde{D}$, with corresponding eigenfrequency ω_m.

The temporal Fourier transform of the non-affine displacement, $\langle s_m\rangle(\omega)$, is expressed by projecting the linearized SLLOD equation of motion (Eq. 3.14) on the normal modes of the system (see Appendix A for details):

$$\langle s_m\rangle(\omega) = \frac{C^{\kappa\xi}_{m}}{\omega^2_m - \omega^2 + i\gamma\omega}\epsilon_{\kappa\xi}(\omega) \tag{5.10}$$

From Eq. 5.7, the resulting complex modulus is thus:

$$C_{\alpha\beta\kappa\xi}(\omega) = C^{\infty}_{\alpha\beta\kappa\xi} - \frac{2}{V_0}\sum_{m}\frac{C^{\alpha\beta}_{m}C^{\kappa\xi}_{m}}{\omega^2_m - \omega^2 + i\gamma\omega}, \tag{5.11}$$

which involves the response function of the normal modes, $1/(\omega^2_m - \omega^2 + i\gamma\omega)$, broadened by the Langevin thermostat through the $i\gamma\omega$ term (it is interesting to note that this response function is exactly the linear response function of a DHO). Building on the decomposition of the elastic constants into affine and non-affine contributions first proposed by Lutsko [114], Lemaître and Maloney obtained an expression similar to Eq. 5.11 to analyze the visco-elastic response of disordered solids [105]. The static limit of this expression ($\omega = 0$) was used by these authors and Zaccone *et al.* [206] to study the effect of non-affine relaxations on the elasticity of glasses.

In case of isostatic deformations of main interest here, the above equations adopt a more compact form (see Appendix A for details), with the complex bulk modulus relating to the Fourier transform of the average pressure $\langle P\rangle(\omega)$ to the applied strain $\epsilon(\omega)$:

$$K(\omega) = K^{\infty} - \frac{2}{9V_0}\sum_{m}\frac{C^{2}_{m}}{\omega^2_m - \omega^2 + i\gamma\omega}. \tag{5.12}$$

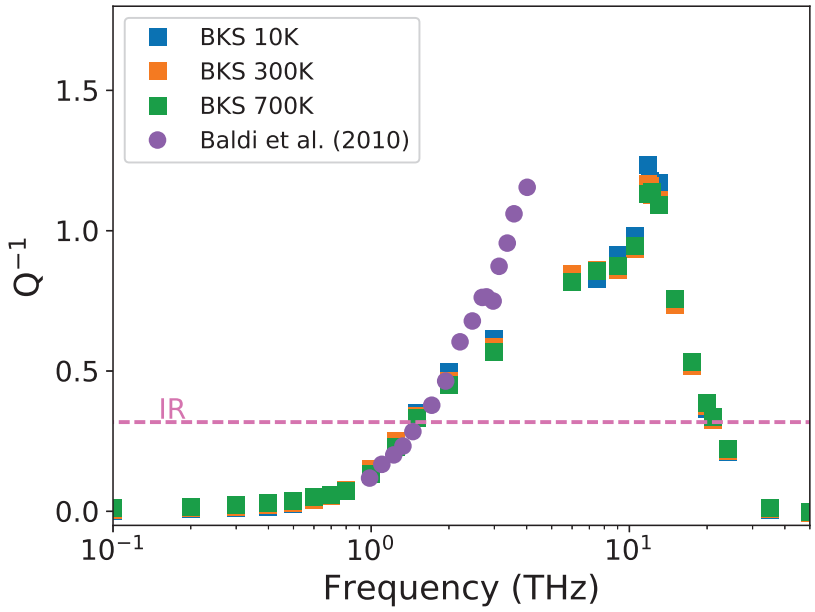

Figure 5.2: Energy dissipation as a function of frequency ($\omega/2\pi$) in amorphous SiO_2 modeled with the full non-linear BKS potential at three different temperatures. The friction of the Langevin thermostat was set to 1 THz. The circles are experimental data obtained by fitting the excitation peak of x-ray scattering spectra with the DHO model [11].

The affine bulk modulus and mode-dependent non-affine term are respectively:

$$K^{\infty} = -\frac{1}{9V_0}\sum_{i\alpha j\beta} D_{ij}^{\alpha\beta} R_{ij}^{\beta} R_{ij}^{\alpha},$$
$$C_m = \sum_{i\alpha j\beta} D_{ij}^{\alpha\beta} R_{ij}^{\alpha} \frac{e_j^{\beta}(m)}{\sqrt{m_j}}. \tag{5.13}$$

Finally, using Eq. 5.12 and Eq. 2.3, we obtain the expression of the dissipation produced by isotropic deformations as the ratio of the imaginary to the real part of the complex modulus:

$$Q^{-1}(\omega) = \frac{\sum_m C_m^2 \frac{\omega\gamma}{(\omega_m^2-\omega^2)^2+(\gamma\omega)^2}}{\frac{9V_0}{2}K^{\infty} - \sum_m C_m^2 \frac{\omega_m^2-\omega^2}{(\omega_m^2-\omega^2)^2+(\gamma\omega)^2}} \tag{5.14}$$

In the next Section, we compare this analytic expression of the dissipation with dissipation obtained using numerical calculations and discuss the physical insights gained from this expression on the origin of dissipation in glasses.

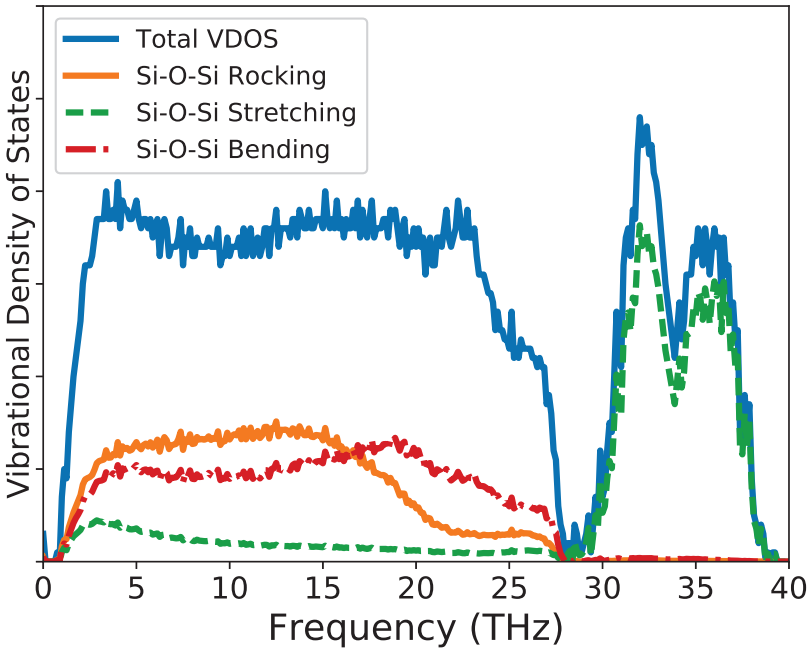

Figure 5.3: Vibrational density of states (VDOS) of the SiO_2 model. The partial VDOS of the oxygen atoms is decomposed on the rocking, stretching and bending motions of the Si-O-Si bonds represented in Fig. 4.14.

5.2 Simulation Results

5.2.1 Full non-linear calculations

The energy dissipation obtained by mechanical spectroscopy in the present amorphous SiO_2 system (obtained following the same protocol as in Chap. 4 for Ta_2O_5) is presented in Fig. 5.2 at three different temperatures. The frequency range broadly covers that of the vibrational density of states of the glass presented in Fig. 5.3 along with the partial VDOS for oxygen atoms projected on the rocking, stretching and bending motions of the Si-O-Si bonds (as done for Ta_2O_5 in Chap. 4). Dissipation is numerically zero below 0.1 THz, increases up to about 1.2 at 12 THz and decreases back to zero above 27 THz. The three sets of data obtained at 10, 300 and 700 K are superposed. This temperature independence is a strong indication that, as expected from previous works [45, 158, 184], dissipation is harmonic in the present range of high frequencies. The energy dissipation was also computed for a few frequencies on a larger system (24,000 atoms) to check for potential size effects. Fig. 5.4 shows that the system size do not affect the calculations. In Fig. 5.2, are also plotted the experimental attenuation data Γ/ω of Baldi *et al.*[11], obtained using a DHO fit of the dynamical structure factor of vitreous SiO_2. The very good agreement between the experimental and numerical data below the Ioffe-Regel (IR) limit, $\Gamma/\omega = 1/\pi$, confirms

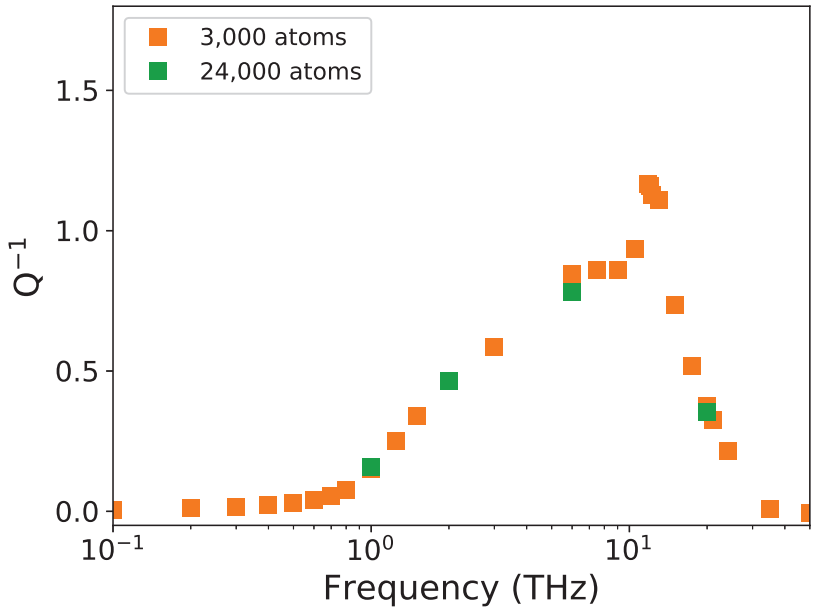

Figure 5.4: Energy dissipation as a function of frequency in amorphous SiO_2 for a small (3,000 atoms) and large (24,000a toms) systems.

the strong connection between the quality Q^{-1} and attenuation Γ/ω factors. However, we note that this link is difficult to justify theoretically, even in the harmonic approximation considered below [139]. In addition, the Ioffe-Regel criterion is defined here from the spectroscopic line-width Γ and not from the (inverse) propagation lifetime of a wavepacket, the later giving slightly different values for the corresponding energy dissipation (see Refs. [184, 21]).
We see in Fig. 5.2 that above the IR limit, the experimental data overestimate the numerical dissipation. This discrepancy might be expected for two reasons. First, as mentioned in Sec. 2.2, simple models like Zener's standard linear solid [139], predict that the dissipation and attenuation factors match only in the limit of low dissipation, while at large dissipation, the attenuation factor overestimates the quality factor. Second, above the IR limit, the dynamical structure factor contains several excitation peaks that cannot be fitted by a simple DHO model [35, 12, 41].

5.2.2 Harmonic approximation

To confirm the harmonic origin of energy dissipation in the present range of frequencies, we applied mechanical spectroscopy to the same sample but with the interactions between particles described using the dynamical matrix of the equilibrium configuration, as explained in Sec. 5.1.2. The resulting energy dissipation is compared with the full non-linear BKS calculations in Fig. 5.5. The very good agreement between both calculations confirms the harmonic origin of dissipation in this frequency range. We note that at low frequencies, typically below 1 THz, the harmonic

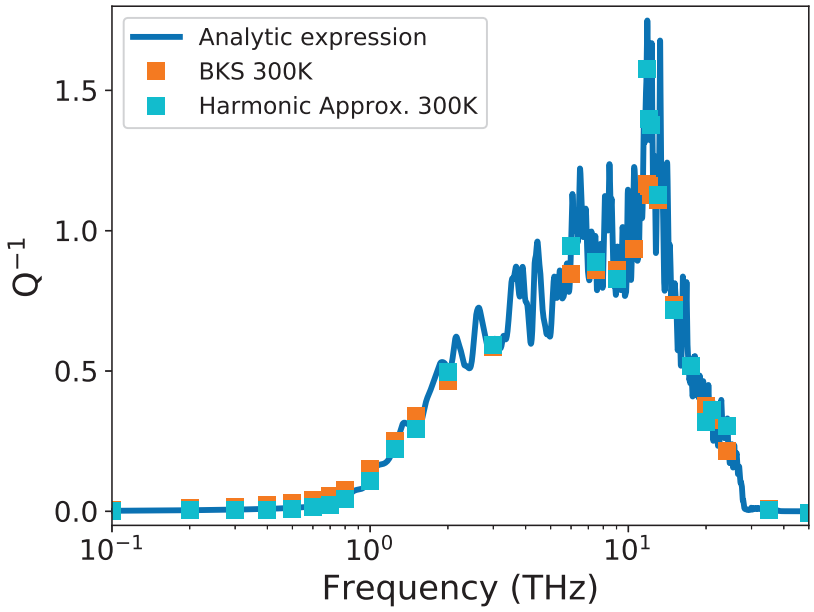

Figure 5.5: Energy dissipation as a function of frequency computed with the non-linear BKS potential, the harmonic approximation of Eq. 5.6 and the analytical expression of Eq. 5.14. The same thermostat friction of 1 THz is used in all calculations.

calculations find a dissipation systematically lower than the non-linear model, an indication that anharmonic effects may play a role in this region. However, we will see below that dissipation measurements are strongly affected by the thermostat in this low-frequency regime.
Finally, we compare in Fig. 5.5 the harmonic simulations to the analytical expression computed from Eq. 5.14. The perfect agreement between both approaches, even in the regions where the dissipation fluctuates rapidly (e.g. near 10 THz), confirms the validity of the analytic calculations of Sec. 5.1.3. The expression of energy dissipation in Eq. 5.14 also shows directly that dissipation in the harmonic regime is independent of the temperature and the strain amplitude (ϵ_0). Q^{-1} however depends on the friction parameter γ of the Langevin thermostat, a point detailed in the following Section, where we also address other properties of dissipation deduced from the analytical expression.

5.3 Properties of Harmonic Dissipation

5.3.1 Physical interpretation

Focusing on the numerator of Eq. 5.14, i.e. the loss modulus, which is mainly responsible for the shape of the dissipation spectrum, we see a sum of contributions coming from the vibrational eigenmodes. Each contribution is the product of the square of the non-affine coefficient C_m

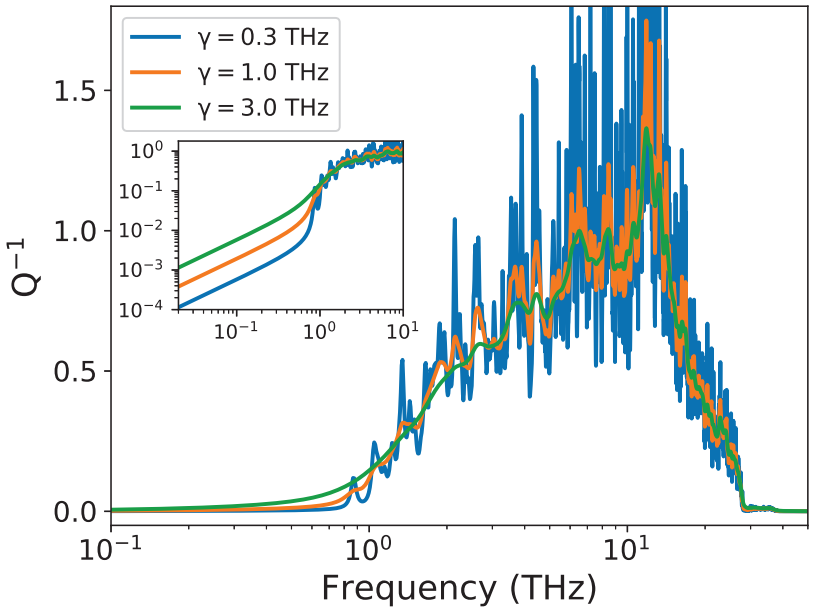

Figure 5.6: Energy dissipation as a function of frequency computed using the analytical expression for three different thermostat frictions: 0.3, 1 and 3 THZ. The inset shows a log-log view of the low frequency region.

(Eq. 5.13) with a Lorentzian centered on the mode eigenfrequency ω_m, with a width fixed by the Langevin friction γ.

Physically, dissipation arises because the deformation applied to the cell triggers non-affine relaxations (Eq. 5.7) that are supported by the eigenmodes of the system (Eq. 5.10). Since the latter are harmonic oscillators damped by the thermostat, they induce a lag in the non-affine stress contribution, which is maximum when the forcing frequency equals the mode eigenfrequency. The coupling coefficient, $C_m^{\alpha\beta}$, reflects the sensitivity of the stress on the amplitude of mode m, since from Eq. 5.7, we see that $C_m^{\alpha\beta} \propto \partial\sigma_{\alpha\beta}/\partial\langle s_m\rangle$. The modes that dissipate most are therefore those that produce large non-affine stress changes and resonate with the forcing frequency.

5.3.2 Influence of the Langevin friction parameter

The dissipation in Eq. 5.14 depends on the friction parameter γ of the Langevin thermostat, which might appear as an artifact since γ is a numerical parameter with no physically defined value. However, we argue below that except in the region $\omega < \gamma$, the shape and main features of the dissipation spectrum do not depend on γ.

The effect of a finite value of γ is to broaden the response function of the eigenmode oscillators (Eq. 5.10). As a result, the loss modulus is expressed as a weighted average of the non-affine

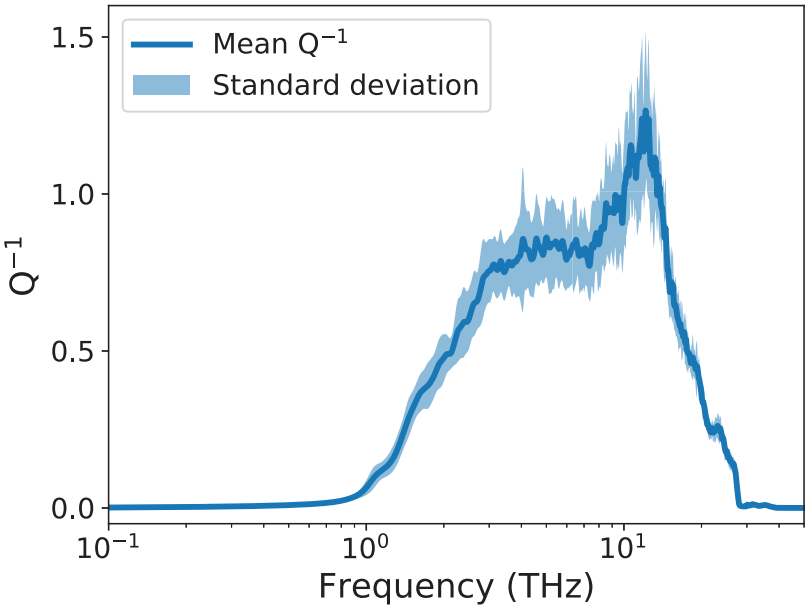

Figure 5.7: Mean energy dissipation as a function of frequency, calculated with Eq. 5.14 for 20 different SiO_2 glasses, with a thermostat frequency $\gamma = 1$ THz. The blue area represents the standard deviation of the energy dissipation computed on the 20 samples.

coefficients C_m over a frequency window of order γ. As will be emphasized in Fig. 5.8, C_m varies rapidly from mode to mode. Therefore, when γ is small, the non-affine parameter C_m is not averaged over a large enough window and the dissipation shows rapid fluctuations, as seen in Fig. 5.5. However, when γ increases and C_m is averaged over more modes, the dissipation spectrum becomes smoother but retains the same shape and features, as shown in Fig. 5.6, even near the peak of dissipation at 10 THz. This is typically true as long as ω remains in the frequency spectrum of the density of states and $\omega > \gamma$. Indeed, in the limit $\omega < \min(\gamma, \omega_m)$, Eq. 5.14 predicts $Q^{-1} \propto \gamma\omega$. This is visible in the inset of Fig. 5.6, where the dissipation below typically 1 THz scales with the frequency and friction. In this region outside the VDOS, the slow decay when $\omega \to 0$ is an artifact of the finite width of the Lorentzian and therefore, of the finite-friction thermostat. Equivalently, we can say that the fluctuations seen in Fig. 5.5 are a finite size effect, due to the fact that in the small systems considered here, there are not enough modes to obtain a smooth average of C_m. Larger systems with denser eigenfrequency spectra would show smoother dissipations at fixed γ. However, considering larger systems is difficult since diagonalizing the dynamical matrix becomes rapidly very computationally intensive.

Another way to limit the fluctuations is to average the dissipation spectrum over independent SiO_2 glassy configurations of same size, as done in Fig. 5.7 for 20 different samples. Fluctuations between different configurations are obvious, but the general shape remains the same and the

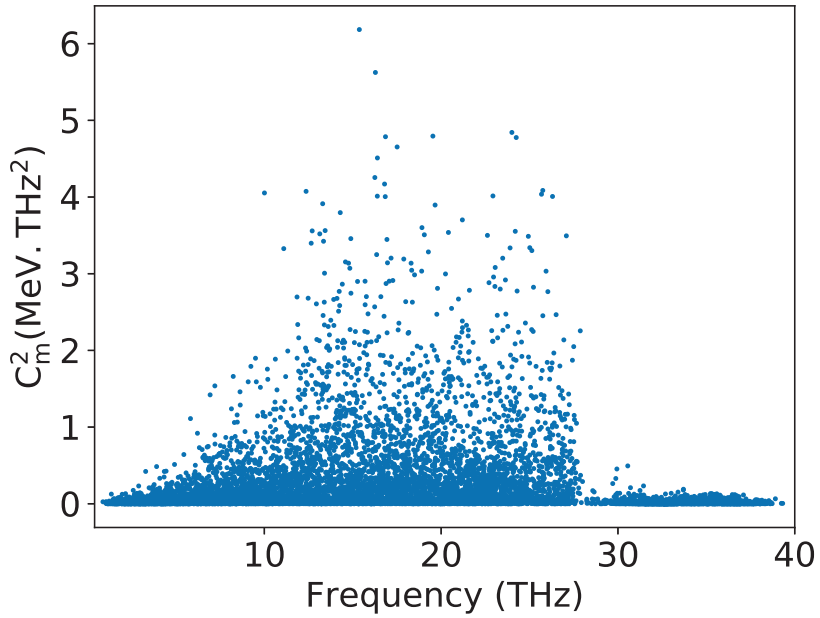

Figure 5.8: Square of the mode-dependent non-affine coefficient, C_m^2, computed from Eq. 5.13, as a function of the modes eigenfrequency.

average curve shows the same features as seen in Figs. 5.2 and 5.6.

5.3.3 Properties of C_m

From Eqs. 5.7 and 5.10, every eigenmode m has an influence on the total stress, through a non-affine contribution (departure of the mode from the affine macroscopic imposed displacement) whose amplitude is fixed by the mode-dependent parameter $C_m^{\alpha\beta}$. Fig. 5.8 shows $C_m^2 = (\sum_\alpha C_m^{\alpha\alpha})^2$, the square of the coupling parameter for isostatic deformations, as a function of the mode frequency. We see that (1) the coupling parameter varies rapidly from mode to mode, (2) C_m^2 vanishes at low frequencies for the long-wavelength modes, which approach plane waves and (3) C_m^2 falls abruptly down to zero above about 27 THz. This frequency corresponds in the VDOS of the present SiO_2 model (Fig. 5.3) to the beginning of the optic-like modes that compose the two high-frequency bands between about 27 and 40 THz [178, 41, 168]. In-between these two limits, in the so-called main band of the VDOS, there are very rapid variations, with many modes having very low C_m^2 values, and a few modes having very large values. Similar spectra with very rapid variations between modes are obtained with other applied strains, such as simple shear or uniaxial loading, although in both cases, C_m^2 does not vanish in the high-frequency band above 27 THz (see Sec. 5.3.4 for an explanation).

Still focusing on the case of isostatic deformations, the non-affine parameter C_m in Eq. 5.13 can

be rewritten as:

$$C_m = -\sum_{i\alpha} \Xi_i^\alpha \frac{e_i^\alpha(m)}{\sqrt{m_i}}, \tag{5.15}$$

with Ξ_i^α introduced in Ref. [105] as

$$\Xi_i^\alpha = \frac{\partial F_i^\alpha}{\partial \epsilon} = -\sum_{j\beta} D_{ij}^{\alpha\beta} R_{ij}^\beta, \tag{5.16}$$

where F_i^α is the force on atom i in direction α induced by an affine isostatic deformation ϵ applied to the initial configuration. The atomic vector field Ξ can be interpreted in two complementary ways. From the first equality in Eq. 5.16, Ξ corresponds to the atomic forces that induce non-affine displacements after application of an elementary affine deformation; Ξ is therefore a field of non-affine forces. From the second equality, the vector $\vec{\Xi}_i$ can be interpreted as a measure of the lack of symmetry of the atomic environment around atom i. This is particularly clear with a pair potential $\phi(r)$ because in this case, $\vec{\Xi}_i$ can be re-written as:

$$\vec{\Xi}_i = \sum_j \phi''(R_{ij}) \vec{R}_{ij}. \tag{5.17}$$

If the local environment of atom i is centro-symmetrical, there is for each atom j at $\vec{R}_{ij}$, an atom j' at $-\vec{R}_{ij}$ with an opposite contribution to $\vec{\Xi}_i$, which is therefore zero. This is true for other symmetrical environments, such as the regular tetrahedra surrounding Si atoms in SiO_2, since from Eq. 5.17, $\vec{\Xi}_i$ vanishes whenever atom i is at the center of gravity of its neighbors weighted by the bond strengths (measured by ϕ'').

In the general case (Eq. 5.9), the vector field $\Xi_{\alpha\beta}$ depends on the orientation of the applied strain $\epsilon_{\alpha\beta}$:

$$\Xi_{\alpha\beta,i}^\kappa = -\frac{1}{2}\sum_j \left(D_{ij}^{\kappa\alpha} R_{ij}^\beta + D_{ij}^{\kappa\beta} R_{ij}^\alpha \right). \tag{5.18}$$

This expression cannot be simplified as above, but it retains the property of vanishing in symmetrical local environments [105], justifying to qualify Ξ as an asymmetry vector field. Since C_m is the projection of eigenvector $e(m)$ on the asymmetry field Ξ (Eq. 5.15), we conclude that the modes that dissipate the most are those that best resemble Ξ (we neglected here the potential effect of varying masses, which can be incorporated if needed in the definition of Ξ). This field thus encodes the information about the structural features that control harmonic dissipation when measured with mechanical spectroscopy.

We finally note that the non-affine parameter can also be re-written in a third alternative way:

$$C_m = \sum_i \sum_{j\alpha} \xi^{\alpha}_{j\to i}(m) R^{\alpha}_{ij}, \tag{5.19}$$

with

$$\xi^{\alpha}_{j\to i} = -\frac{F^{\alpha}_{j\to i}}{s_m} = \sum_{\beta} D^{\alpha\beta}_{ij} \frac{e^{\beta}_j(m)}{\sqrt{m_j}} \tag{5.20}$$

where $F^{\alpha}_{j\to i}$ is the force on atom i in direction α due to the displacement of atom j when mode m has a mass-scaled amplitude s_m. Therefore, $\xi^{\alpha}_{j\to i}$ measures the sensitivity on the mode amplitude of the force on atom i due to atom j. This alternative expression shows the strong connection between dissipation and the forces induced in the glass by the eigenmodes. Such connection between force distributions and vibrational properties has recently been pointed out in the case of hard-sphere glasses [44]. In silica, the most important forces are supported by the Si-O bonds and form force chains supported by the SiO_2 skeleton. When non-affine atomic displacements are induced by an eigenmode, the force chains adopt a specific response, reflected by $\xi^{\alpha}_{j\to i}$, which varies very rapidly from mode to mode, like C_m.

5.3.4 Application to SiO_2

We concluded from the above discussion that inspecting the asymmetry field Ξ allows to identify the structural elements responsible for harmonic dissipation. To this end, we plot in Fig. 5.9 the Ξ field for isostatic deformations in a slab of SiO_2.

The Ξ vectors on the Si atoms (in black) are very small and hardly visible, as expected from their tetrahedral environment. Four-fold coordinated Si atoms therefore do not participate in harmonic dissipation. On the other hand, oxygen atoms are either two- or three-folded and have asymmetrical environments, resulting in finite Ξ vectors (in red). Moreover, O atoms form Si-O-Si bonds and we can see in Fig. 5.9 that in most cases, the Ξ vectors point towards the inside of the Si-O-Si bond, i.e. in a direction which bends the bond. This is readily understood from Eq. 5.17, where the O atom in a Si-O-Si bond has two Si neighbors at similar distances, resulting in a Ξ vector close to the bisector vector of the Si-O-Si angle. We checked this result numerically by computing in the inset of Fig. 5.9 the stereographic projection of the Ξ vectors (normalized to unity) of the O atoms in the basis formed by the rocking, bending and stretching vectors (V_{Rock}, V_{Bend} and V_{Stre}) of each Si-O-Si bond (see Fig. 5.3). Most Ξ vectors are oriented along the bending vector, which by construction, is the bisector vector of the Si-O-Si angle. Therefore, in the case of isostatic deformations, bending of the Si-O-Si bonds is the main contributor to harmonic dissipation in amorphous SiO_2.

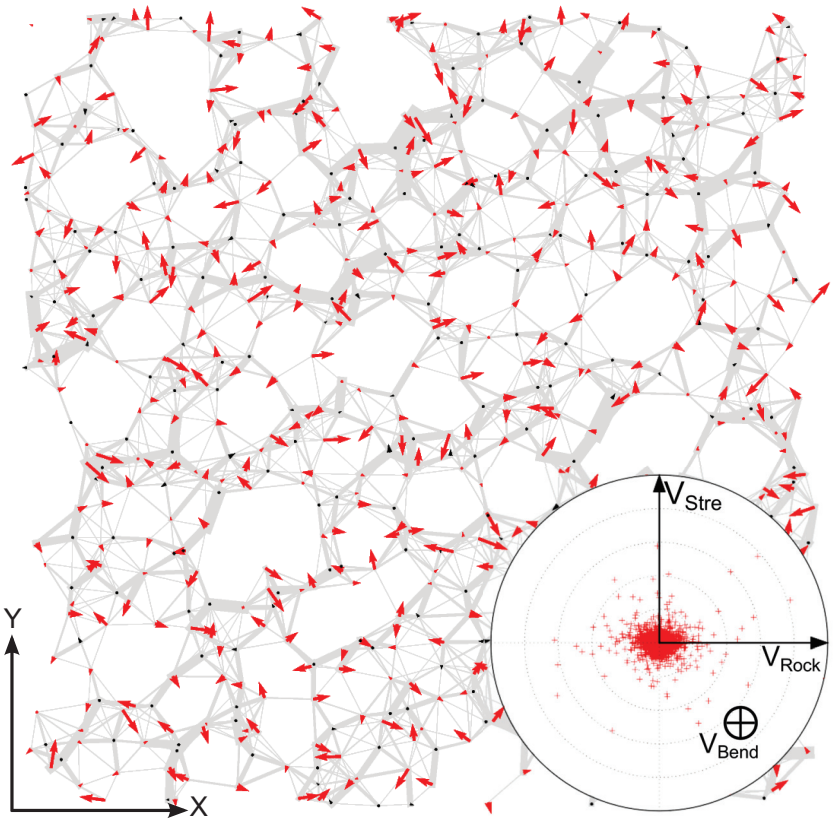

Figure 5.9: Asymmetry vector field Ξ in the case of isostatic deformations, represented in 2D projection for an 8 Å slab in a SiO_2 sample. Black arrows are for Si atoms, red arrows for oxygen atoms. The scaled forces $\xi^{\alpha}_{j\to i}$ for the mode of maximum dissipation are shown in grey, with a width proportional to their intensity. The inset shows the stereographic projection of the Ξ vectors (normalized to unity) of the O atoms in the basis formed by the rocking, stretching and bending vectors (V_{Rock}, V_{Stre},V_{Bend}) of each Si-O-Si bond.

For a general applied strain, the $\Xi_{\alpha\beta}$ field will remain small on the Si atoms and may take other orientations on the O atoms. As an illustration, we show in Figs. 5.11 and 5.10 the field $\Xi_{\alpha\beta}$ in the case of simple shear and the corresponding C^2_m. Dissipation is smaller than with isostatic deformations, as evidenced by the smaller length of the Ξ_{xy} vectors (their scale was tripled compared to Fig. 5.9) and the smaller C^2_m. Moreover, the difference between Si and O atoms is smaller, although O atoms still support on average larger Ξ_{xy} vectors than Si atoms. Finally, the distribution of orientations of the Ξ_{xy} vectors on O atoms is more spread, but the stereographic projection shows that they are predominantly oriented along V_{stre}. In simple shear, dissipation is therefore dominated by the stretching motion of the Si-O-Si bonds. As a consequence, the coupling parameter in shear, C^{xy}_m do not vanish but thrives in the high-frequency band above 27 THz as seen in Fig. 5.10, which is dominated by the stretching of the Si-O-Si bonds, as shown in the VDOS of Fig. 5.3.

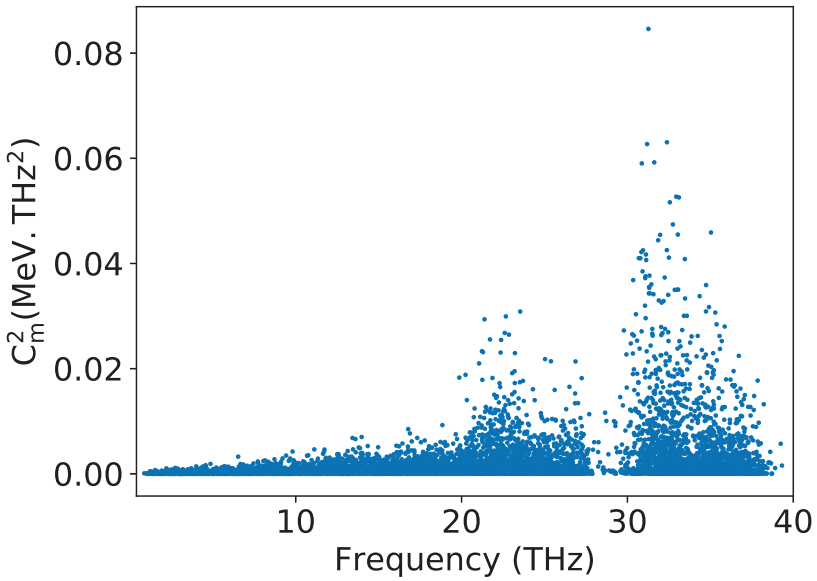

Figure 5.10: Square of the mode-dependent non-affine coefficient, C_m^2, computed from Eq. 5.13, as a function of the modes eigenfrequency for an applied shear strain ϵ_{xy}.

5.3.5 Application to Ta_2O_5

Despite the limited use of Ta_2O_5 glasses in high frequency devices, it is interesting to repeat the present study to get insights on the origin of harmonic dissipation in a glass possessing a SRO and MRO less organized than SiO_2. Performing mechanical spectroscopy in the case of isostatic deformation using both the M-BKS potential and a harmonic approximation on one of the samples synthesized in Chap 4, we obtain the dissipation spectrum showed in Fig. 5.12. On this figure is also represented here dissipation computed analytically using Eq. 5.14 which shows once again a very good agreement with the dissipation computed in the harmonic approximation. The spectrum presents similar trends to what was seen in SiO_2 with a strong increase of dissipation followed by two peaks at 12 THz and 20 THz before vanishing at high frequency together with the VDOS (see Fig. 4.8). Below the THz, a small discrepancy appears between the dissipation given by the M-BKS potential on the one hand and the harmonic calculation and analytic expression on the other hand. This disagreement, more noticeable than in SiO_2, reveals the existence of an anharmonic phenomenon such as Akhiezer damping, that appears to play a larger role in Ta_2O_5. Unlike the low frequencies presented in the previous chapter, where Ta_2O_5 dissipates more than SiO_2 (see Chap. 6), the peak of dissipation in Ta_2O_5 is four times lower, confirming that different phenomena are at work in the different ranges of frequency. Consistently, the mode-dependent non-affine coefficient, C_m^2, represented in Fig. 5.13, presents values two to three times smaller than in SiO_2 for hydrostatic deformation. We saw in the VDOS of Ta_2O_5 that below

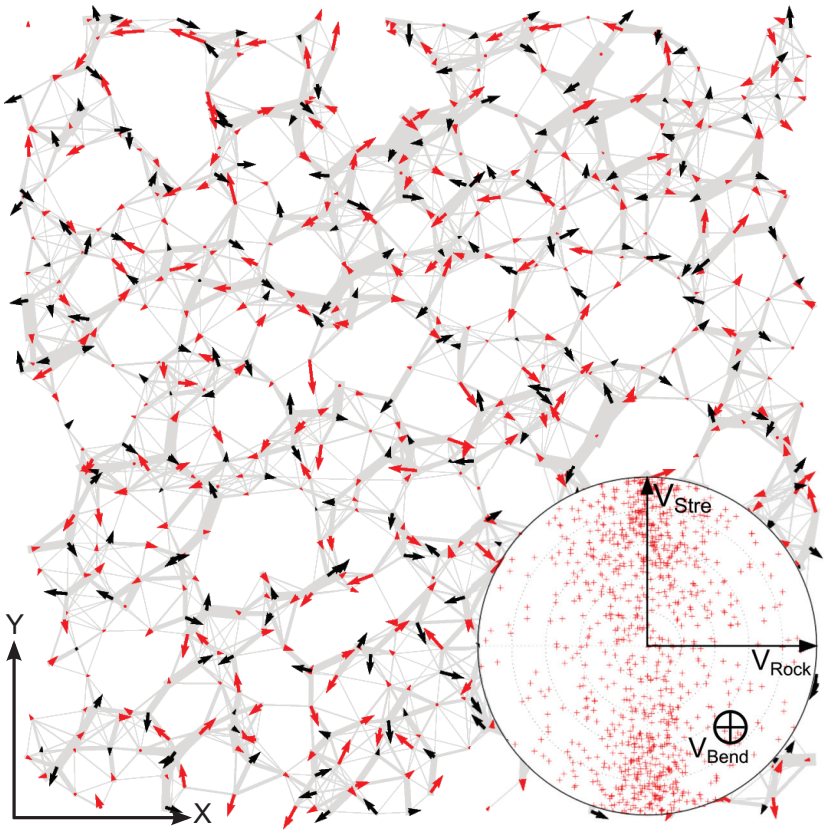

Figure 5.11: Asymmetry vector field Ξ_{xy} and its stereographic projection for an applied shear strain ϵ_{xy} in the same 8 Å slab as in Fig. 5.9, projected on the xy plane of the slab. The scale of the arrows is tripled compared to Fig. 5.9.

6 THz, the vibrations involve predominantly Ta atoms while above this frequency, the O atoms carry most of the vibrations. This duality is also observed in the C_m^2 which present small values below 6 THz and large values above this frequency. Once again, the oxygen atoms seem to be at the origin of dissipation. Above 25 THz, the C_m^2 do not collapse to zero like in SiO_2. This can be understood by looking at the partial VDOS for oxygen atoms in Ta_2O_5 (Fig 4.15): at high frequencies, the vibrations are not only carried by O-2Ta (similar to the vibration seen in SiO_2 at these frequencies) but also by O-3Ta stretching motion thus raising the average C_m^2 at high frequencies.

The asymmetry field, represented in Fig. 5.14, shows a similar picture as in SiO_2, with higher Ξ vectors on oxygen atoms in directions perpendicular to the bonds than for Ta atoms. We calculated the average amplitude of $\vec{\Xi}_i$ for two-folded oxygen atoms (69.4% of the oxygen atoms) and three-folded oxygen atoms and saw that it is in average 30% lower for the latter. Indeed, the three-folded oxygens are more completely surrounded by Ta atoms and are less likely to have a "soft" bending direction along which a non-affine motion is possible. Consistently with the

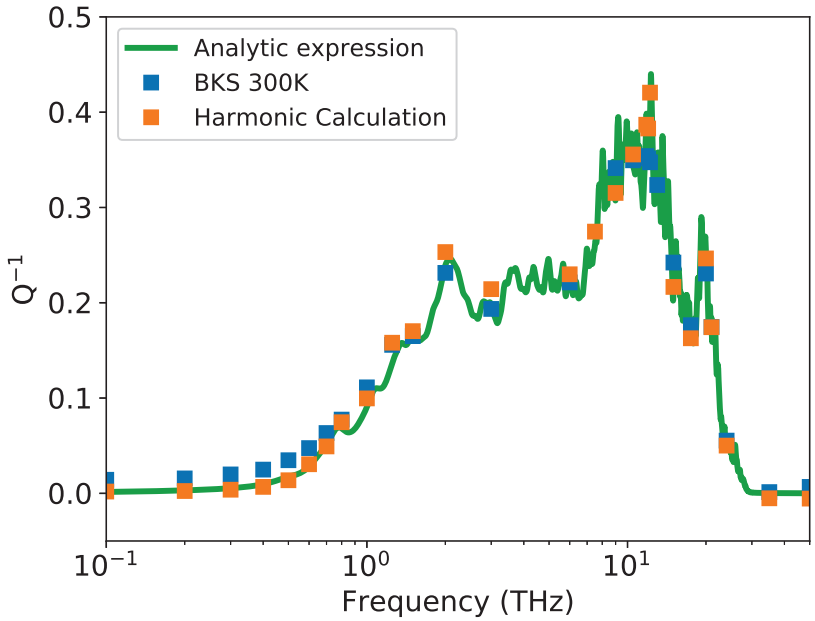

Figure 5.12: Energy dissipation in a Ta_2O_5 glass as a function of frequency computed with the non-linear BKS potential, the harmonic approximation of Eq. 5.6 and the analytical expression of Eq. 5.14. The same thermostat friction of 1 THz is used in all calculations.

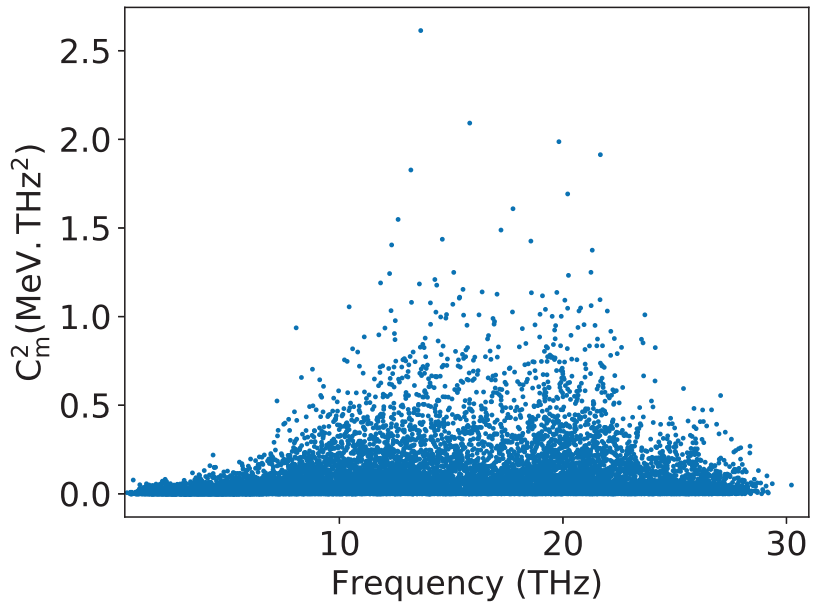

Figure 5.13: Square of the mode-dependent non-affine coefficient, C_m^2, computed from Eq. 5.13, as a function of the modes eigenfrequencies.

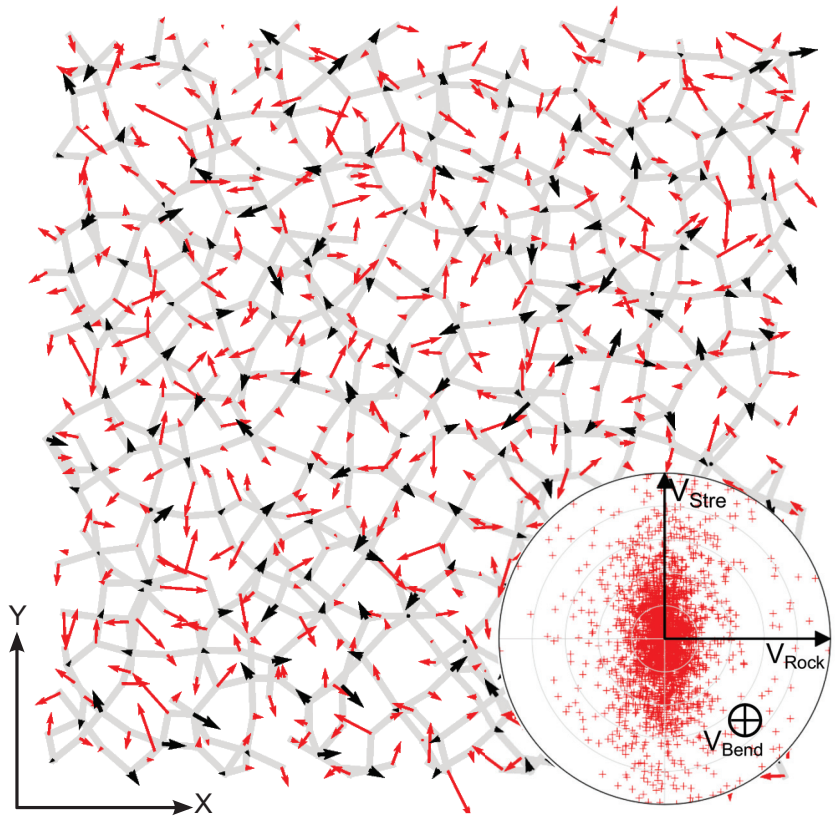

Figure 5.14: Asymmetry vector field Ξ in the case of isostatic deformations and its projection for two-folded oxygens, represented in 2D for an 6 Å slab in a Ta_2O_5 sample. Black arrows are for Ta atoms, red arrows for oxygen atoms. The atomic bonds are shown in grey.

disorganized SRO of Ta_2O_5, the projection of Ξ for two-folded oxygen on the rocking, stretching and bending directions in the inset of Fig. 5.14, reveals a more heterogeneous distribution than in SiO_2. The vectors are mainly oriented in the bending direction but the greater variety of local environments allows a wider direction of motion for the oxygens as showed by the spread, especially in the stretching direction. Concerning O-3Ta atoms, we projected Ξ on the stretching and bending motions as in Chap. 4, and saw that the vectors are equally shared between both directions (0.53 versus 0.47 respectively).

From this analysis, the peaks of dissipation at 12 THz and 20 THz can be explained: for two-folded oxygens, most $\vec{\Xi}_i$ are oriented along the bending direction of the Ta-O-Ta bonds, leading to high dissipation at frequencies where the motion of oxygens is along the bending direction (which peaks a little after 10 THz in the VDOS of Fig 4.15). Added to this dissipation is the one coming from the O-3Ta, whose Ξ are equally supported by stretching and bending motions. In the VDOSs, these motions form a broad maximum between 10 and 15 THz and a sharper peak at 20 THz.

5.4 Summary

Mechanical spectroscopy was used to compute dissipation at high frequencies in models of SiO_2 and Ta_2O_5 glasses. We have shown that the loss angle can be expressed analytically in the harmonic regime, characteristic of the high frequencies accessible to molecular dynamics simulations and inelastic x-ray scattering experiments. This analytical expression, written as a sum of damped harmonic oscillator, shows the role of the eigenmodes as energy dissipators. The sensitivity of the stress tensor to the vibrational modes is central to understanding high frequency dissipation. Up to now however, despite its formal evidence, a more quantitative connection between eigenfrequencies and the contribution of the corresponding eigenmodes to the global stress tensor is lacking due to the complex shape of the vibrations in amorphous solids. We have shown that an asymmetry vector field, which depends only on the equilibrium configuration of the glass, can be used to characterize the structural features that control harmonic energy dissipation. We recover here that force asymmetries are at the origin of non-affine displacements, as discussed in the works of Lemaître and Maloney [105] and Zaccone *et al.* [206], and that the non-affinity of the local fields in turn are responsible for energy dissipation, as computed by mechanical spectroscopy.

In the particular case of SiO_2 and Ta_2O_5, we have shown that the deformation of the Si-O-Si bonds and Ta-O-Ta bonds are the main contributors to energy dissipation. However, we should insist that since dissipation arises from the extended modes of the main band of the VDOS, dissipation is not related to the local vibration of a bond, but rather to the collective vibration of many Si-O-Si bonds (Ta-O-Ta bonds). With respect to the ring structure of silica, we have seen in Fig. 5.9 that in the case of isostatic deformations, the Ξ arrows point mostly towards the center of the rings, anticipating a potential connection between ring morphology and dissipation.

We also shown that internal friction is related to the forces induced in the glass skeleton by the eigenmodes, in connection with their effect on the stress tensor. This sensitivity of the stress tensor to the vibration modes of the system not only confirms that the force distribution affects vibrational properties, as pointed out in Ref. [44], but shows also that the components of the forces that are relevant for high-frequency internal friction are the non-trivial harmonic components induced by displacements along the eigenmodes of the samples.

CHAPTER 6

LOW FREQUENCY ENERGY DISSIPATION

After investigating the atomic origin of dissipation at high-frequency, we will now delve in the study of dissipation at low-frequency (from the Hz to the MHz), of interest for the gravitational wave detectors. In this frequency range, dissipation takes its root in Thermally-Activated Relaxations (TAR) involving from a few to a hundred of atoms. Studying the statistics of these TARs, their topologies, and their structural characteristics is necessary to apprehend the origin of low-frequency dissipation and model it, as done with the Two-Level System (TLS) model. As mentioned in Chap. 2, the TLS model has been used numerous times to fit experimental dissipation measurements in attempts to grasp its atomic origin. However, such studies had to make assumptions on the distribution and characteristics of the TLSs due to the lack of atomic-scale information provided by the experimental methods.

Accordingly, the present chapter is dedicated to the study of dissipation at low frequency in numerical SiO_2 and Ta_2O_5 glasses through the characterization of TARs observed during MD runs. These TARs are then used in the framework of the TLS model through their characteristic parameters (e.g. energy barrier and asymmetry) to predict dissipation. In this study, we take a fresh look at the TLS model by using a discrete formula not based on distributions of TLSs, but on individual events as observed in MD. Also, we discuss the different approximations used in the literature in the application of the TLS model to determine their robustness and we compare our numerical dissipation to experimental data in both SiO_2 and Ta_2O_5.

The present chapter is organized as follows: the first section is dedicated to the Two Level System model and to numerical methods while Secs. 6.2 & 6.3 describe their application to SiO_2 and Ta_2O_5 respectively.

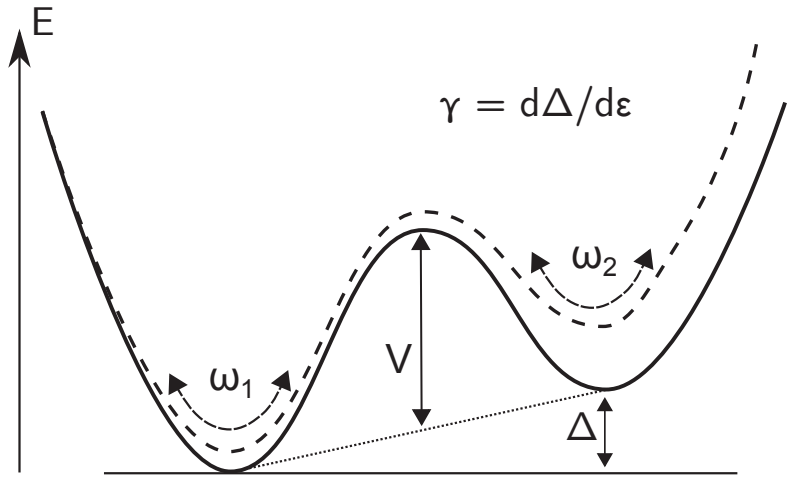

Figure 6.1: Schematic representation of a two-level system, with two metastable states connected by a double-well potential. The dashed curve represents the potential under a strain ϵ.

6.1 Methodology

6.1.1 The Two-Level System model

At low frequencies and temperatures (above typically 10 K), dissipation is due to the thermally-activated relaxation of TLSs, local bi-stable regions brought out-of-equilibrium by the propagating wave. Each TLS is characterized, as illustrated in Fig. 6.1, by the energy asymmetry between the TLS states (noted 1 and 2), $\Delta = (E_2 - E_1)$, the average energy barrier, $V = \frac{E_a - E_1}{2} + \frac{E_a - E_2}{2} = E_a - \frac{\Delta}{2}$ (where E_a is the activation energy), the attempt frequencies in the initial and final state, $\omega_{1/2}$, and the deformation potential, $\gamma = \frac{\partial \Delta}{\partial \epsilon}$, which represents the sensitivity of the asymmetry Δ on the strain ϵ. In the rest of the present study, the square of this last parameter will be averaged over all possible orientations of the TLS with respect to the propagating wave, and thus will be noted $\langle \gamma^2 \rangle$.

Using the harmonic Transition State Theory (hTST) [195], we can show that in the linear regime, dissipation is expressed as a sum over all the TLSs (see Appendix C for full analytical development):

$$Q^{-1} = \frac{1}{\mathcal{V} C} \sum_{\ell, TLS} A_\ell \frac{\omega \tau_\ell}{1 + \omega^2 \tau_\ell^2} \langle \gamma_\ell^2 \rangle \tag{6.1}$$

with

$$A_\ell = \frac{1}{4 k_B T} \mathrm{sech}^2 \left(\frac{\Delta}{2 k_B T} + \frac{1}{2} \ln \frac{\omega_{2,\ell}}{\omega_{1,\ell}} \right) \tag{6.2}$$

and the relaxation time

$$\tau_\ell = \frac{\pi}{\sqrt{\omega_{1,\ell}\omega_{2,\ell}}} \exp\left(\frac{V}{k_B T}\right) \operatorname{sech}\left(\frac{\Delta}{2k_B T} + \frac{1}{2}\ln\frac{\omega_{2,\ell}}{\omega_{1,\ell}}\right), \tag{6.3}$$

where $\mathcal{V}$ is the sample volume and C the appropriate elastic modulus (longitudinal or shear modulus for longitudinal and transverse waves, respectively) .

Eq. 6.1 is similar to the classical expression of Jackle *et al.* [92], used by several authors to extract TLS characteristics from experiments [187, 28, 193]. However, while as mentioned in Chap. 2, such inverse calculations require simplifying assumptions, e.g. replacing the relaxation time and deformation potential by their averages, no such simplification is needed here. For instance, we can account for the fact that the attempt frequencies $\omega_{1/2}$ are a priori different in both states of the TLS. Details of the calculations are given in the Appendix C, where care was taken to account for the tensorial nature of the stresses and strains. This results in particular in expressions of the longitudinal and transverse mean square deformation potential:

$$\begin{aligned}
\langle\gamma^2\rangle_L = \quad & \tfrac{1}{5}(\gamma_{XX}^2+\gamma_{YY}^2+\gamma_{ZZ}^2) + \tfrac{2}{15}\big(\gamma_{XX}\gamma_{YY}+\gamma_{XX}\gamma_{ZZ}+\gamma_{YY}\gamma_{ZZ}+2\gamma_{XY}^2+ \\
& 2\gamma_{XZ}^2+2\gamma_{YZ}^2\big), \\
\langle\gamma^2\rangle_T = \quad & \tfrac{1}{15}(\gamma_{XX}^2+\gamma_{YY}^2+\gamma_{ZZ}^2) - \tfrac{1}{15}(\gamma_{XX}\gamma_{YY}+\gamma_{YY}\gamma_{ZZ}+\gamma_{ZZ}\gamma_{XX}) + \\
& \tfrac{4}{15}\big(\gamma_{XY}^2+\gamma_{XZ}^2+\gamma_{YZ}^2\big),
\end{aligned} \tag{6.4}$$

which depend on the full deformation potential tensor

$$\bar{\bar{\gamma}} = \frac{\partial\Delta}{\partial\bar{\bar{\epsilon}}}. \tag{6.5}$$

Consistently, the longitudinal and transverse (or shear) elastic moduli are averaged using similar expressions. Strains were applied to the cells to compute the average longitudinal and shear moduli giving 135.9 and 39.6 GPa for SiO_2 and 205.2 and 45.0 GPa for Ta_2O_5, respectively.

6.1.2 Exploring the potential energy landscape

To generate representative samples of TLSs, 115 glassy structures of silica were synthesized using the protocol and BKS potential described in Chap. 3 by quenching a melt from 5,000 K down to 0 K at a constant quench rate of 10^{11} K.s^{-1}. All samples are cubic with a size $L = 34.77$ Å and contain 3,000 atoms (1,000 silicon and 2,000 oxygen atoms) at a density of 2.4 g/cm^3, which corresponds to zero average pressure with the present potential [96]. Average coordination numbers are shown in Tab. 6.1, highlighting that the samples contain very few coordination defects, although we will see in the following that these have a strong influence on the low-frequency dissipation.

Silicium	%	Oxygen	%
Coord. 4	99.7	Coord. 1	0.1
Coord. 5	0.3	Coord. 2	99.7
		Coord. 3	0.2

Table 6.1: Average first-neighbor coordination numbers in SiO_2.

59 samples were also synthesized following the same protocol but with a faster quench rate of 10^{12} K.s^{-1} to test for potential effects due to relaxation. For Ta_2O_5, 59 glassy structures where obtained following the protocol already used in Chap. 4, with a size $L = 34.2$ Å for 2999 atoms (857 tantala and 2142 oxygen atoms). The Ta_2O_5 glasses were obtained using a quench rate of 10^{12} K.s^{-1}.

To identify the TLSs present in our glasses, we use both MD and the Activation Relaxation Technique (ART) described in Sec. 3.3.1. For the exploration based on MD, we generated, for each of the samples, 1,000 trajectories at constant temperature (1,000 K), starting with different initial random velocities, during which energy was quenched every 40 fs to check if the system had changed IS. Then, the climbing NEB algorithm was employed to find the minimum energy path between the intial and final ISs, from which the energy asymmetry (Δ) and energy barrier were obtained (in Appendix B, we propose a way to visualize the organization of the ISs in the 3N dimensions of the PEL). We checked that the energy asymmetries depend negligibly on the cell size by surrounding the final configurations by copies of the initial configuration and re-relaxing this larger system. We found relative variations of Δ below 3%. As mentioned in Chap. 3, only low energy barriers are found because of the Boltzmann factor. In the past [146, 78], rather low search temperatures were used (100-600 K), strongly limiting the range of activation energies. Here, we used a higher temperature, 1,000 K (the glass-transition temperature for the present potential is 1300 K), to obtain a larger range of activation energies and try to probe all relevant barriers playing a role in dissipation.

Concerning the ART method, a subset of 60 samples were randomly selected amongst the SiO_2 samples. ART is efficient to find transitions as it is not limited by notions of temperature or dynamics, therefore, a larger number of initial samples is not required. For each sample, 2,000 ART searches were conducted. For half of them, the initial displacement vector $\vec{U}$ was centered on an oxygen atom, while for the other half, $\vec{U}$ was centered on an Si atom. When centered on an oxygen atom, $\vec{U}$ is defined as being non-zero only for the three components of the chosen oxygen atom. When centered on a Si atom, the components of $\vec{U}$ are chosen non-zero for all the atoms in the first shell of neighbors of the selected atom since we realized that transition involving Si atoms are more collective than these centered on O atoms.

6.1.3 Deformation potential and attempt frequency

Two more parameters need to be computed to predict the dissipation from the TLS model: the deformation potential tensor, $\gamma_{ij} = \partial\Delta/\partial\epsilon_{ij}$, which measures the sensitivity of a TLS to the strain of the propagating wave and $\omega_{1/2}$, the attempt frequencies in the initial and final configurations. To obtain the components of $\bar{\bar{\gamma}}$, no additional computation is required as from Eq. C.5 we have

$$\gamma_{ij} = \Delta\sigma_{ij} * \mathcal{V} \tag{6.6}$$

where $\Delta\sigma_{ij}$ is the total internal pressure difference between states 1 and 2 of the TLS. We checked by using a finite-difference calculation that this expression is equivalent to the definition in Eq. 6.5.
Finally, the attempt frequencies in the initial and final configurations of each TLS, ω_1 and ω_2 (see Fig. 6.1) were computed using the hTST [195] from the ratio of the real, strictly positive, eigenfrequencies in the initial and activated states of each transition:

$$\omega_{1/2} = \frac{\prod_{i=1}^{3N-3} \omega_{1/2,i}}{\prod_{i=1}^{3N-4} \omega_i^\star}, \tag{6.7}$$

using an exact diagonalization of the dynamical matrix of the initial, final and activated configurations of each TLS.

6.2 The case of SiO_2

6.2.1 Thermally Activated Relaxations in SiO_2

From the above-mentioned searches result 668 transitions or 1.93 transitions/1000 atoms ($1.4\ 10^{-4}$ TLS/Å^3) with the MD method and 22,796 TARs with ART. This gap in the number of transitions illustrates the difference of efficiency between these two techniques. Compared to the experimental density of $7.8\ 10^{-5}$ TLS/Å^3 obtained by Vacher *et al.* from a fit of attenuation data with the TLS model (see Eq. 8 of Ref. [193]), the present density is about twice higher. However, as we will see while studying dissipation, only a limited fraction of the TLSs contribute significantly to the dissipation and the density of TLS observed experimentally does not take into account the TLSs that do not contribute to dissipation. To check the possible influence of the quenching rate on the transitions density, we performed searches using the MD method on the 59 SiO_2 samples quenched at 10^{12} K/s and found 1649 events (9.31 transitions/1000 atoms). The magnitude of this increase in TLS density with decreasing quenching rate indicates that the existence of TLSs and their statistical distribution appear to vary greatly with respect to the relaxation of the glass and thus with defects such as ill-coordinated atoms.

On Figs. 6.2 and 6.3 are represented Δ, the TLS asymmetries, as a function of V, the energy barrier, for the 668 transitions found using MD and the 22,796 obtained with ART. For transitions found with MD, a higher density of events is seen at lower V, which is coherent with the fact that barriers are overcome with a probability $\propto \exp(-V/k_bT)$. A strong correlation is observed between V and Δ. Indeed, from its definition, Δ cannot be larger than $2V$ (marked by an orange dashed line) nor smaller than $-2V$ as $V = E_a - \Delta/2$. Therefore, the distribution of energy barriers, $g(V)$, and asymmetries, $f(\Delta)$, cannot be considered independent as done in the past [193, 78]. Only a few transitions show a negative asymmetry, which proves that the glasses were properly relaxed since very few lower energy states can be reached without overcoming a consequent energy barrier. Looking now at the shape of the distribution of barrier heights, $g(V)$, in the upper inset, we propose a Gaussian function $g(V) = N_g \exp(-V^2/V_0^2)$ as a fit with $N_g = 152$ and $V_0 = 0.47$ eV (orange curve in the inset of Fig. 6.2) similar to the fit also proposed in Refs. [187, 193]. For the distribution of asymmetries, $f(\Delta)$, both Gaussian and stretched exponential functions were also proposed [193, 187]. A simple decreasing exponential $N_d \exp(-\Delta/\Delta_0)$ with $N_d = 170$ and $\Delta_0 = 0.4$ is here more appropriate.

Looking at the transitions obtained with ART in Fig. 6.3, we first see that the bulk of the transitions are not at low V but between 1 and 4 eV. A second feature is the subset of transition for which $\Delta = 0$ eV seen between $V = 2$ eV and 10 eV. These transitions are symmetric and correspond to jumps of two or three oxygens atoms that result either in the exchange of position of the oxygens or in a rotation of the oxygen atoms around an Si atom. These motions do not create coordination defects as they are symmetric events, however, they imply the transient breaking of several Si-O bonds and therefore, their energy barriers are high. In the context of energy dissipation, an issue appear with the set of transitions obtained using ART: Eq. 6.1 says that the contribution of TLSs to dissipation is proportional to $\text{sech}^2\left(\frac{\Delta}{2k_BT} + \frac{1}{2}\ln\frac{\omega_2}{\omega_1}\right)$. As the function $\text{sech}^2(x)$ goes rapidly to zero when x increases, it imposes a cut-off on Δ. Roughly speaking, all TLSs with $|\Delta| > 0.2$ eV will contribute little to none to the dissipation. Looking at the distribution of transitions presented in Fig. 6.3, we see that only a fraction (8%) of them are below this limit, most of which have a V, and thus a relaxation time, too large to play a role in the frequency range of application. In addition, almost all the transitions which have a small Δ and an appropriate V were also obtained using the MD method. Since ART spends most of its time finding irrelevant transitions with high energy barriers and asymmetries, only the transitions found using MD will be considered in the rest of the present study during which they will be referred to as TLSs.

The longitudinal and transverse sensitivity to the strain, γ_l^2 and γ_t^2 are represented in Figs. 6.4 and 6.5 as a function of V. The similarity between the graphs of γ_l^2 and γ_t^2 comes from the similarity between Eq. C.23 and C.28, however γ_t^2 presents lower values at all V, consistent with the lower value of the transverse modulus. For both γ_l^2 and γ_t^2, the bulk of the data are

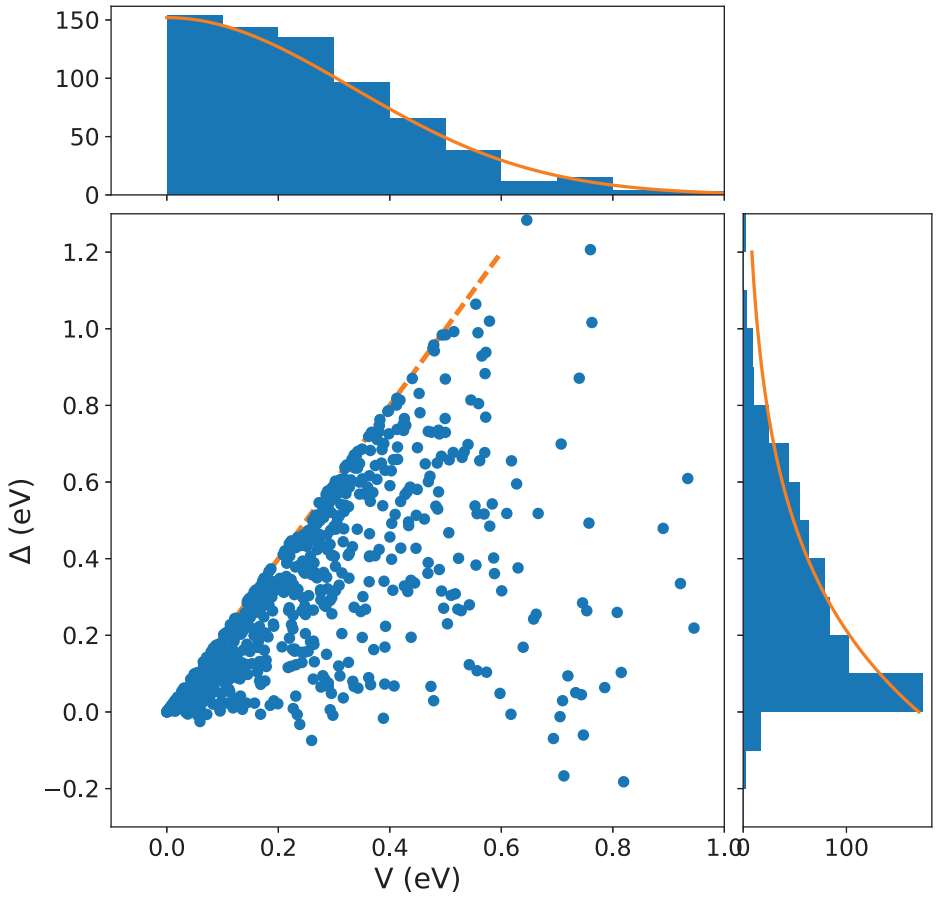

Figure 6.2: Asymmetry Δ as a function of the TLS energy barrier $V = E_a - \Delta/2$ for the 337 TLSs found using the MD method. The orange dashed line represents the maximum possible asymmetry $\Delta = 2V$ for a TLS of energy barrier V. The upper and right panel represent the histograms for the energy barriers and asymmetries $g(V)$ and $f(\Delta)$ respectively (see text for details).

not consistent with experimental values (1.08 eV^2 and 0.42 eV^2 for longitudinal and transverse respectively [51]) with a constant overshot of about two orders of magnitude. However, these experimental data were obtained performing extremely low temperature acoustic measurements in the quantum regime (0.1 to 1.5 K) and therefore are not pertinent for the present TLS distribution. We note also that in the present sample, the barriers with the lowest V, which are relevant at very low temperature have indeed low coupling parameters, consistent with experimental data.

The attempt frequencies in the initial and final state, $\omega_{1/2}$, plotted in Figs. 6.6 and 6.7, are not simple functions of V either. A major part of the values are gathered around a median at 7 THz while the rest are homogeneously spread and do not appear to vary with V. A few extreme values increase the average away from the median, with an average of 25.0 THz, slightly above

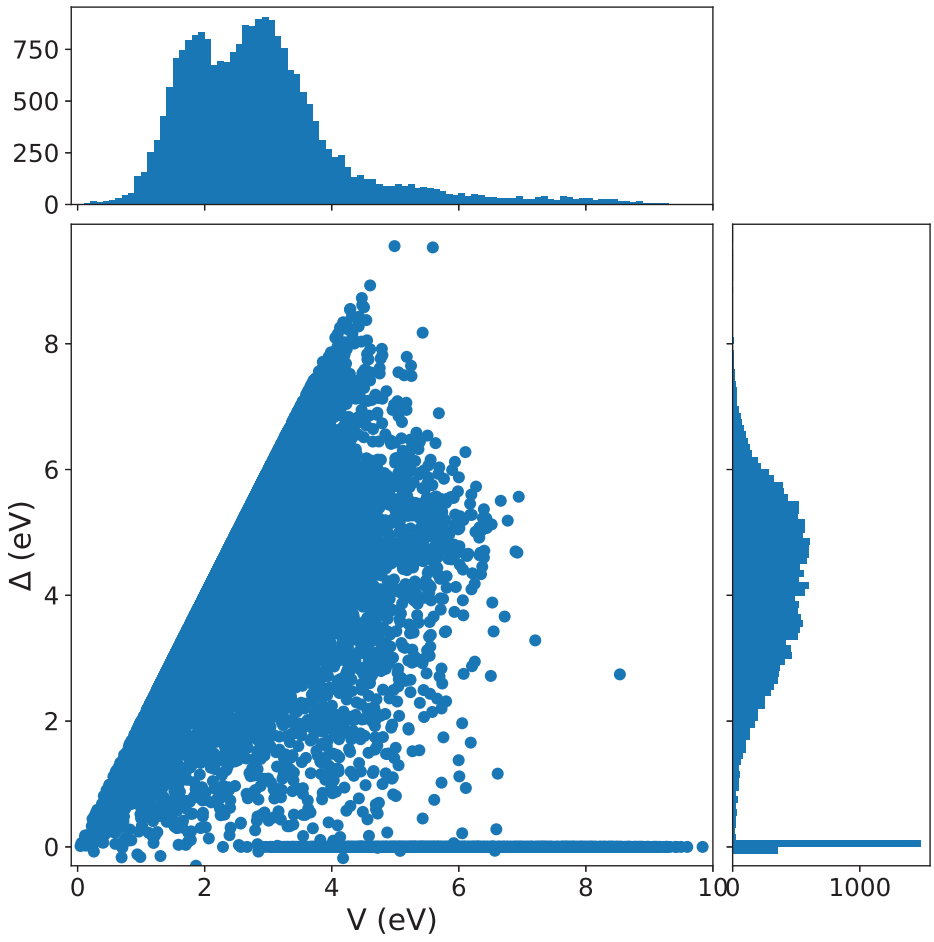

Figure 6.3: Asymmetry Δ as a function of the TLS energy barrier V for the 22,796 TLSs found using the ART.

experimental estimates at 10.5 and 18.9 THz [193, 123].

Inspecting closely the atomic motions taking place in our set of TLSs, we notice that each TLS can be sorted in one of the three following categories that will be referred to as TLS of Type I, Type II and Type III respectively (it is important to note that there is no systematic way to classify TLSs, and therefore, the following observations were obtained by studying a subset of TLSs for which types were determined "by hand"):

(1) In Type I, the most frequently observed in our numerical glasses, the maximum displacement is centered on an Si atom as illustrated in Fig 6.8. These Type I TLS can be understood as a change of tetrahedron from a Si atom. For such an event to happen, the O atom in the direction of the Si displacement or the O atom from which the Si is coming has to be ill-coordinated (one- or three-folded) as a two-folded O on both sides would not allow a displacement of the Si atom. Consequently, these Type I TLS are centered on coordination defects and should not be observed

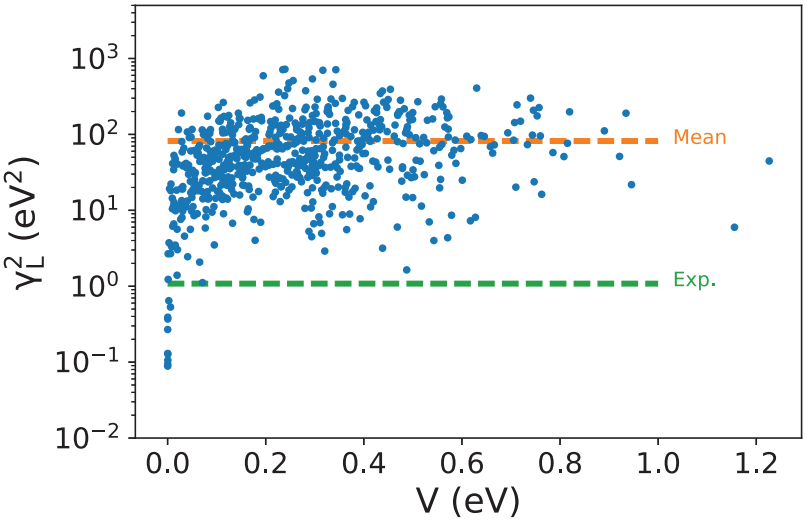

Figure 6.4: Longitudinal sensibility to the strain calculated from Eq. C.23 as a function of V, the green dashed line represents the experimental value for SiO_2 [51] while the orange line represents $\langle \gamma_l^2 \rangle$.

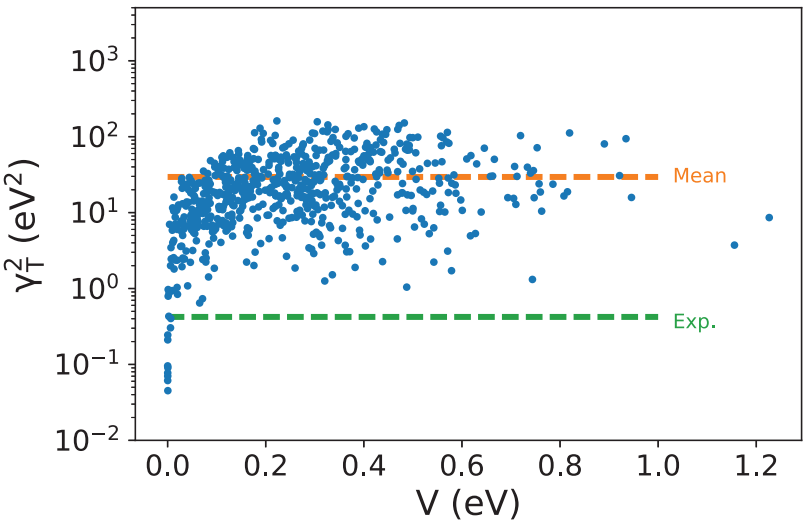

Figure 6.5: Transverse sensibility to the strain calculated from Eq. C.28 as a function of V, the green dashed line represents the experimental value for SiO_2 [51] while the orange line represents $\langle \gamma_t^2 \rangle$.

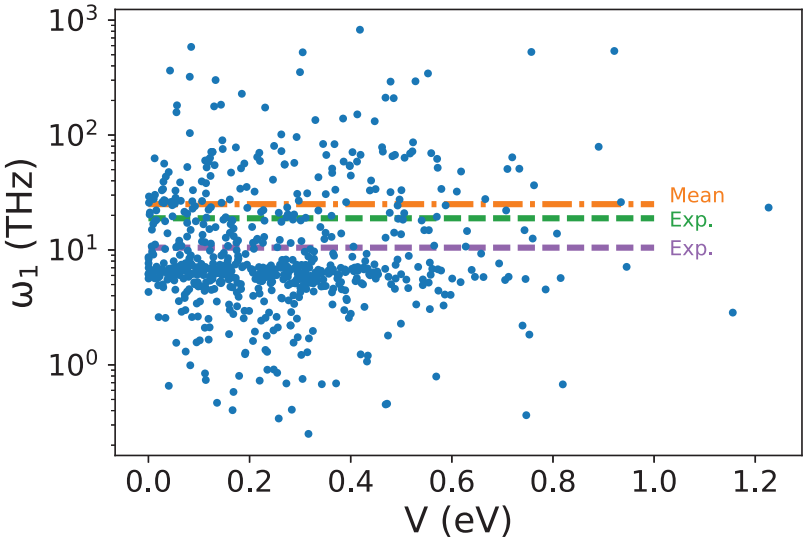

Figure 6.6: Attempt frequency in the first well of the TLSs, ω_1, as a function of V, the orange dashed line represents the average while the green and purple dashed lines represent the experimental values for SiO_2 deposited by IBS [123] and vitreous bulk SiO_2 respectively [193].

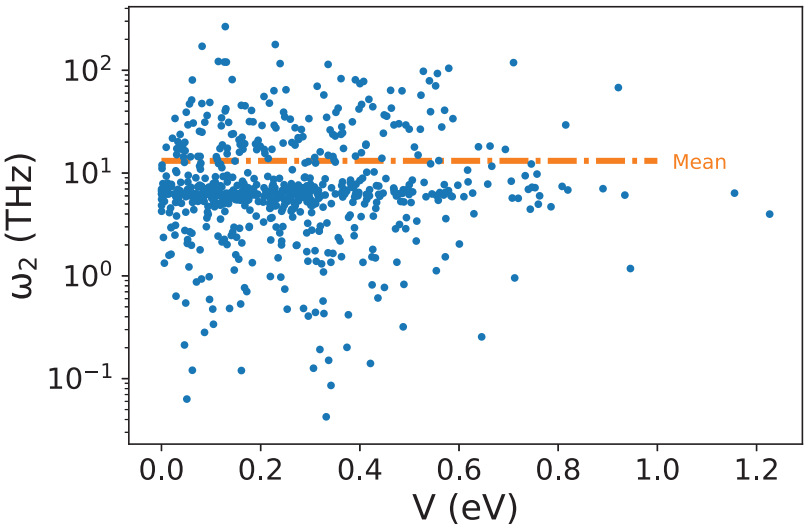

Figure 6.7: Attempt frequency in state 2 of the TLSs, ω_2, as a function of V, the orange dashed line represents the average.

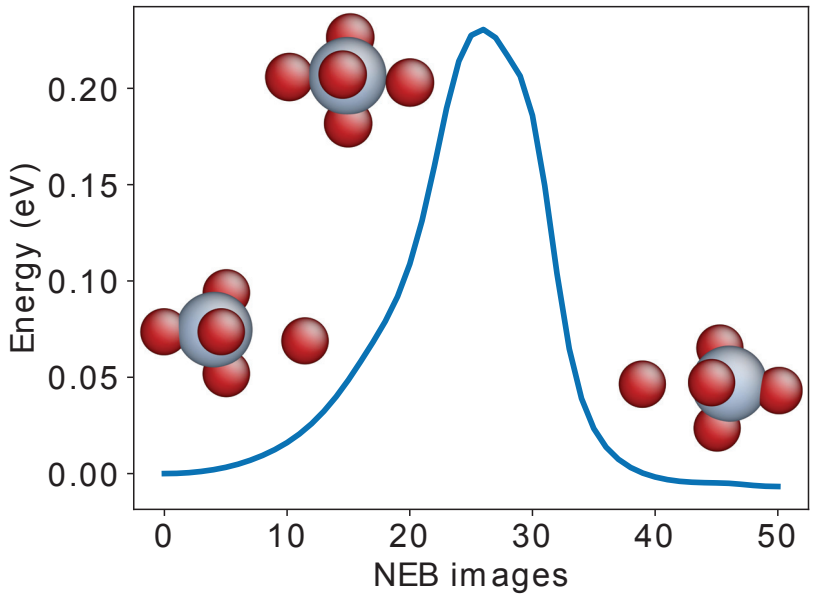

Figure 6.8: Potential energy along the minimum energy pathway for a TLS of type I. The three snapshots show from left to right: the initial configuration, the saddle point and the final configuration of the TLS. The oxygen and silicon atoms are depicted in red and gray respectively.

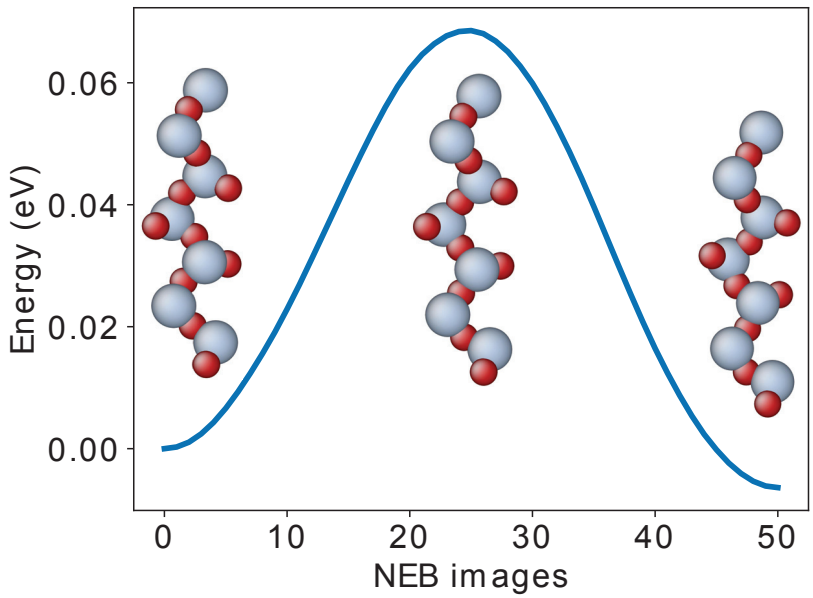

Figure 6.9: Potential energy along the minimum energy pathway for a TLS of type II (on the right). The three snapshots show from left to right: the initial configuration, the saddle point and the final configuration of the TLS. The oxygen and silicon atoms are depicted in red and gray respectively.

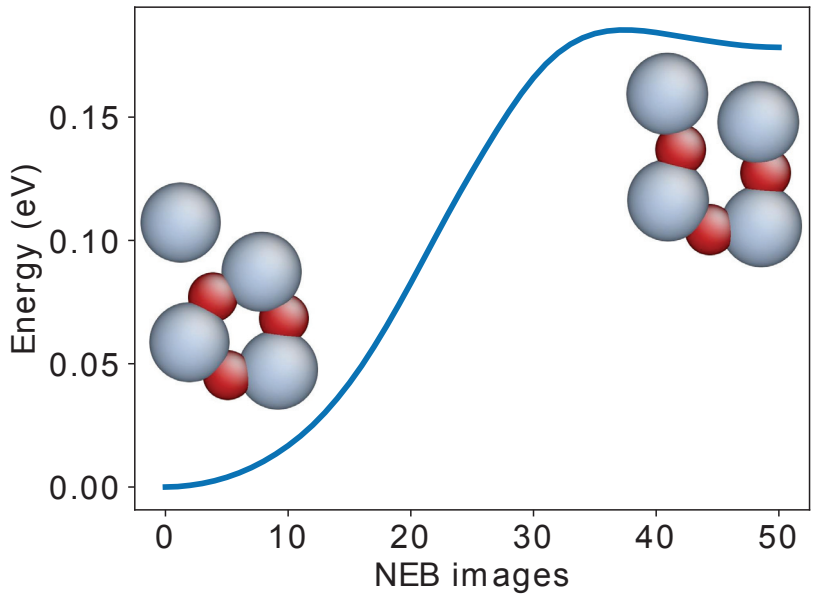

Figure 6.10: Potential energy along the minimum energy pathway for a TLS of type III. Only the initial and final configuration of the TLS are represented as the saddle point is almost identical to the final configuration.The oxygen and silicon atoms are depicted in red and gray respectively.

experimentally as the glasses produced experimentally are more relaxed than numerical glasses by several orders of magnitude. Similar atomic motions have already been observed in alumina by Paz *et al.* [141] where an Al atom can oscillate from one O to another. These events induce a significant displacement for less than a dozen atoms and thus are very localized. Looking at the energy profile of the double-well potential on Fig. 6.8, we see a highly symmetric double-well reflecting the structural symmetry between the initial and final configurations. The maximum energy is reached when the Si atom has 5 neighbors, that is when the Si atom is in the plane formed by the three oxygens separating the two tetrahedra.

(2) The second category, encountered slightly less often than Type I involves mainly O displacements. In these events, as represented in Fig 6.9, several SiO_4 tetrahedra rotate leading the simultaneous jump of O atoms from one side of their Si-O-Si bonds to another. These events have already been observed in SiO_2 and rather than being described as the rotation of tetrahedra, they have been referred to as jumps around "floppy Si-O-Si bridge" [146, 144]. These TLS of Type II are delocalized and involve quasi 1D chains of atoms or rings. As the jump of all the oxygen is simultaneous, the energy profile shows an energy barrier not higher than a few hundreds of meV, the maximum of energy happening when the oxygens are compressed in the middle of their Si-O-Si bonds. The energy profile also shows once again a symmetric double-well, mirroring the symmetry present between the initial and final atomic configurations. These TLS of Type II are

of main interest since they are symmetric and do not rely on coordination defects, therefore, they contribute to the dissipation and are likely to be probed in experimental acoustic measurements. The TLS showed in Fig. 6.9 in particular can be seen as the canonical TLS mentioned in the literature [30, 146, 193] as it is almost perfectly symmetric and presents a small energy barrier, 65 meV. This TLS is therefore a good representative of the TLS pointed at when studying dissipation in silica. It is interesting to notice that similar motions have been observed in the past during the study of atomic vibration in silica glasses where low frequency modes were understood as rotation of SiO_4 tetrahedra [30, 181].
(3) The third category encompassed events in which an O atom carries the highest displacement, going from being two-folded to three-folded (3 Si neighbors) or change one of its Si neighbors (an Si atom ends up five-folded) as shown in Fig 6.10. These Type III TLSs are highly unstable and asymmetrical ($\Delta \approx V$) as can be seen from the energy profile represented in Fig. 6.10. This high asymmetry makes Type III TLS contribute very little to dissipation. These TLSs are more localized than Type II and involve usually less than 20 atoms. From the three types of TLS, Type III shows the highest diversity in structural topologies and can be difficult to tell apart from Type II as they also involve oxygen displacements and are sometimes as delocalized. To verify the stability of these TLSs, we took the atomic configuration corresponding to the system in the excited state of the TLS and applied a deformation of amplitude $\epsilon = 0.008$ to the simulation cell along one of the three axis X, Y or Z followed by an energy minimization. Most of the Type III TLSs fell back in the initial state of the TLS, showing that the very existence of Type III is not guaranteed when an acoustic waves propagates in the medium.

6.2.2 Application of the TLS model and Approximations

Fig. 6.11 represents the Q^{-1} computed from Eq. 6.1 for a longitudinal wave at 10 kHz. Dissipation is qualitatively similar for a transverse wave at the same frequency and thus will not be presented here. In addition, dissipation is not represented below 10 K as quantum effects not treated in the present study play a major role at such temperatures. It has to be noted that, to our knowledge, it is the first time that the TLS model is applied on discrete TLSs without using approximations on the TLSs distribution or their parameters while considering V and Δ correlated. The present Q^{-1} curve presents peaks corresponding to dissipation induced by individual TLSs due to the sum over TLSs in Eq. 6.1. Even if 668 TLSs were obtained, only 41 of them present a maximum above 10^{-5} and therefore contribute significantly to dissipation and the finite size of the samples can be seen, many more events would be needed to obtain a smooth curve. As mentioned in the previous section, events based on coordination defects such as three-folded O or three- and five-folded Si that are not expected to be seen experimentally (Type I TLSs in the previous section). When these TLSs are not taken into account in the calculation of Q^{-1} (by removing TLS in which an

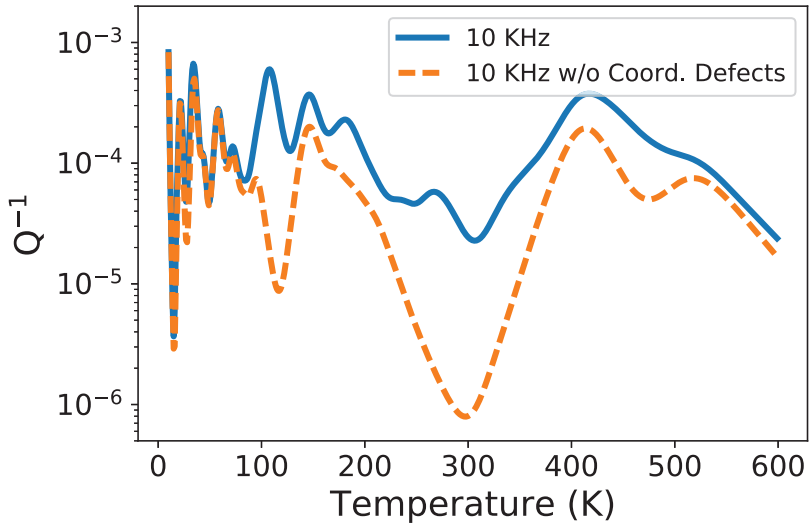

Figure 6.11: Q^{-1} as a function of the temperature at 10 kHz. The orange dashed line is the dissipation computed when removing the TLSs based on a coordination defects such as five-folded Si atoms.

ill-coordinated atom moves more than 0.2 Å), dissipation is lower above 100 K especially in the 250 to 350K range. Therefore, the action of TLSs based on defects appears to affect the dissipation of the glass at high temperatures, which is expected since Type I TLSs tend to have larger energy barrier than Type II and therefore induce dissipation at higher temperature.

We now consider Q^{-1} computed using different approximations, some of them used in the literature [187, 28, 193, 78]. In the present analytical development of the TLS model, we introduced ω_1 and ω_2, the attempt frequencies in the initial and final states of the TLS whereas in the original TLS model, only the average attempt frequency was consider (the original formula is obtained from the present model with $\omega_1 = \omega_2$) [92]. A second approximation was introduced by Hamdan *et al.* [78] who argued that calculating the attempt frequency for all TLSs was too computer intensive and therefore preferred to consider an averaged value, $\langle\omega_1\rangle$, computed on a subset of events (with the present data set $\langle\omega_1\rangle = 25.0$ THz). Fig. 6.12 compares the dissipations obtained in these three cases and shows curves of similar profiles as expected from the rather homogeneous distribution of $\omega_{1/2}$ seen in Figs. 6.6 and 6.7. Indeed, $\omega_{1/2}$ enters Eq. 6.1 only as a pre-exponential factor and has therefore a limited role. These approximations are therefore quite reasonable.

Fig. 6.13 compares the dissipations computed using selection rules on the asymmetries of the TLSs, Δ. The first of the two approximations was introduced in Refs. [72, 193] to integrate the TLS model analytically and obtain a fit to attenuation measurements. This approximation consists in replacing $\mathrm{sech}(\Delta/2k_bT)$ in Eq. 6.1 by 0 for TLSs whose asymmetry is higher than $2k_bT$

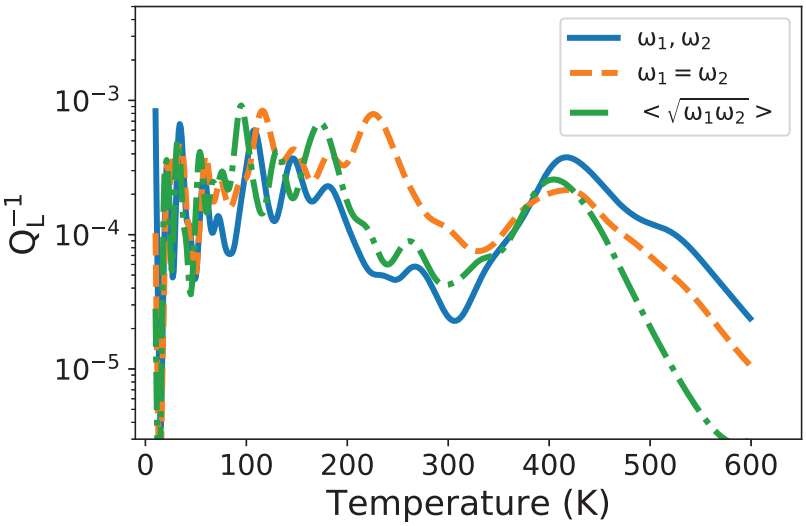

Figure 6.12: Q^{-1} at 10 kHz as a function of the temperature considering two different approximations concerning ω. The orange dashed line corresponds to dissipation computed considering that the attempt frequency in the two states of the TLSs are equal while the dash-dotted green line considers an average value for the attempt frequency.

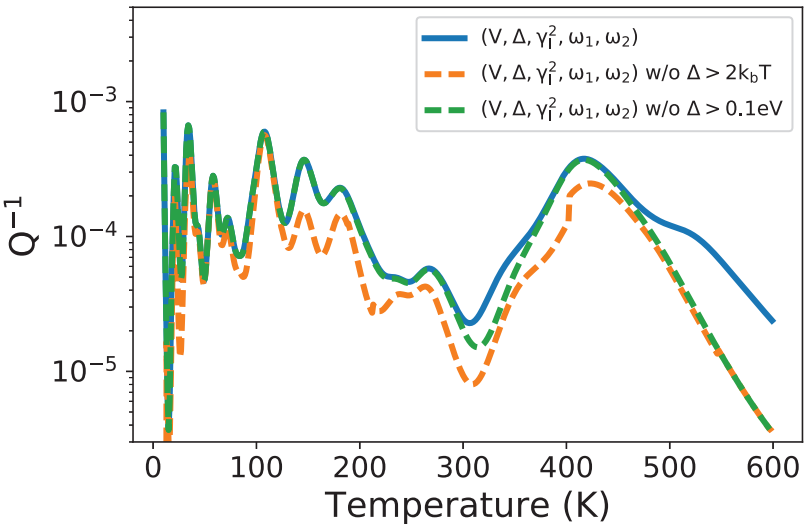

Figure 6.13: Q^{-1} at 10 kHz as a function of the temperature considering two different approximations concerning Δ (see text for details).

and by 1 otherwise. This approximation is based on the observation that the function $\mathrm{sech}^2(x)$ varies rapidly from one to zero when x increases. A second approximation was introduced in Refs. [78, 189] and consists in ignoring all TLSs whose asymmetry are higher than 0.1 eV ($|\Delta| > 0.1$ ev). This approximation was introduced based on two arguments: (1) as said above, the $\mathrm{sech}^2(x)$ function imposes a cut-off on the contribution of TLSs with a large Δ (2) Trinastic *et al.* argued in Ref [189] that TLSs with $|\Delta| > 0.1$ ev were removed because higher asymmetries correspond to defective states that do not exist in experimental glasses. This claim is difficult to substantiate as defective states with high Δ are not probed experimentally as they do not contribute to dissipation. Therefore, defective states could exist without being seen in acoustic measurements. Below 150 K, these two selection rules give dissipations similar to the Q^{-1} calculated on all the TLSs. As expected from the rapid cutoff imposed by $\mathrm{sech}(\Delta/2k_bT)$, the majority of dissipation comes from TLSs with small asymmetry and therefore this approximation is quite good. However, above 150 K, TLSs contributing significantly to the dissipation start to be removed.

6.2.3 Comparison with experiments

We will now compare the dissipation computed numerically with three experimental data sets. The first of these three experimental studies was performed by Fraser *et al.* [67] on General Electrics 105 fused quartz synthesized by melting a natural quartz crystal under vacuum . This silica sample has a high purity since it contains only 5 ppm of OH impurities. The dissipation measurements were carried out using the resonant sphere technique at 1.5 MHz. The second data set comes from Ref. [36] where dissipation was measured using the vibrating reed technique at 11.4 kHz on Suprasil W, which is also a very pure synthetic glass with a low concentration of impurities such as OH-. The last data set is taken from Ref. [123] where dissipation was measured using vibrating cantilevers excited electro-statically. The cantilever was coated with a 1 μm thin film of silica using Ion Beam Sputtering (IBS) at 100 K. It is important to notice that unlike the previous two studies focused on bulk vitreous silica, this last study uses deposited thin films known to be more prone to structural defects, less relaxed and sometimes porous [70]. Therefore, in contrast with vitreous silica, we will refer to this type of disordered SiO_2 as IBS silica.

These three data sets are represented in Fig. 6.14 along with the present numerical dissipation. We have to remind the reader that these dissipation curves were obtained at different frequencies, however, since the shape and magnitude of dissipation varies slowly with frequency we consider that they are consistent. The experimental data tell two different stories: (1) Dissipation for vitreous silica is represented by the red and green lines (data of Refs. [67, 36]). This first data set in red shows a maximum of dissipation between 30 and 50 K before a drop. The second data set

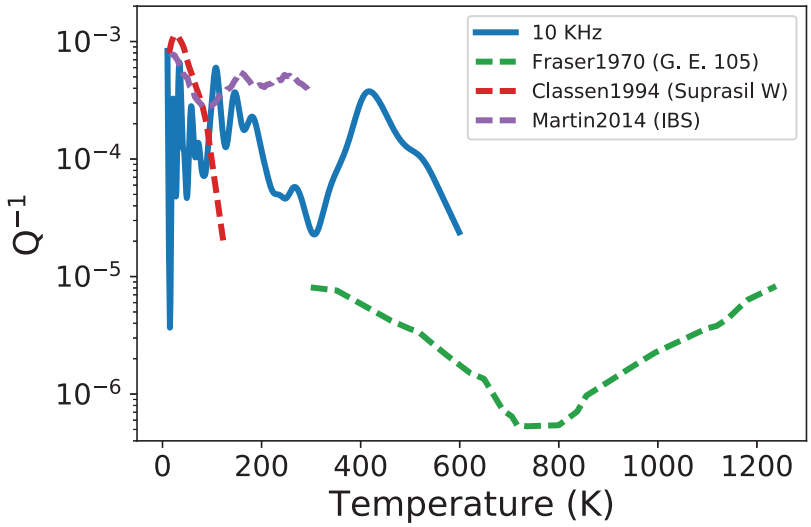

Figure 6.14: Q^{-1} at 10 kHz as a function of temperature for the present numerical data compared to the experimental measurements of Refs. [67, 36, 123].

(in green) shows that this drop reaches several orders of magnitude with a minimum of 10^{-6} at 750 K. After this minimum, dissipation increases again. This increase has been shown to come from impurities in the glass and losses taking place in the experimental setup [67] (2) For IBS silica (purple line), a maximum is also observed at low temperature, followed by a drop to 3.10^{-4}, not as marked as for vitreous silica. Two small peaks at 150 and 250 K follow. As of today, the difference in dissipative behavior above 50 K between vitreous and IBS silica is understood as the presence of additional TLSs due to the defects and structural heterogeneities present in IBS silica and absent in the almost perfect atomic arrangement of vitreous silica [123].
Due to the lack of criteria for structural relaxation, it is problematic to choose if the dissipation computed on the present numerical glasses should be compared to vitreous silica, IBS silica or if numerical glasses present features not seen in either of these experimental glasses. In addition, due to the discrete nature of the curve coming from the finite size of the samples, the precise analysis of temperature dependent features is difficult. However, three main regions of high dissipation can be distinguished. A first series of peaks from 10 to 100 K matches the dissipation peak at low temperature of both vitreous and IBS silica. Follows a second series of peaks from 100 to 200 K that approximatively matches the first peak seen in IBS silica. A third maximum from 350 to 500 K does not match any experimental data (the measurements on IBS silica stopping at 300 K). To better understand the origin of these three peaks, we plotted in Fig. 6.15 the distribution of asymmetries as a function of the energy barriers where the size of the points representing TLSs is a function of the maximum of dissipation produced by each TLSs (more precisely the size of the points is related to dissipation as $A = 2\log(\max(Q^{-1}))$) while the

colors of the points represent the temperature at which the dissipation for each TLS is maximum. This figure shows that the TLS responsible for dissipation are as expected TLSs whose Δ is small. Looking at their distribution with V we observe two groups: a first one from 0 to 0.5 eV which is responsible for the series of dissipation peaks seen from 10 to 300 K and a second one from 0.5 to 0.9 eV responsible for the dissipation peak at 450 K. The gap in-between these peaks originates from the absence of TLS around 0.5 eV coming from the limited number of barriers obtained in the present study. More samples would be necessary to fill this gap. From the global shape of the dissipation curve, the present glasses seem closer to IBS silica (less relaxed) both in amplitude and shape than to vitreous silica (more relaxed), which is expected given the very fast numerical quench rate. The origin of the discrepancy between the shape of the present dissipation and experimental values is difficult to pinpoint. However, as the number of TLSs obtained by our MD method is not sufficient to obtain a smooth dissipation curve, it is not surprising that detailed features could not be reproduced. One could hope that a more statistically significant set of TLSs could result a better agreement with experimental measurements. Another possible explanation could reside in the description of the glass. We should keep in mind that we are using a very simple interatomic potential, which may represent improperly the PEL. Therefore, it is possible that our set of TLS is a bad representation of the TLSs present in an experimental glass. The origin of this misrepresentation could come firstly from our sample, which, despite reproducing properly the properties of silica glasses, could reproduce improperly the TLSs present in experimental glasses. As showed by Fraser *et al.* in Ref. [67] and by the increase in TLS density with increasing quench rate (see Sec. 6.2.1), impurities have a strong impact on the dissipative properties of the glass. Therefore, subtle structural differences between numerical and experimental glasses could have a great impact on the existence and distribution of TLSs and thus on dissipation. Secondly, the present protocol used to search for TLSs could be blind to some of the TLSs or be biased toward certain TLSs. However, since the search method is based on MD kinetics, this claim is hard to support.

6.3 The case of Ta_2O_5

6.3.1 Thermally Activated Relaxations in Ta_2O_5

From the 59 Ta_2O_5 samples quenched at 10^{12} K/s, 1887 TLSs were obtained using the MD method. This corresponds to a density of 10.7 TLS/1000 atoms, slightly higher than the density obtained for the same quenching rate in SiO_2. The correlated distributions of asymmetry and energy barrier for Ta_2O_5 are represented in Fig. 6.16 and present V ranging from 0 to 1.2 eV with a high density of TLSs along the $\Delta = 2V$ line. The range of V is similar to what was obtained for SiO_2 as the searches were performed at the same temperature, $T = 1000$ K.

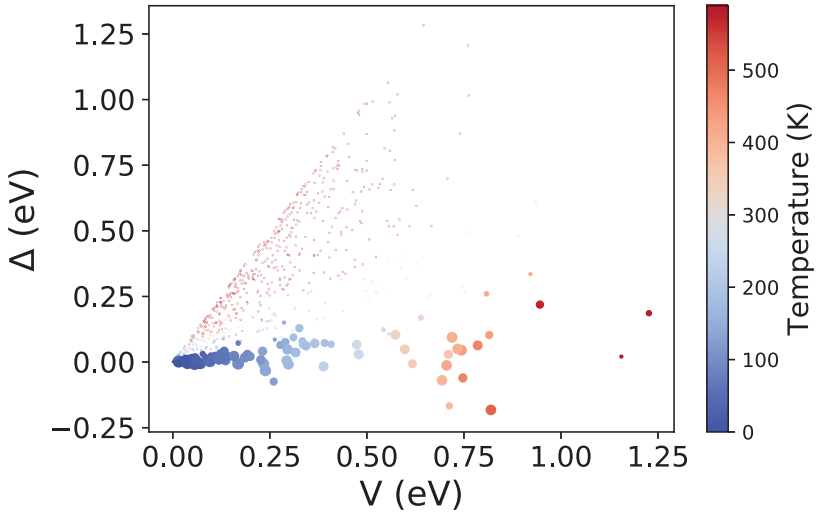

Figure 6.15: Asymmetries Δ as a function of the TLSs energy barriers V where the size of the points is a direct function of the dissipation generated by the TLSs (see text for details) and where the color of the points represents the temperature at which the dissipation for each TLS is maximum.

The longitudinal sensitivity to the strain, γ_l^2, represented in Fig. 6.17, shows a similar picture than in the case of SiO_2 with a tail of low γ_l^2 at low V leading to a cluster of points at higher γ_l^2 centered on the average at 83.0 eV^2. In Fig. 6.18 is plotted the attempt frequency, ω_1, which, as for SiO_2, do not vary with V and is gathered around a median value of 1 THz. This median value is almost an order of magnitude smaller than in SiO_2 which indicates a softer PEL. Part of this frequency difference can be explained by the fact that Ta atoms are heavier than Si atoms and therefore vibrate at lower frequencies.

As for SiO_2, it is possible to gather the TLSs around stereotypical relaxation motions corresponding to similar topologies. Since the TLSs observed in Ta_2O_5 present similarities with the atomic motions seen in SiO_2, we will use the same denomination when possible.

(1) As represented in Fig. 6.19, there exist in Ta_2O_5 TLSs similar to the Type I seen in SiO_2. In Ta_2O_5, Type 1 consists of a five- or six-folded Ta atom changing one or two of its O neighbors in a motion that can be described as a change of tetrahedron. As in SiO_2, the Ta atom goes through one of the faces of the polyhedron, with an energy maximum when the atom is located in the plane shared by the two polyhedra. However, since the SRO of the Ta atoms is more heterogeneous than Si atoms in SiO_2 (which can be seen by the sharpness of the first peak in the pair distribution functions shown in Chap. 4), Type I TLSs in Ta_2O_5 are not based nor create coordination defects and therefore may exist in experimental glasses and be probed when measuring dissipation. As in SiO_2, Type I TLSs are localized as they only involve two polyhedra and the moving Ta atom.

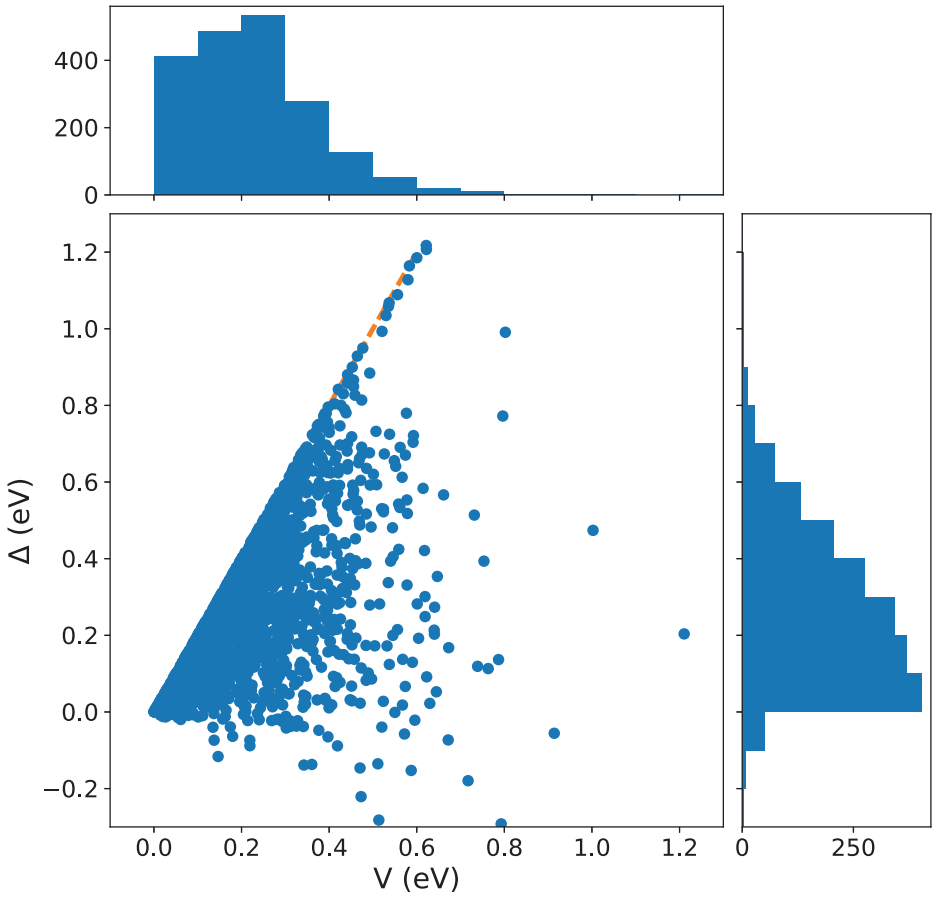

Figure 6.16: TLS asymmetry Δ as a function of V for the TLSs found in Ta_2O_5. The orange dashed line represents the maximum possible asymmetry $\Delta = 2V$ for a TLS of energy barrier V.

Their asymmetries are small with a maximum observed at 0.09 eV; however their energy barriers are more spread with values observed from 0.19 to 0.57 eV.

(2) The second type of TLS observed in Ta_2O_5 is noted Type II with an example represented in Fig. 6.20. We saw in SiO_2 that the collective motion of several oxygens could occur, with little energy increase. Similarly, the present glass presents relaxations based on the motion of several oxygens. However, while in SiO_2 every O is two-folded, and thus have a soft direction along which the Si-O-Si bond can bend, in Ta_2O_5, the O atom can be both two- or three-folded. Therefore when an O atom moves, it necessarily pushes another O atom that in turn pushes another O atom, and so on. The motion corresponds to the "sliding" of a chain of Os, each O changing one or two of its Ta neighbors. These Type II TLSs also result in a change of coordination for Ta as at the two ends of the chains, oxygen atoms will either leave a gap or be in excess. As Ta can be five or six folded, this does not create a coordination defects and the energy cost is small. As in SiO_2, these events present low asymmetries ranging from 0 to 0.1 eV but because of the transient breaking

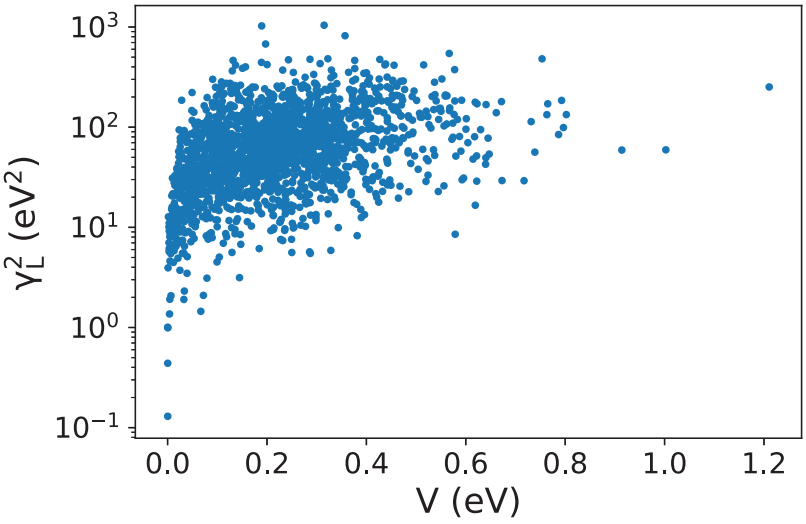

Figure 6.17: Longitudinal sensibility to the strain, γ_l, calculated from Eq. C.23 as a function of V for the TLSs found in Ta_2O_5. γ_t present a similar picture and will not be plotted here.

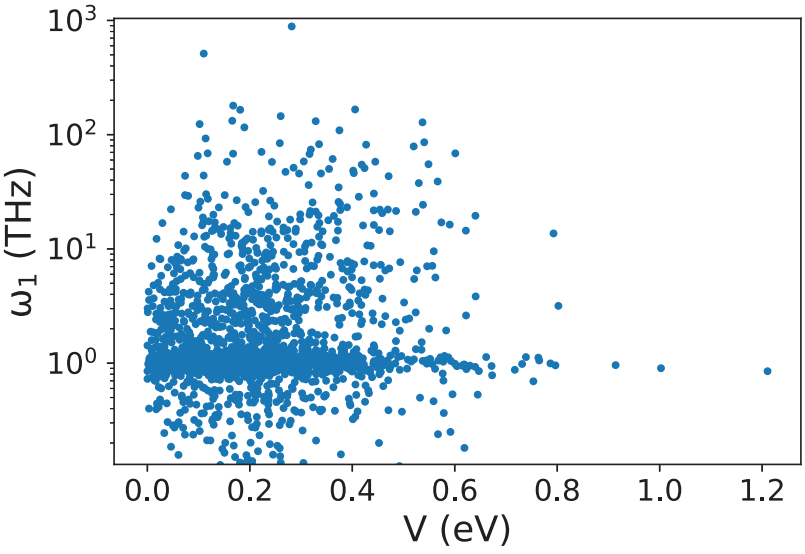

Figure 6.18: Attempt frequency ω_1 as a function of V for the TLSs found in Ta_2O_5. ω_2 present a similar picture and will not be plotted here.

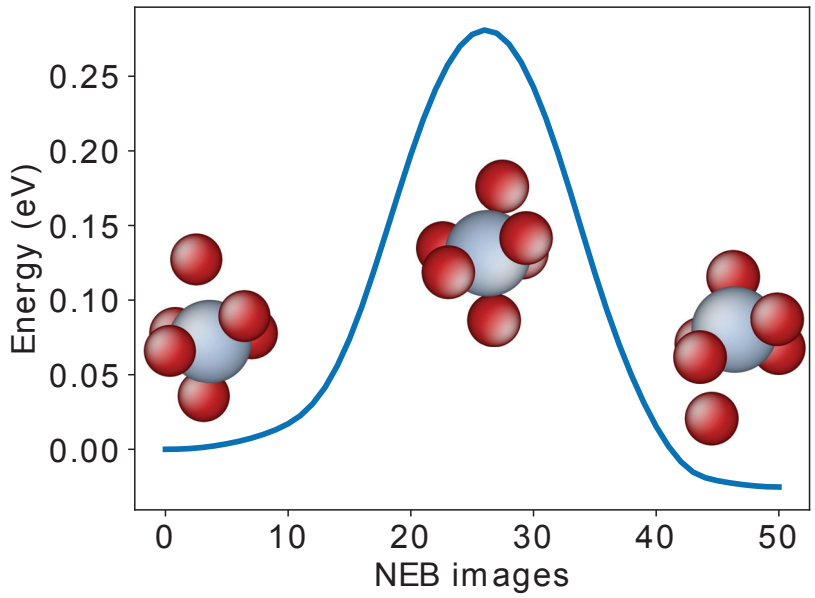

Figure 6.19: Potential energy along the minimum energy pathway for a TLS of type I in Ta_2O_5. The three snapshots show from left to right: the initial configuration, the saddle point and the final configuration of the TLS.

of Ta-O bonds and the higher variety of local environment, Type II TLSs possess higher energy barriers, from 0.1 to 0.45 eV (that is, of the same order as Type I).

(3) We will call Type III all TLSs based on the small motion of a single Ta or O atom that accounts for around ≈ 50 % of all the TLSs observed in Ta_2O_5. Due to the strong disorder present at the SRO level in Ta_2O_5, the PEL presents meta-basins in which several close ISs exist. The barriers between these ISs are small (<0.1 eV), therefore, the direction of these events in the PEL can be seen as "soft". From an atomic point of view, Type III TLSs can be either centered on Ta or O atoms; if centered on a Ta atom, the TLS corresponds to a local change of the Ta atom in its O polyhedra. In most polyhedra, there exists a bistable position of the Ta atom which is rarely at the center of the cage (as seen in the crystalline form of Ta_2O_5 in Fig.8 of Ref. [83]). In the second case, when the TLS is centered on an O atom, the motion consists of an O atom oscillating between positions in which it is two- and three-folded. As structural defects are naturally present in Ta_2O_5, it is possible for O atoms to go from being two-folded to being three-folded without a noticeable change in energy. Either centered on a Ta or an O atom, Type III TLSs are highly localized and involve less than 10 atoms. As these TLS have low energy barriers (<0.1 eV), they are not expected to contribute strongly to the dissipation as they will resonate at high-frequencies that are not of interest for GW detectors.

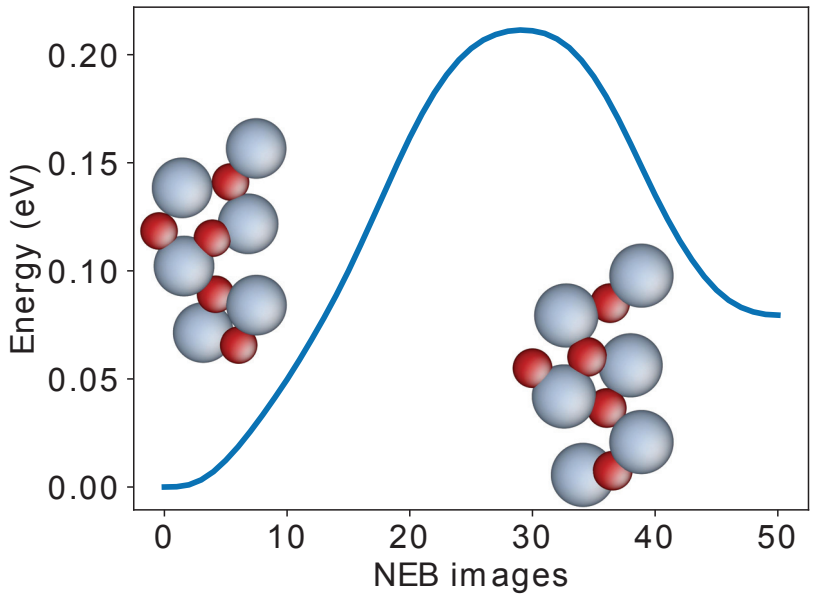

Figure 6.20: Potential energy along the minimum energy pathway for a TLS of type II in Ta_2O_5. The left and right snapshot represent the initial and final states respectively.

6.3.2 Comparison with experiments

As for SiO_2, dissipation is computed as a function of temperature using Eq. 6.1. We will compare the present dissipation with experimental data published by Martin *et al.* [122]. This data set was measured at 1 kHz on a vibrating cantilever coated with amorphous Ta_2O_5 which was itself deposited using Ion Beam Sputtering (IBS). It is important to note that as of today, no bulk vitreous Ta_2O_5 has ever been produced, therefore no experimental data is available.

As seen from Fig. 6.21, the dissipation curve obtained numerically still presents discrete peaks that are however less marked than in SiO_2 due to the higher TLS density. The dissipation curve presents values of the order of 10^{-4} to 10^{-3} in agreement with experimental dissipation. The numerical dissipation reproduces the initial decay up to about 150 K. Then while the experimental dissipation continues to decrease regularly, the numerical dissipation shows a broad peak at about 200 K. As for SiO_2, it is difficult to pin-point exactly the origin of this discrepancy and the main culprits are: a possible bad description of the numerical glass due to an inadequate potential or a non statistically significant probing of the TLS due to the research method or the finite size of the samples. Additional limits of the TLS model will be discussed in the next chapter.

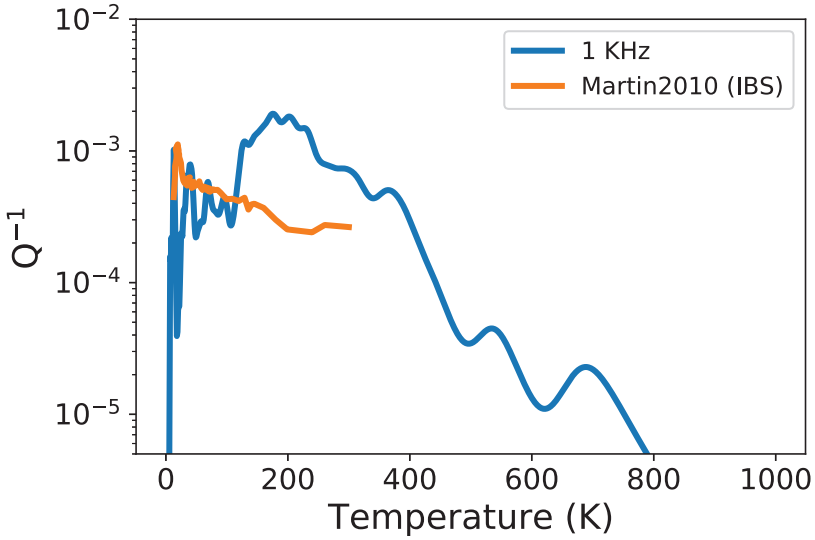

Figure 6.21: Q^{-1} at 10 kHz as a function of temperature for the present numerical data in blue compared to the experimental measurements of Ref. [122] in orange.

6.4 Summary

In the present chapter, we presented a numerical study of the mechanisms at the origin of dissipation at low-frequency. Using a search technique based on MD, we obtained sets of thermally-activated events in SiO_2 and Ta_2O_5 glasses. Each of these events was characterized by four parameters: the energy barrier, V, the asymmetry, Δ, the sensibility to the strain,γ, and the attempt frequency in the initial and final state $\omega_{1/2}$. Inspecting the atomic motions of some of these TLSs, we were able to group the events based on stereotypical atomic motions linked to similar topologies. In the case of SiO_2, we noticed that one of these groups existed due to coordination defects that do not exist a priori in experimental silica. In the case of Ta_2O_5, the more heterogeneous disorder is at the origin of a higher diversity of TLSs that can still be classified in categories presenting similar relaxation motions.

In a second time, we used these sets of TLSs and their corresponding four parameters in the framework of a revised TLS model that accounts for the difference in attempt frequency between the initial and final states and for the tensorial nature of the sensitivity parameter to the strain. We compared approximations reported in the literature to our calculations, and showed that the approximations are robust in the low temperature limit. Comparing the dissipation obtained numerically in SiO_2 and Ta_2O_5 with experimental data, we found that the present TLS model reproduces the amplitude of the dissipation in the temperature range of interest. However, the precise features of the experimental curves are not reproduced, which could be due either to a bad description of the glasses or to the limited size of the present TLS distributions.

CHAPTER 7

CONCLUSION

Energy dissipation in glasses may appear elusive due to the numerous phenomena at its origin in the different temperature and frequency ranges. In addition, the variety of behaviors displayed by different glasses requires a systematic look at the short- and medium-range order of each glass to grasp the origin of dissipation. As experimental methods show weaknesses when dealing with disordered solids, numerical tools are as of today, the most effective way to explore the atomic-scale phenomena at their core. In the present study, we made an attempt at using molecular dynamics in a two-fold manner: first, to simulate atomic models of two oxide glasses, Ta_2O_5 and SiO_2, and second to implement protocols measuring dissipation. The atomic nature of the simulations allows us to establish a link between dissipation and the short- and medium-range order of the glasses.

In the first part of the present study, we described the structure of Ta_2O_5 and TiO_2 doped Ta_2O_5 at the short- and medium-range order, by exposing the chain-like structure formed by Ti and Ta centered polyhedra. Performing a normal mode analysis, we proposed a new interpretation of the Raman spectra of Ta_2O_5 glasses. These results are important as they substantiate and bring a complementary analysis to the experimental studies, performed in parallel, on the structural and dissipative properties of Ta_2O_5 glasses [19, 172]. However, while at the time of the beginning of the present study, TiO_2 doped Ta_2O_5 glasses were in the pole position to be used in the next generation of gravitational waves (GWs) detectors, as of today, the decrease of dissipation induced by TiO_2 doping is deemed insufficient, especially since cryogenic operating temperatures are considered for the next generation of GWs detectors at which both SiO_2 and Ta_2O_5 present a peak of dissipation. Other materials such as amorphous silicon [175], single-crystal gallium phosphide [136] or single-crystalline silicon [166] would be better adapted to low temperatures.

The second part of the present study was dedicated to using the previously obtained Ta_2O_5 and SiO_2 glass models to study numerically energy dissipation.

At high-frequency, dissipation was computed through the implementation of numerical mechanical spectroscopy. To support the numerical study, an analytical development based on the projection of atomic motions on the vibrational eigenvectors was performed. We proved that dissipation is harmonic in the THz regime, and that it can be expressed analytically if the atomic positions and inter-atomic interactions are known. These equations revealed the role of non-affine motions in dissipation, which, in the case of hydrostatic deformation, can be shown to be based on a local symmetry factor. The analytical and numerical study we performed at high frequency are of significant importance for the study of attenuation and energy dissipation in solids. First because prior to this work, no analytical formula had been proposed to describe the dissipative behavior of a disordered harmonic solid. Secondly, because experimental studies measure attenuation and thus dissipation values only until the Ioffe-Regel criteria, while our numerical study and analytical development propose an approached to understand dissipation beyond this limit. However, as our analytical development is based on the knowledge of atomic positions and inter-atomic interactions, it is hard to imagine a simple way of extending the present formula to directly help the analysis of experimental attenuation data. One possibility would be to find a analytical link between the Q^{-1} proposed in the present study and the dynamical structure factor probed experimentally using Brillouin scattering and IXS. In addition to proposing a correcting factor for experimental data, such a development would make clearer the link between energy dissipation Q^{-1} and attenuation Γ, that is as of today hard to understand outside simple models such as damped harmonic oscillators.

A second follow-up to the present high-frequency study would be to implement less memory costly diagonalization techniques. Indeed, the diagonalization algorithm used in the present study is memory intensive and as a consequence the dissipation curves displayed in Chap. 5 present artifacts due to the small size of the samples. The use of less computer intensive diagonalization techniques would allow to study larger samples possessing more vibrational eigenmodes and thus, would allow a smaller Langevin thermostat parameter leading to less numerical artifacts.

A third follow-up imposes itself as the present analytic expression of the quality factor and application of Ξ as structural indicator of dissipation go beyond the case of oxide glasses. More work could be done in other disordered solids such as metallic glasses or amorphous silicon, but also in crystals, where defects that break the local symmetry, such as dislocation cores or grain boundaries, will be sources of harmonic dissipation. Likewise, we expect that non-centrosymmetrical crystals, such as quartz, should exhibit high-frequency dissipation, even in absence of defects, although these aspects of energy dissipation at high frequencies remain to be explored quantitatively.

The second part of the study on dissipation focused on low-frequencies. In order to grasp the atomic origin of dissipation at low-frequency, we performed searches for thermally activated bistable states known as Two-Level Systems (TLS) and were able to catalog these atomic motions based on their topology. The present low-frequency study is of prime importance as it presents thermally activated atomic motions that are often theorized but rarely observed and described. In addition, we propose for the first time a classification of these events, made possible by the order within disorder present at short- and medium-range order in oxide glasses. A revised TLS model accounting for the full tensorial nature of the sensitivity to the strain and the difference in attempt frequencies between the initial and final states of the TLSs was proposed. Based on this new framework and using the TLSs previously obtained, different assumptions used in the literature when fitting the TLS model to experimental data were tested and shown to be robust, especially in the low temperature limit. In a second time, we compared the dissipation obtained numerically with experimental measurements obtained on vitreous silica and silica and Ta_2O_5 deposited using Ion Beam Sputtering. Doing so, we showed for the first time that no approximations are needed for the TLS model to reproduce the amplitude of the dissipation of experimental glasses. However, we couldn't reproduce the detailed features of the experimental dissipation curve, because of what we think are the shortcomings of the present inter-atomic potentials and because of the limited size of our TLS distributions. An error in the TLS distribution could either come from a biased exploration of the TLSs present in the numerical glass or from a bad description of the glass itself. The first hypothesis could be tested by developing a new algorithm for the search of TLSs while the latter could be verified comparing TLS density in numerical silica described using different inter-atomic potentials.

Finally, working with the TLS model made us realize its shortcomings and we think that two additional points should be addressed in the future.

(1) In the TLS model, the events are said to be independent (as seen from the superposition principle of Eq. C.21) which may be false for two reasons. As most of the TLSs are based on the motion of tens or hundreds of atoms, it is not uncommon for two TLSs to share atoms, especially if, as believed from experimental glasses, TLS are centered on defects such as OH impurities. Therefore, the activation of a TLS could affect the possible activation of other TLSs sharing the same atoms, either by preventing or helping the relaxation. The second reason is that, as shown in Refs. [148, 103, 104], shear transformation zones and TLSs in glasses produce long range strain fields. When an acoustic wave passes through a medium, the strain field produced by the activation of some of the TLSs would be added to the deformation induced by the acoustic wave. This additional deformation may induce other activations leading to two different type of transitions: spontaneous transitions due to thermal fluctuation and "provoked" transitions due to the strain field produced by spontaneous transitions. Measuring the importance of this

phenomena would require to characterize the deformation fields around transforming TLSs and study closely the interaction between these fields and other TLSs through their sensitivity to the strain.

(2) When starting the present study, we tried to computed the deformation potential, γ, by imposing stress or strain to the simulation cell and measuring the resulting change in energy of the initial and final states of each TLSs. Doing so, we observed that many TLSs disappear when the solid is under stress or strain due to the vanishing of their energy barriers. This vanishing happened in two different circumstances: when the potential energy of the initial or final state of the TLS goes above the barrier height or when the energy of the barrier itself decreases under deformation until the PEL becomes monotomic in the direction of the TLS. In both cases the TLS effectively disappears and thus does not contribute to dissipation. This fact indicates that dissipation could depend on the amplitude of the acoustic wave considered as TLSs would vanish at different deformation amplitude. Therefore, a new TLS model needs to be a function of the wave amplitude as it needs to take into account the deformation at which each TLS vanishes.

A final point calls for additional work despite not being considered directly in the present manuscript. Between TLSs, source of dissipation below the MHz, and harmonic dissipation, source of dissipation above the GHz, there is a frequency range where most of the dissipation is believed to come from Akhiezer damping as explained in Chap. 2. This specific frequency range is not directly accessible using MD as the time scale involved is two to three orders of magnitude larger than what MD is capable of. Since dissipation cannot be measured directly, a model need to be used to predict dissipation as we did at low frequencies with the TLS model. As of today, Akhiezer's dissipation is modeled from calculations of the Grüneisen parameters, that represent the variation of frequency of the eigenmodes with respect to the deformation induced by the passing wave [90]. This work which would require the diagonalization of the dynamical matrices of very large atomic samples would be very interesting as it would allow to fill the gap between the present studies performed below the MHz and above the THz.

APPENDIX A

Analytic Expression of the Complex Modulus in the Harmonic Approximation

We detail here the calculations leading to an analytic expression of the dissipation in the harmonic linear response regime, assuming a Langevin thermostat. We consider here only the case of isostatic deformations. The general expressions given in the main text are obtained by a straightforward generalization of these calculations.

A.1 Frequency-dependent pressure

We note r_i^α the current position of atom i in direction α and R_i^α, its equilibrium position in the reference undeformed cell. At time t, the cell is compressed or stretched isostatically along the X, Y and Z directions by $\epsilon(t) = \epsilon_0 \sin(\omega t)$, such that:

$$r_i^\alpha = (1+\epsilon) R_i^\alpha + x_i^\alpha, \tag{A.1}$$

where x_i^α is the non-affine displacement. In the harmonic approximation, using the expression of the energy given in Eq. 5.6 of the main text, the force on atom i and direction α is given by:

$$F_i^\alpha = -\sum_{j\beta} D_{ij}^{\alpha\beta} (r_{ij}^\beta - R_{ij}^\beta) \tag{A.2}$$

where R_{ij}^{α} is the equilibrium separation between atoms i and j in direction α in the undeformed initial cell. The dynamical matrix, $D_{ij}^{\alpha\beta}$, is sparse and has the following usual symmetries

$$D_{ij}^{\alpha\beta} = D_{ji}^{\beta\alpha} = D_{ji}^{\alpha\beta} = D_{ij}^{\beta\alpha}. \tag{A.3}$$

And in free mechanical systems, the acoustic sum rule imposes

$$\sum_i D_{ij}^{\alpha\beta} = 0, \tag{A.4}$$

that expresses the translational invariance.

The pressure is expressed as:

$$\begin{aligned} P &= \frac{1}{3V} \sum_{i\alpha j\beta} F_i^{\alpha} r_{ij}^{\alpha} \\ &= \frac{1}{3V} \sum_{i\alpha j\beta} D_{ij}^{\alpha\beta} (r_{ij}^{\beta} - R_{ij}^{\beta}) r_{ij}^{\alpha}, \end{aligned} \tag{A.5}$$

where $V = L^3$ is the current volume of the cell, with $L = L_0(1+\epsilon)$. At the rather low temperatures considered here, we have checked that the kinetic pressure is negligible and will not be included in the calculations.

The pressure can be re-written as a function of the applied strain ϵ and the non-affine displacements x_i^{α} using Eq. A.1:

$$\begin{aligned} P &= \frac{1}{3V} \sum_{i\alpha j\beta} D_{ij}^{\alpha\beta} \left[\epsilon R_{ij}^{\beta} + x_{ij}^{\beta} \right] \left[(1+\epsilon) R_{ij}^{\alpha} + x_{ij}^{\alpha} \right] \\ &= \frac{\epsilon(1+\epsilon)}{3V} \sum_{i\alpha j\beta} D_{ij}^{\alpha\beta} R_{ij}^{\beta} R_{ij}^{\alpha} + \frac{1}{3V} \sum_{i\alpha j\beta} D_{ij}^{\alpha\beta} x_{ij}^{\beta} x_{ij}^{\alpha} + \frac{(1+2\epsilon)}{3V} \sum_{i\alpha j\beta} D_{ij}^{\alpha\beta} R_{ij}^{\alpha} x_{ij}^{\beta} \end{aligned} \tag{A.6}$$

In the linear response regime, only the first-order terms in ϵ and x_{ij}^{β} are kept. The second term of the above expression is therefore neglected and the current volume V is replaced by the reference volume V_0. The first term corresponds to the pressure in case of affine atomic motion, with the affine bulk modulus:

$$\begin{aligned} K^{\infty} &= -V \frac{dP}{dV} = -\frac{1}{3} \frac{dP}{d\epsilon} \\ &= -\frac{1}{9V_0} \sum_{i\alpha j\beta} D_{ij}^{\alpha\beta} R_{ij}^{\beta} R_{ij}^{\alpha}. \end{aligned} \tag{A.7}$$

The last term of Eq. A.6 is the non-affine contribution, which can be re-arranged using the

symmetries of D:

$$\sum_{i\alpha j\beta} D_{ij}^{\alpha\beta} R_{ij}^{\alpha} x_{ij}^{\beta} = \sum_{i\alpha j\beta} D_{ij}^{\alpha\beta} R_{ij}^{\alpha} x_{j}^{\beta} - \sum_{i\alpha j\beta} D_{ij}^{\alpha\beta} R_{ij}^{\alpha} x_{i}^{\beta} = 2 \sum_{i\alpha j\beta} D_{ij}^{\alpha\beta} R_{ij}^{\alpha} x_{j}^{\beta}. \tag{A.8}$$

The pressure is thus expressed as:

$$P = -3K^{\infty}\epsilon + \frac{2}{3V_0} \sum_{i\alpha j\beta} D_{ij}^{\alpha\beta} R_{ij}^{\alpha} x_{j}^{\beta}. \tag{A.9}$$

We then project the non-affine displacements onto the normal modes of the system. To this end, we introduce mass-scaled displacements

$$s_j^{\beta} = \sqrt{m_j} x_j^{\beta}, \tag{A.10}$$

and their projections s_m on the eigenmodes $e(m)$ of the system (i.e. the eigenvectors of the mass-scaled dynamical matrix $\tilde{D}$):

$$s_m = \sum_{j\beta} s_j^{\beta} e_j^{\beta}(m) \tag{A.11}$$

$$s_j^{\beta} = \sum_{m} s_m e_j^{\beta}(m). \tag{A.12}$$

Replacing x_j^{β} in Eq. A.9, we form a mode-dependent term:

$$C_m = \sum_{i\alpha j\beta} D_{ij}^{\alpha\beta} R_{ij}^{\alpha} \frac{e_j^{\beta}(m)}{\sqrt{m_j}} \tag{A.13}$$

and the final expression of the pressure is:

$$P = -3K^{\infty}\epsilon + \frac{2}{3V_0} \sum_{m} C_m s_m. \tag{A.14}$$

Averaging this equation over multiple cycles and taking its Fourier transform, we obtain:

$$\langle P \rangle(\omega) = -3K^{\infty}\epsilon(\omega) + \frac{2}{3V_0} \sum_{m} C_m \langle s_m \rangle(\omega), \tag{A.15}$$

where $\epsilon(\omega)$ is the Fourier transform of $\epsilon(t)$ between 0 and $T = 2\pi/\omega$. We see that C_m is proportional to $\partial P/\partial s_m$ and therefore expresses the sensitivity of the pressure to the amplitude of the normal mode m. The properties of C_m will be further explored below.

A.2 Complex bulk modulus

To express $\langle s_m \rangle(\omega)$, we start from the SSLOD equations written as a second-order differential equation in Sec 3.1.3:

$$m_i \ddot{r}_i^\alpha = m_i r_i^\alpha (\dot{\epsilon}^2 + \ddot{\epsilon}) - \sum_{j\beta} D_{ij}^{\alpha\beta} (r_{ij}^\beta - R_{ij}^\beta) - m_i \gamma (\dot{r}_i^\alpha - r_i^\alpha \dot{\epsilon}) + F_{th}, \tag{A.16}$$

which is written in terms of non-affine displacements, keeping only the first-order terms, as:

$$m_i \ddot{x}_i^\alpha = -(\sum_{j\beta} D_{ij}^{\alpha\beta} R_{ij}^\beta)\epsilon - \sum_{j\beta} D_{ij}^{\alpha\beta} x_j^\beta - m_i \gamma \dot{x}_i^\alpha + F_{th}. \tag{A.17}$$

Introducing the mass-scaled coordinates s_i^α we obtain:

$$\ddot{s}_i^\alpha = -\Big(\sum_{j\beta} \frac{D_{ij}^{\alpha\beta}}{\sqrt{m_i}} R_{ij}^\beta\Big)\epsilon - \sum_{j\beta} \tilde{D}_{ij}^{\alpha\beta} s_j^\beta - \gamma \dot{s}_i^\alpha + \frac{F_{th}}{\sqrt{m_i}}, \tag{A.18}$$

which yields after projection on the eigenmodes:

$$\ddot{s}_m = C_m \epsilon - \omega_m^2 s_m - \gamma \dot{s}_m + F_m. \tag{A.19}$$

Here, F_m is the random force on mode m and ω_m^2 the eigenfrequency of mode m, i.e. the eigenvalue of $\tilde{D}$ corresponding to the eigenmode $e(m)$. We have also recognized that

$$\sum_{i\alpha j\beta} \frac{D_{ij}^{\alpha\beta}}{\sqrt{m_i}} R_{ij}^\beta e_i^\alpha(m) = -C_m, \tag{A.20}$$

in reference to Eq. 5.13, where the minus sign comes from the exchange between indices i and j. Averaging this equation over multiple cycles, the random force term, of zero mean, vanishes, and taking the Fourier transform, we obtain:

$$\langle s_m \rangle(\omega) = \frac{C_m}{\omega_m^2 - \omega^2 + i\gamma\omega} \epsilon(\omega). \tag{A.21}$$

Finally, replacing $\langle s_m \rangle(\omega)$ in Eq. A.15, we have:

$$\langle P \rangle(\omega) = -3K^\infty \epsilon(\omega) + \frac{2}{3V_0} \sum_m \frac{C_m^2}{\omega_m^2 - \omega^2 + i\gamma\omega} \epsilon(\omega), \tag{A.22}$$

resulting in the complex bulk modulus reported in the main text:

$$K(\omega) = K^\infty - \frac{2}{9V_0} \sum_m \frac{C_m^2}{\omega_m^2 - \omega^2 + i\gamma\omega}. \tag{A.23}$$

APPENDIX B

POTENTIAL ENERGY LANDSCAPE AROUND AN INHERENT STRUCTURE

When obtaining a list of TLSs, either through MD or using ART, it is hard not to wonder: how does all of these new stable configurations are organize around the initial IS ? Are they organized in cluster or randomly spread in the 3N dimensions of the PEL ? These questions have been repeatedly studied by the group of D. J. Wales, most of the time using disconnectivity graph on small clusters of atoms or organic compounds (see Ref. [200]). Since it would be very computationally intensive to draw the disconnectivity graph for systems as large as the ones used in the present study, we propose a simpler approach to visualize and develop an intuition of the organization of inherent structures in the PEL.

We chose one of the SiO_2 samples used in Chap. 6 and the 10 associated TLSs found using MD. Their corresponding minimum energy pathways computed with the NEB method are represented in Fig. B.1. The TLSs are numbered from 0 to 10 for convenience. Looking quickly at this graph, we see that most of these TLSs are quite asymmetric especially number 4 and 7. It seems that the TLS 1 has the lowest activation energy since it is squished on the x-axis, a zoom on this region reveals that it is a very unstable TLS whose Δ almost equals its activation energy.

We know compute the distance matrix M between the 11 IS (10 final configurations plus the initial state). The distance between two configurations k and l is calculated as:

$$M_{kl} = \sum_{i}^{N} \left\| R_i^k - R_i^l \right\| \tag{B.1}$$

Where N is the number of atoms in the system and R_i^k and R_i^l denote the equilibrium position of

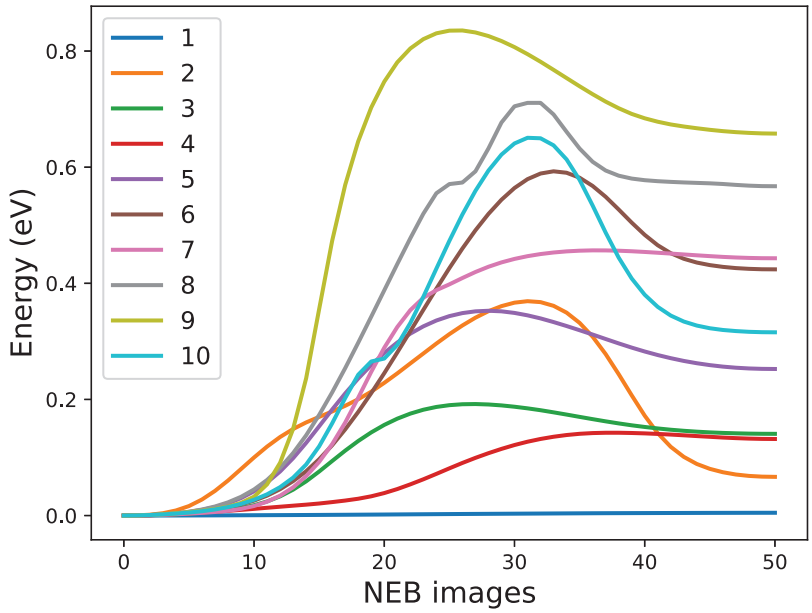

Figure B.1: Potential energy of the NEB images along the minimum energy pathway for 10 TLS found from the same starting IS.

atom i in the ISs k and l respectively. The resulting distance matrix is represented as a heat map in Fig. B.2. The black diagonal represents the distances for $k = l$ and are effectively zero. The largest distance is 151.9 Å between IS 4 and 10 and the smallest is 91.95 Å between IS 1 and the initial configuration. As 1 is close to the initial IS, it is therefore also close to all the other ISs.

To visualize the organization of these ISs in the PEL, it would be interesting to represents them in a 2D plane were they would be organized according to the distance matrix with the closest ISs in the PEL close on the 2D plane and the farthest ISs in the PEL far from each other on the 2D plane. Since there is no simple analytic solution to create graphs based on a distance matrix, we use once again a Verlet algorithm where the ISs are represented as points in a 2D space. The interactions between points are described by springs whose equilibrium distances are given by the distance matrix. To do so, the 11 ISs are placed randomly in space and at each time step, the forces between them are computed using the distance matrix as:

$$F_l = \sum_{k=0}^{10} K(r_{lk} - M_{lk}) \tag{B.2}$$

where K is the spring constant and r_{lk} is the distance between the points corresponding to the IS l and k in the 2D space. A fraction of the energy is withdrawn from the system at each time step until the particles organization reaches a stable state represented in Fig. B.3. It is important to notice that since the graph showed here is the result of a dynamic, it is not the only possible

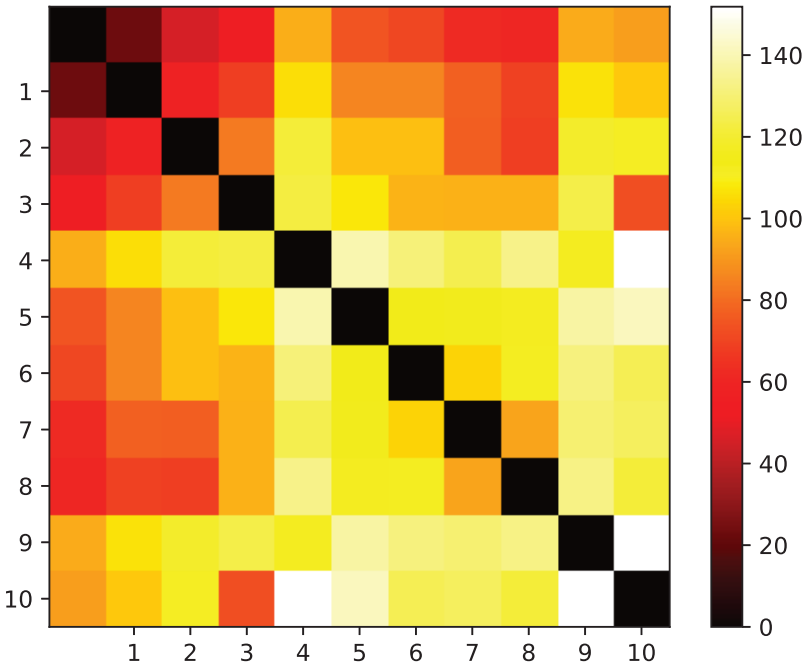

Figure B.2: Heat map of the distance matrix M for 11 IS found on the same SiO_2 glass. Colors represent the distances in angstrom between configuration, lighter colors representing configurations further from each other.

organization for the 11 ISs and their corresponding distance matrix (it would even be possible to explore the 22+1 dimensions of the PEL of this system but it would be going too far).

At first sight, the 11 ISs seem homogeneously spread in space around the initial IS marked in by a red point as IS 0. As expected from the heat map of the distance matrix represented in Fig. B.2, the IS 1 is almost on top of the initial IS (and therefore quite close to all the other ISs). We saw that the minimum energy pathway between these two states presents a small energy barrier, which is now explained by the fact that these states are also close in the PEL. IS 0 and 1 are likely to be two states belonging to the same meta-basin, one of them (IS 0) slightly more relaxed than the other. Looking at the atomic configurations, we identified this TLS as a Type II involving four oxygen atoms (see main text for details). Coming back to Fig. B.3, we see that IS 4 and 9 are far from all the other ISs, which is explained by the distance seen both of these states and the rest of the TLS in the PEL. These two ISs got isolated to minimize the energy of the system. The IS 10 is also far from most of the TLS but ends close to the IS 3 with which it has an affinity. Looking at the atomic configurations for IS 3 and 10, we observed that these two TLSs happen in the same region of the glass and involve some of the same atoms which explains their proximity in the PEL. A similar situation exists to a lesser extent between IS 2 and 8. In a general manner, in our 2D plot, two ISs that involve motions of the same atoms in the same

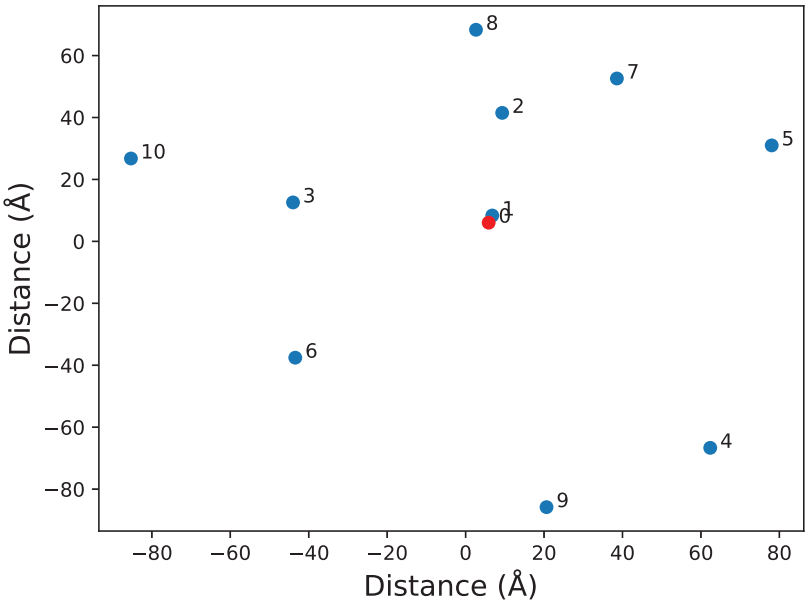

Figure B.3: 11 IS found on the same SiO_2 glass organized by proximity in a 2D space.

directions will form a line with the initial state.

APPENDIX C

ENERGY DISSIPATION IN THE FRAMEWORK OF THE TLS MODEL

In this appendix, we detail the theory leading to the expression of dissipation 6.1. We follow an approach similar to that of Jackle *et al.* [92], but fully account for the tensorial nature of the strains and stresses and for the possible difference between the attempt frequency in the first and second states of the TLSs.

C.1 Complex modulus

C.1.1 Equilibrium probabilities and detailed balance

We consider a TLS with 2 metastable states, noted 1 and 2, linked by a double-well potential, $V(x)$ as shown in Figs. 6.1 of the main text. We note p_1 and p_2, the probabilities to find the TLS in either state 1 or 2, which denotes the basin on one side and the other of the energy barrier, and $\bar{p}_1$ and $\bar{p}_2$, their equilibrium values.
At equilibrium, the probability to be at position x is proportional to $\exp(-V(x)/k_bT)$. Therefore,

$$\bar{p}_1 \propto \int_1 \exp\left(-\beta V(x)\right)\, \mathrm{d}x \tag{C.1}$$

and

$$\bar{p}_2 \propto \int_2 \exp\left(-\beta V(x)\right)\, \mathrm{d}x, \tag{C.2}$$

where the integrals are performed over the basins of both states and $\beta = 1/k_bT$. Using a harmonic approximation, with ω_1^2 and ω_2^2 the curvatures at the bottom of both states, we have:

$$\begin{aligned} \bar{p}_1 &= \frac{1}{1+\exp(-\beta\Delta)\frac{\omega_1}{\omega_2}} \\ \bar{p}_2 &= \frac{1}{1+\exp(\beta\Delta)\frac{\omega_2}{\omega_1}}, \end{aligned} \tag{C.3}$$

where Δ is the energy asymmetry between states 1 and 2, as in the main text.
According to the harmonic Transition State Theory [195], the transition rates between states 1 and 2 are:

$$\begin{aligned} a_{12} &= \frac{\omega_1}{2\pi}\exp(-\beta E^*) \\ a_{21} &= \frac{\omega_2}{2\pi}\exp(-\beta(E^*-\Delta)), \end{aligned} \tag{C.4}$$

where $E^\star$ is the energy barrier from state 1 to 2. One can easily check that Eqs. C.3 and C.4 satisfy the detailed balance, i.e. $\bar{p}_1 a_{12} = \bar{p}_2 a_{21}$.

C.1.2 Deformation potential

The TLS is in a volume $\mathcal{V}$ subjected to a periodic applied strain tensor, $\bar{\bar{\epsilon}}(t)$. Dissipation occurs if the energy asymmetry, Δ, depends on the applied strain. Within an eigenstrain approach [135], such coupling occurs if an eigenstrain $\bar{\bar{\epsilon}}^\star$ is generated when the TLS transforms from state 1 to state 2. The energy asymmetry and stress then depend on the applied strain as (with repeated index summation):

$$\begin{aligned} \Delta\left(\bar{\bar{\epsilon}}\right) &= \Delta + \frac{\mathcal{V}}{2} C^\infty_{ijkl}\left(\epsilon_{ij} - \frac{v_a}{\mathcal{V}}\epsilon^\star_{ij}\right)\left(\epsilon_{kl} - \frac{v_a}{\mathcal{V}}\epsilon^\star_{kl}\right) \\ \sigma_{ij} &= C^\infty_{ijkl}\left(\epsilon_{kl} - \frac{v_a}{\mathcal{V}}\epsilon^\star_{kl}\right), \end{aligned} \tag{C.5}$$

where C^∞ is the tensor of elastic constants (including both affine and non-affine contributions, which relax over timescales much shorter than considered here [42]) and v_a, the TLS volume. Introducing the deformation potential tensor:

$$\gamma_{ij} = \left.\frac{\partial\Delta}{\partial\epsilon_{ij}}\right|_{\bar{\bar{\epsilon}}=0} = -v_a C^\infty_{ijkl}\epsilon^\star_{kl}, \tag{C.6}$$

we have:

$$\sigma_{ij} = C^\infty_{ijkl}\epsilon_{kl} + \frac{\gamma_{ij}}{\mathcal{V}}. \tag{C.7}$$

If we introduce $\delta p_2(t) = p_2(t) - \bar{p}_2(0)$, the difference between the current probability of being in

state 2, $p_2(t)$, and its equilibrium value in absence of applied strain, $\bar{p}_2(0)$, the time-dependent part of the stress is expressed as:

$$\sigma_{ij} = C^{\infty}_{ijkl}\epsilon_{kl}(t) + \frac{\gamma_{ij}}{V}\delta p_2(t), \tag{C.8}$$

Concerning the energy asymmetry, keeping only the first-order time-dependent term, we have:

$$\Delta\left(\bar{\bar{\epsilon}}\right) = \Delta + \gamma_{ij}\epsilon_{ij}. \tag{C.9}$$

C.1.3 Master equation

Dissipation arises because the strain changes Δ (Eq. C.9), which in turn changes the equilibrium probabilities, $\bar{p}_1$ and $\bar{p}_2$ (Eq. C.3) and brings the system in and out-of-equilibrium state with a finite relaxation time. The probabilities p_1 and p_2 follow master equations:

$$\begin{aligned} \dot{p}_1 &= -p_1 a_{12} + p_2 a_{21} \\ \dot{p}_2 &= p_1 a_{12} - p_2 a_{21}, \end{aligned} \tag{C.10}$$

where the transition rates depend on time because of their dependence on Δ (Eq. C.4). Since $p_1 + p_2 = 1$, we have:

$$\dot{p}_2 = -p_2(a_{12} + a_{21}) + a_{12}. \tag{C.11}$$

We can thus define a time-dependent equilibrium, reached if the applied strain varies slowly compared to the relaxation time of the TLS:

$$\bar{p}_2(t) = \frac{a_{12}(t)}{a_{12}(t) + a_{21}(t)}, \tag{C.12}$$

Inserting Eq. C.12 into Eq. C.11, we obtain:

$$\dot{p}_2 = -(p_2 - \bar{p}_2(t))(a_{12}(t) + a_{21}(t)) \tag{C.13}$$

We see from this equation and Eq. C.4 that to the first order, the time-dependence of the transition rates can be neglected, allowing to define a relaxation time, $\tau^{-1} = a_{12}(0) + a_{21}(0)$. Using $V = E^{\star} - \Delta/2$ as in the main text, we can rewrite the relaxation time as:

$$\tau^{-1} = \frac{\sqrt{\omega_1\omega_2}}{\pi}\exp(-\beta V)\mathrm{ch}\left(\frac{\beta\Delta}{2} + \frac{1}{2}\ln\frac{\omega_2}{\omega_1}\right) \tag{C.14}$$

From Eq. C.13 using $\delta p_2 = p_2 - \bar{p}_2(0)$, we have:

$$\tau\dot{\delta} p_2 = -\delta p_2 + \bar{p}_2(t) - \bar{p}_2(0) \tag{C.15}$$

From the definition of the coupling parameter, we have:

$$\begin{aligned} \bar{p}_2(t) - \bar{p}_2(0) &= \bar{p}_2(\Delta + \gamma_{ij}\epsilon_{ij}(t)) - \bar{p}_2(\Delta) \\ &\simeq \frac{\partial \bar{p}_2}{\partial \Delta}\gamma_{ij}\epsilon_{ij}(t) \end{aligned} \tag{C.16}$$

and from Eq. C.3:

$$\frac{\partial \bar{p}_2}{\partial \Delta} = -\frac{1}{4kT\mathrm{ch}^2\left(\frac{\beta\Delta}{2} + \frac{1}{2}\ln\frac{\omega_2}{\omega_1}\right)} \equiv -A. \tag{C.17}$$

Finally, inserting Eq. C.16 with the definition of A into Eq. C.15, we obtain the following first-order differential equation for δp_2:

$$\tau\dot{\delta} p_2 = -\delta p_2 - A\gamma_{ij}\epsilon_{ij}, \tag{C.18}$$

which is solved in the spectral domain, with $\epsilon \propto \exp(i\omega t)$:

$$\delta p_2 = -\frac{A}{1 + i\omega\tau}\gamma_{ij}\epsilon_{ij} \tag{C.19}$$

C.1.4 Complex modulus

From Eqs. C.8 and C.19, the tensor of complex elastic moduli is expressed as:

$$C(\omega) = C^{\infty} - \frac{1}{\mathcal{V}}\frac{A}{1 + i\omega\tau}\bar{\bar{\gamma}} \otimes \bar{\bar{\gamma}}, \tag{C.20}$$

with $\gamma \otimes \gamma$, the tensor of components $\gamma_{ij}\gamma_{kl}$. If the volume $\mathcal{V}$ contains a population of TLSs, with different $\bar{\bar{\gamma}}_\ell$, A_ℓ and τ_ℓ, we obtain from the superposition principle:

$$C(\omega) = C^{\infty} - \frac{1}{\mathcal{V}}\sum_{\ell, TLS}\frac{A_\ell}{1 + i\omega\tau_\ell}\bar{\bar{\gamma}}_\ell \otimes \bar{\bar{\gamma}}_\ell \tag{C.21}$$

C.2 Longitudinal dissipation

If the medium is deformed by a longitudinal wave along a unit vector $\vec{U}$, the corresponding strain tensor is $\epsilon(t)\vec{U} \otimes \vec{U}$, with elements $\epsilon(t)U_iU_j$. Dissipation is then given by the time delay between

$\epsilon(t)$ and the tensile stress $\sigma = U_i \sigma_{ij} U_j$ along $\vec{U}$.

Glasses being isotropic, the static term in Eq. C.21 corresponding to C^∞ yields $\sigma = M\epsilon$, where $M = \lambda + 2\mu$ is the longitudinal modulus and λ and μ are the Lamé coefficients. The second term in Eq. C.21 yields for each TLS a coupling term of the form $\sum_{ijkl} \gamma_{ij}\gamma_{kl} U_i U_j U_k U_l = (\sum_{ij} \gamma_{ij} U_i U_j)^2$. Since a TLS can take any orientation with respect to the applied strain, we have to average this term over all strain directions:

$$\langle \gamma^2 \rangle_L = \sum_{ijkl} \gamma_{ij}\gamma_{kl} \langle U_i U_j U_k U_l \rangle. \tag{C.22}$$

Only even-power averages are non-zero and because of isotropy, there are only 2 distinct terms, $\langle U_X^4 \rangle = \langle U_Y^4 \rangle = \langle U_Z^4 \rangle = 1/5$ and $\langle U_X^2 U_Y^2 \rangle = \langle U_X^2 U_Z^2 \rangle = \langle U_Y^2 U_Z^2 \rangle = 1/15$. Thus:

$$\begin{aligned} \langle \gamma^2 \rangle_L = \quad & \tfrac{1}{5}(\gamma_{XX}^2 + \gamma_{YY}^2 + \gamma_{ZZ}^2) + \\ & \tfrac{2}{15}\big(\gamma_{XX}\gamma_{YY} + \gamma_{XX}\gamma_{ZZ} + \gamma_{YY}\gamma_{ZZ} + \\ & 2\gamma_{XY}^2 + 2\gamma_{XZ}^2 + 2\gamma_{YZ}^2\big). \end{aligned} \tag{C.23}$$

The frequency-dependent longitudinal modulus is therefore expressed as:

$$M(\omega) = M - \frac{1}{\mathcal{V}} \sum_{\ell, TLS} \frac{A_\ell}{1 + i\omega\tau_\ell} \langle \gamma_\ell^2 \rangle_L \tag{C.24}$$

and the dissipation is given by the ratio of the imaginary and real parts of the complex modulus:

$$Q^{-1}(\omega) = \frac{\sum_\ell A_\ell \frac{\omega\tau_\ell}{1+\omega^2\tau_\ell^2} \langle \gamma_\ell^2 \rangle_L}{\mathcal{V}M - \sum_\ell \frac{A_\ell}{1+\omega^2\tau_\ell^2} \langle \gamma_\ell^2 \rangle_L} \tag{C.25}$$

We have checked that for the present system, systematically, $\sum_\ell A_\ell \langle \gamma_\ell^2 \rangle_L \ll \mathcal{V}M$, such that:

$$Q_L^{-1}(\omega) \simeq \frac{1}{\mathcal{V}M} \sum_{\ell, TLS} A_\ell \frac{\omega\tau_\ell}{1+\omega^2\tau_\ell^2} \langle \gamma_\ell^2 \rangle_L \tag{C.26}$$

C.3 Transverse dissipation

With a transverse wave, the medium is sheared along a unit vector $\vec{U}$ parallel to a plane of normal $\vec{V}$. The corresponding strain tensor is $\epsilon(t)/2(U \otimes V + V \otimes U)$. The time-independent term in Eq. C.21 now yields a shear stress $\sigma = G\epsilon$, where G is the shear modulus and the average coupling

term is:

$$\langle\gamma^2\rangle_T = \sum_{ijkl} \gamma_{ij}\gamma_{kl}\langle U_i V_j U_k V_l\rangle. \tag{C.27}$$

Again, only even-power averages are non-zero, and accounting for the fact that $\vec{U}$ and $\vec{V}$ are perpendicular, we find $\langle U_X^2 V_X^2\rangle = \langle U_Y^2 V_Y^2\rangle = \langle U_Z^2 V_Z^2\rangle = 1/15$, $\langle U_X V_X U_Y V_Y\rangle = \langle U_Y V_Y U_Z V_Z\rangle = \langle U_Z V_Z U_X V_X\rangle = -1/15$ and $\langle U_X^2 V_Y^2\rangle = \langle U_X^2 V_Z^2\rangle = \langle U_Y^2 V_Z^2\rangle = 3/15$. Therefore:

$$\begin{aligned}\langle\gamma^2\rangle_T = \quad & \tfrac{1}{15}(\gamma_{XX}^2 + \gamma_{YY}^2 + \gamma_{ZZ}^2) - \tfrac{1}{15}(\gamma_{XX}\gamma_{YY} + \gamma_{YY}\gamma_{ZZ} + \gamma_{ZZ}\gamma_{XX}) + \\ & \tfrac{4}{15}\left(\gamma_{XY}^2 + \gamma_{XZ}^2 + \gamma_{YZ}^2\right),\end{aligned} \tag{C.28}$$

and

$$Q_T^{-1}(\omega) \simeq \frac{1}{\mathcal{V}G} \sum_{\ell,TLS} A_\ell \frac{\omega\tau_\ell}{1+\omega^2\tau_\ell^2}\langle\gamma_\ell^2\rangle_T \tag{C.29}$$

BIBLIOGRAPHY

[1] Linear algebra package, http://www.netlib.org/lapack/.

[2] Rheoman - Multiscale Modeling of Mantle Rheology, Université Lille 1, http://www.umet.univ-lille1.fr/Projets/RheoMan/fr/pour-en-savoir-plus/nudged-elastic-band-2.php.

[3] B. P. Abbott and et al.
Observation of gravitational waves from a binary black hole merger.
Phys. Rev. Lett., 116:061102, 2016.

[4] A. Akhiezer.
On the sound absorption in solids.
J. Phys. (U.S.S.R.), 1:277, 1981.

[5] G. Alaca, P. Skeldon, G. E. Thompson, A. B. Mann, H. Habazaki, and K. Shimizu.
Mechanical properties of amorphous anodic alumina and tantala films using nanoindentation.
Nanotechnology, 13:451, 2002.

[6] B. J. Alder and T. E. Wainwright.
Studies in molecular dynamics. I. General method.
J. Chem. Phys., 31:459, 1959.

[7] M. P. Allen and D. J. Tildesley.
Computer simulation of liquids.
Clarendon Press, 1987.

[8] P. B. Allen, J. L. Feldman, J. Fabian, and F. Wooten.
Diffusons, locons and propagons: Character of atomic vibrations in amorphous Si.
Philos. Mag. B, 79:1715–1731, 1999.

[9] W. Arnold and S. Hunklinger.
Experimental evidence for the direct interaction between two-level systems in glasses at very low temperatures.
Solid State Commun., 17:883, 1975.

[10] N. W. Ashcroft and N. D. Mermin.
Solid state physics.
Brooks Cole, 1976.

[11] G. Baldi, V. M. Giordano, G. Monaco, and B. Ruta.
Sound attenuation at terahertz frequencies and the boson peak of vitreous silica.
Phys. Rev. Lett., 104:195501, 2010.

[12] G. Baldi, V. M. Giordano, B. Ruta, R. Dal Maschio, A. Fontana, and G. Monaco.
Anharmonic damping of terahertz acoustic waves in a network glass and its effect on the density of vibrational states.
Phys. Rev. Lett., 112:125502, 2014.

[13] G. Baldi, V. M. Giordano, B. Ruta, and G. Monaco.
On the nontrivial wave-vector dependence of the elastic modulus of glasses.
Phys. Rev. B, 93:144204, 2016.

[14] G. T. Barkema and N. Mousseau.
Event-based relaxation of continuous disordered systems.
Phys. Rev. Lett., 77:4358, 1996.

[15] J.-L. Barrat and D. Rodney.
Portable implementation of a quantum thermal bath for molecular dynamics simulations.
J. Stat. Phys., 144:679, 2011.

[16] C. R. Bartels, B. Crist, and W. W. Graessley.
Self-diffusion coefficient in melts of linear polymers: Chain length and temperature dependence for hydrogenated polybutadiene.
Macromolecules, 17:2702, 1984.

[17] R. Bassiri, M. R. Abernathy, F. Liou, A. Mehta, E. K. Gustafson, M. J. Hart, N. Kim, A. C. Lin, I. Maclaren, I. W. Martin, R. K. Route, S. Rowan, B. Shyam, J. F. Stebbins, and M. M. Fejer.
Order, disorder and mixing: The atomic structure of amorphous mixtures of titania and tantala.
J. Non-Cryst. Solids, 438:59–66, 2016.

[18] R. Bassiri, K. Evans, K. B. Borisenko, M. M. Fejer, J. Hough, I. Maclaren, I. W. Martin, R. K. Route, and S. Rowan.
Correlations between the mechanical loss and atomic structure of amorphous TiO_2-doped Ta_2O_5 coatings.
Acta. Mater., 61:1070, 2013.

[19] R. Bassiri, F. Liou, M. R. Abernathy, A. C. Lin, N. Kim, A. Mehta, B. Shyam, R. L. Byer, E. K. Gustafson, M. Hart, I. MacLaren, I. W. Martin, R. K. Route, S. Rowan, J. F. Stebbins, and M. M. Fejer.
Order within disorder: The atomic structure of ion-beam sputtered amorphous tantala (a-Ta_2O_5).
APL Mat., 3:036103, 2015.

[20] L. K. Béland, P. Brommer, F. El-Mellouhi, J.-F. Joly, and N. Mousseau.
Kinetic activation-relaxation technique.
Phy. Rev. E, 84:046704, 2011.

[21] Y. M. Beltukov, C. Fusco, D. A. Parshin, and A. Tanguy.
Boson peak and Ioffe-Regel criterion in amorphous siliconlike materials: The effect of bond directionality.
Phys. Rev. E, 93:023006, 2016.

[22] Y. M. Beltukov, V. I. Kozub, and D. A. Parshin.
Ioffe-Regel criterion and diffusion of vibrations in random lattices.
Phys. Rev. B, 87:134203, 2013.

[23] P. Benassi, M. Krisch, C. Masciovecchio, V. Mazzacurati, G. Monaco, G. Ruocco, F. Sette, and R. Verbeni.
Evidence of high frequency propagating modes in vitreous silica.
Phys. Rev. Lett., 77:3835–3838, 1996.

[24] K. Binder and W. Kob.
Glassy materials and disordered solids.
World Scientific Pub. Co., 2005.

[25] H. E. Bömmel and K. Dransfeld.
Excitation and attenuation of hypersonic waves in quartz.
Phys. Rev., 117:1245, 1960.

[26] T. Brink, L. Koch, and K Albe.
Structural origins of the boson peak in metals: From high-entropy alloys to metallic glasses.
Phys. Rev. B, 94:224203, 2016.

[27] R. Bruckner.
Properties and structure of vitreous silica. I.
J. Non-Cryst. Solids, 5:123, 1970.

[28] U. Buchenau.
Mechanical relaxation in glasses and at the glass transition.

Phys. Rev. B, 63:104203, 2000.

[29] U. Buchenau.
Evaluation of X-ray Brillouin scattering data.
Phys. Rev. E, 90:062319, 2014.

[30] U. Buchenau, N. Nücker, and A. J. Dianoux.
Neutron scattering study of the low-frequency vibrations in vitreous silica.
Phys. Rev. Lett., 43:1069, 1984.

[31] U. Buchenau, M. Prager, N. Nücker, A. J. Dianoux, N. Ahmad, and W. A. Phillips.
Low-frequency modes in vitreous silica.
Phys. Rev. B, 34:5665–5673, 1986.

[32] D. G. Cahill and J. E. Van Cleve.
Torsional oscillator for internal friction data at 100 kHz.
J. Non-Cryst. Solids, 60:2706, 1989.

[33] G. Carini, G. Carini, G. D'Angelo, D. Fioretto, and G. Tripodo.
Identification of relaxing structural defects in densified B_2O_3 glasses.
Phys. Rev. B, 90:140204, 2014.

[34] A. Carré, L. Berthier, J. Horbach, S. Ispas, and W. Kob.
Amorphous silica modeled with truncated and screened coulomb interactions: A molecular dynamics simulation study.
J. Chem. Phys., 127:114512, 2007.

[35] J. K. Christie, S. N. Taraskin, and S. R. Elliott.
Vibrational behavior of a realistic amorphous-silicon model.
J. Non-Cryst. Solids, 353:2272–2279, 2007.

[36] J. Classen, C. Enss, C. Bechinger, G. Weiss, and S. Hunklinger.
Low frequency acoustic and dielectric measurements on glasses.
Ann. Physik, 506:315, 1994.

[37] C. Comtet, D. Forest, P. Ganau, G. M. Harry, C. Michel, N. Morgado, V. Pierro, and L. Pinard.
Reduction of tantala mechanical losses in Ta_2O_5/SiO_2 coatings for the next generation of virgo and ligo interferometric gravitational waves detectors.
Paper presented at the 42th Rencontres de Moriond - Gravitational Waves and Experimental Gravity, Mar 2007, La Thuile, Italy, 2007.

[38] T. Corbitt and N. Mavalvala.
Review: Quantum noise in gravitational-wave interferometers.
J. Opt. B Quantum Semiclassical Opt., 6:675–683, 2004.

[39] P. Coussot.
Rheometry of pastes, suspensions, and granular materials.
Wiley, 2005.

[40] T. Damart, E. Coillet, A. Tanguy, and D. Rodney.
Numerical study of the structural and vibrational properties of amorphous Ta_2O_5 and TiO_2-doped Ta_2O_5.
J. Appl. Phys., 119:175106, 2016.

[41] T. Damart, V. M. Giordano, and A. Tanguy.
Nanocrystalline inclusions as a low-pass filter for thermal transport in a-Si.
Phys. Rev. B, 92:094201, 2015.

[42] T. Damart, A. Tanguy, and D. Rodney.
Theory of harmonic dissipation in disordered solids.
Phys. Rev. B, 95:054203, 2017.

[43] E. DeGiuli, A. Laversanne-Finot, G. Düring, E. Lerner, and M. Wyart.
Effects of coordination and pressure on sound attenuation, boson peak and elasticity in amorphous solids.
Soft Matter, 10:5628, 2014.

[44] E. DeGiuli, E. Lerner, C. Brito, and M. Wyart.
Force distribution affects vibrational properties in hard-sphere glasses.
Proc. Nat. Acad. Sci., 111:17054, 2014.

[45] R. Dell'Anna, G. Ruocco, M. Sampoli, and G. Viliani.
High frequency sound waves in vitreous silica.
Phys. Rev. Lett., 80:1236–1239, 1998.

[46] E. Demiralp, T. Çağin, and W. A. Goddard.
Morse stretch potential charge equilibrium force field for ceramics: Application to the quartz-stishovite phase transition and to silica glass.
Phys. Rev. Lett., 82:1708, 1999.

[47] A. Devos, M. Foret, S. Ayrinhac, P. Emery, and B. Rufflé.
Hypersound damping in vitreous silica measured by picosecond acoustics.
Phys. Rev. B, 77:100201, 2008.

[48] P. S. Dobal, R. S. Katiyar, Y. Jiang, R. Guo, and A. S. Bhalla.
Micro-Raman scattering and x-ray diffraction studies of $(Ta_2O_5)_{1-x}(TiO_2)_x$ ceramics.
J. Appl. Phys., 87:8688, 2000.

[49] P. S. Dobal, R. S. Katiyar, Y. Jiang, R. Guo, and A. S. Bhalla.

Raman scattering study of a phase transition in tantalum pentoxide.
J. Raman Spectrosc., 31:1061, 2000.

[50] S. J. Donachie and G. S. Ansell.
The effect of quench rate on the properties and morphology of ferrous martensite.
Metall. Trans. A, 6:1863, 1975.

[51] P. Doussineau, M. Matecki, and W. Schön.
Connection between the low temperature acoustic properties and the glass transition temperature of fluoride glasses.
J. Phys. France, 44:101, 1983.

[52] M. T. Dove.
Introduction to the theory of lattice dynamics.
École thématique de la Société Française de la Neutronique, 12:123, 2011.

[53] N. E. Dowling.
Mechanical behavior of materials.
Pearson, 2012.

[54] J. P. K. Doye.
Network topology of a potential energy landscape: A static scale-free network.
Phys. Rev. Lett., 88:238701, 2002.

[55] E. Duval, A. Mermet, and L. Saviot.
Boson peak and hybridization of acoustic modes with vibrations of nanometric heterogeneities in glasses.
Phys. Rev. B, 75:024201, 2007.

[56] A. Einstein and N. Rosen.
On gravitational waves.
Journal of the Franklin Institute, 223:43–54, 1937.

[57] S. R. Elliott.
Physics of amorphous materials.
Longman, 1984.

[58] D. J. Evans and G. P. Morriss.
Statistical mechanics of nonequilibrium liquids.
Academic Press, 1990.

[59] P. Ewald.
Die Berechnung optischer und elektrostatischer Gitterpotential.
Ann. Phys., 369:253–287, 1970.

[60] H. Eyring.
The activated complex in chemical reactions.
J. .Chem. Phys., 3:107, 1935.

[61] J. Fabian and P. B. Allen.
Theory of sound attenuation in glasses: The role of thermal vibrations.
Phys. Rev. Lett., 82:1478–1481, 1999.

[62] C. Ferrante, E. Pontecorvo, G. Cerullo, A. Chiasera, G. Ruocco, W. Schirmacher, and T. Scopigno.
Acoustic dynamics of network-forming glasses at mesoscopic wavelengths.
Nat. Commun., 4:1793, 2013.

[63] J. D. Ferry.
Viscoelastic Properties of Polymers, 3rd Edition.
Wiley, 1980.

[64] M. E. Fine, H. Van Duyne, and N. T. Kenney.
Low-temperature internal friction and elasticity effects in vitreous silica.
J. Appl. Phys., 25:402, 1954.

[65] R. Flaminio, J. Franc, C. Michel, N. Morgado, L. Pinard, and B. Sassolas.
A study of coating mechanical and optical losses in view of reducing mirror thermal noise in gravitational wave detectors.
Classical Quant. Grav., 27:084030, 2010.

[66] M. Foret, E. Courtens, R. Vacher, and J.-B. Suck.
Scattering investigation of acoustic localization in fused silica.
Phys. Rev. Lett., 77:3831–3834, 1996.

[67] D. B. Fraser.
Acoustic loss of vitreous silica at elevated temperatures.
J. Appl. Phys., 41:6, 1970.

[68] D. Frenkel and B. Smit.
Understanding Molecular Simulation: From Algorithms to Applications.
Academic Press, 2001.

[69] C. Ganter and W. Schirmacher.
Rayleigh scattering, long-time tails, and the harmonic spectrum of topologically disordered systems.
Phys. Rev. B, 82:094205, 2010.

[70] S. Gelin.

Dépôt de films d'oxyde de silicium par vaporisation sous vide: dynamique moléculaire et expériences.
PhD thesis, Université Paris-Est, 2016.

[71] S. Gelin, H. Tanaka, and A. Lemaître.
Anomalous phonon scattering and elastic correlations in amorphous solids.
Nat. Mater., 4736:1177–1181, 2016.

[72] K. S. Gilroy and W. A. Phillips.
An asymmetric double-well potential model for structural relaxation processes in amorphous materials.
Philos. Mag. B, 43:735, 1981.

[73] M. Goldstein.
Viscous liquids and the glass transition: A potential energy barrier picture.
J. Chem. Phys., 51:3728, 1969.

[74] M. Granata and al.
Cryogenic measurements of mechanical loss of high-reflectivity coating and estimation of thermal noise.
Opt. Lett., 38:5268, 2013.

[75] G. S. Grest, S. R. Nagel, and A. Rahman.
Longitudinal and transverse excitations in a glass.
Phys. Rev. Lett., 49:1271–1274, 1982.

[76] T. S. Grigera, V. Martin-Mayor, G. Parisi, and P. Verrocchio.
Vibrational spectrum of topologically disordered systems.
Phys. Rev. Lett., 87:085502, 2001.

[77] E. Hairer, C. Lubich, and G. Wanner.
Geometric numerical integration illustrated by the Störmer/Verlet method.
J. Am. Ceram. Soc., 90:3019, 2007.

[78] R. Hamdan, J. P. Trinastic, and H. P. Cheng.
Molecular dynamics study of the mechanical loss in amorphous pure and doped silica.
J. Chem. Phys., 141:054501, 2014.

[79] G. D. Hammond, A. V. Cumming, J. Hough, R. Kumar, K. Tokmakov, S. Reid, and S. Rowan.
Reducing the suspension thermal noise of advanced gravitational wave detectors.
Class. Quantum Grav., 29:124009, 2012.

[80] J.-P. Hansen and I. R. McDonald.
Theory of simple liquids.

Elsevier Academic Press, 2006.

[81] G. Henkelman, B. P. Uberuaga, and H. Jonsson.
A climbing image nudged elastic band method for finding saddle points and minimum energy paths.
J. Chem. Phys., 113:9901, 2000.

[82] A. Heuer.
Exploring the potential energy landscape of glass-forming systems: from inherent structures via metabasins to macroscopic transport.
J. Phys.: Condens. Matter, 20:373101, 2008.

[83] R. Hollerweger, D. Holec, J. Paulitsch, M. Bartosik, R. Daniel, R. Rachbauer, P. Polcik, J. Keckes, C. Krywka, H. Euchner, and P. H. Mayrhofer.
Complementary ab initio and x-ray nanodiffraction studies of Ta_2O_5.
Acta. Mater., 83:276, 2015.

[84] M. Holz, S. R. Heil, and A. Sacco.
Temperature-dependent self-diffusion coefficients of water and six selected molecular liquids for calibration in accurate 1H NMR PFG measurements.
Phys. Chem. Chem. Phys., 2:4740, 2000.

[85] J. Horbach, W. Kob, and K. Binder.
High frequency sound and the boson peak in amorphous silica.
Eur. Phys. J. B, 19:531–543, 2001.

[86] B. H. Houston, D. M. Photiadis, M. H. Marcus, J. A. Bucaro, X. Liu, and J. F. Vignola.
Thermoelastic loss in microscale oscillators.
Appl. Phys. Lett., 80:1300, 2002.

[87] S. Hunklinger, W. Arnold, S. Stein, R. Nava, and K. Dransfeld.
Saturation of the ultrasonic absorption in vitreous silica at low temperatures.
J. Non-Cryst. Solids, 42:253, 1972.

[88] Radu Iftimie, Peter Minary, and Mark E Tuckerman.
Ab initio molecular dynamics: Concepts, recent developments, and future trends.
Proc. Natl. Acad. Sci. USA, 102:6654, 2005.

[89] A. F. Ioffe and A. R. Regel.
Non-crystalline, amorphous and liquid electronic semiconductors.
Prog. Semicond., 4:89, 1960.

[90] S. S. Iyer and R. N. Candler.

Mode-and direction-dependent mechanical energy dissipation in single-crystal resonators due to anharmonic phonon-phonon scattering.
Phys. Rev. Applied, 5:034002, 2016.

[91] J. Jackle.
On the ultrasonic attenuation in glasses at low temperatures.
Z. Phys., 257:212–223, 1972.

[92] J. Jäckle, L. Piché, W. Arnold, and S. Hunklinger.
Elastic effects of structural relaxation in glasses at low temperatures.
J. Non-Cryst. Solids, 20:365, 1976.

[93] C. Joseph, P. Bourson, and M. D. Fontana.
Amorphous to crystalline transformation in Ta_2O_5 studied by Raman spectroscopy.
J. Raman Spectrosc., 43:1146, 2012.

[94] V. G. Karpov, M. I. Klinger, and F. N. Ignat'ev.
Theory of the low-temperature anomalies in the thermal properties of amorphous structures.
Zh. Eksp. Teor. Fiz., 84:760, 1983.

[95] R. Keil, G. Kasper, and S. Hunklinger.
Distribution of barrier heights in a-$Si0_2$ and a-Se.
J. Non-Cryst. Solids, 164:1183, 1993.

[96] P. Koziatek, J.-L. Barrat, and D. Rodney.
Short- and medium-range orders in as-quenched and deformed SiO_2- glasses: An atomistic study.
J. Non-Cryst. Solids, 414:7–15, 2015.

[97] R. Kubo.
The fluctuation-dissipation theorem.
Rep. Prog. Phys., 29:255, 1966.

[98] K. Kunal and N. R. Aluru.
Akhiezer damping in nanostructures.
Phys. Rev. B, 84:245450, 2011.

[99] C. Lanczos.
An iteration method for the solution of the eigenvalue problem of linear differential and integral operators.
J. Res. Natl. Bur. Std., 45:255, 1950.

[100] J. M. Larkin and A. J. H. McGaughey.

Thermal conductivity accumulation in amorphous silica and amorphous silicon.
Phys. Rev. B, 89:144303, 2014.

[101] S. Le Roux and P. Jund.
Ring statistics analysis of topological networks: New approach and application to amorphous GeS_2 and SiO_2 systems.
Comput. Mater. Sci., 49:70, 2010.

[102] J. Lee, S.-Y. Kim, and J. Lee.
Design of a protein potential energy landscape by parameter optimization.
Science, 108:4525, 2004.

[103] A. Lemaître.
Structural relaxation is a scale-free process.
Phys. Rev. Lett., 113:245702, 2014.

[104] A. Lemaître.
Tensorial analysis of Eshelby stresses in 3D supercooled liquids.
J. Chem. Phys., 143:164515, 2015.

[105] A. Lemaître and C. Maloney.
Sum rules for the quasi-static and visco-elastic response of disordered solids at zero temperature.
J. Stat. Phys., 123:415–453, 2006.

[106] C. Levelut, R. Le Parc, and J. Pelous.
Dynamic sound attenuation at hypersonic frequencies in silica glass.
Phys. Rev. B, 73:052202, 2006.

[107] M. Li, H. X. Tang, and M. L. Roukes.
Ultra-sensitive nems-based cantilevers for sensing, scanned probe and very high-frequency applications.
Nat. Nanotechnol., 2:114–120, 2007.

[108] Q. Li, H. Zhang, B. Cheng, R. Liu, B. Liu, J. Liu, Z. Chen, B. Zou, T. Cui, and B. Liu.
Pressure-induced amorphization in orthorhombic Ta_2O_5: An intrinsic character of crystal.
J. Appl. Phys., 115:193512, 2014.

[109] T. Li, F. A. A. Sandoval, M. Geitner, L. Bellon, G. Cagnoli, V. Dolique, R. Flaminio, M. Granata, C. Michel, N. Morgado, and L. Pinard.
Measurements of mechanical thermal noise and energy dissipation in optical dielectric coatings.
Phys. Rev. D, 89:092004, 2014.

[110] Z. Liang and P. Keblinski.
Sound attenuation in amorphous silica at frequencies near the boson peak.
Phys. Rev. B, 93:054205, 2016.

[111] R. Lifshitz and M. L. Roukes.
Thermoelastic damping in micro- and nanomechanical systems.
Phys. Rev. B, 61:5600–5609, 2000.

[112] J. Lin, N. Masaaki, A. Tsukune, and M. Yamada.
Ta_2O_5 thin films with exceptionally high dielectric constant.
Appl. Phys. Lett., 74:2370, 1999.

[113] X. Q. Liu, X. D. Han, Z. Zhang, L. F. Ji, and Y. J. Jiang.
The crystal structure of high temperature phase ta_2o_5.
Acta Mater., 55:2385, 2007.

[114] J. F. Lutsko.
Generalized expressions for the calculation of elastic constants by computer simulation.
J. Appl. Phys., 65:2991, 1989.

[115] F. W. Lytle, D. E. Sayers, and E. A. Stern.
Extended x-ray-absorption fine-structure technique. II. Experimental practice and selected results.
Phy. Rev. B, 11:4825, 1975.

[116] R. Malek and N. Mousseau.
Dynamics of Lennard-Jones clusters : A characterization of the activation-relaxation technique.
Phys. Rev. E, 62:7723, 2000.

[117] M. L. Manning and A. J. Liu.
Vibrational modes identify soft spots in a sheared disordered packing.
Phys. Rev. Lett., 107:108302, 2011.

[118] B. Mantisi, A. Tanguy, G. Kermouche, and E. Barthel.
Atomistic response of a model silica glass under shear and pressure.
Eur. Phys. J. B, 85:304, 2012.

[119] M. Marinov and N. Zotov.
Model investigation of the Raman spectra of amorphous silicon.
Phys. Rev. B, 55:2938, 1997.

[120] A. Marruzzo, W. Schirmacher, A. Fratalocchi, and G. Ruocco.
Heterogeneous shear elasticity of glasses: the origin of the boson peak.

Sci. Rep., 3:1407, 2013.

[121] I. Martin, E. Chalkley, R. Nawrodt, H. Armandula, R. Bassiri, C. Comtet, M. Fejer, A. Gretarsson, G. Harry, D. Heinert, J. Hough, I. MacLaren, C. Michel, J. Montorio, N. Morgado, S. Penn, S. Reid, R. Route, S. Rowan, C. Schwarz, P. Seidel, W. Vodel, and A. Woodcraft.
Comparison of the temperature dependence of the mechanical dissipation in thin films of Ta_2O_5 and Ta_2O_5 doped with TiO_2.
Classical Quant. Grav., 26:155012, 2009.

[122] I. W. Martin, R. Bassiri, R. Nawrodt, M. M. Fejer, A. Gretarsson, E. Gustafson, G. Harry, J. Hough, I. MacLaren, S. Penn, et al.
Effect of heat treatment on mechanical dissipation in Ta_2O_5 coatings.
Class. Quantum Gravity, 27:225020, 2010.

[123] I. W. Martin, R. Nawrodt, K. Craig, C. Schwarz, R. Bassiri, G. Harry, J. Hough, S. Penn, S. Reid, R. Robie, and S. Rowan.
Low temperature mechanical dissipation of an ion-beam sputtered silica film.
Class. Quantum Grav., 31:035019, 2014.

[124] D. V. Martynov and et al.
Sensitivity of the advanced ligo detectors at the beginning of gravitational wave astronomy.
Phys. Rev. D, 93:112004, 2016.

[125] C. Masciovecchio, G. Baldi, S. Caponi, L. Comez, S. Di Fonzo, D. Fioretto, A. Fontana, A. Gessini, S. C. Santucci, and F. Sette.
Evidence for a crossover in the frequency dependence of the acoustic attenuation in vitreous silica.
Phys. Rev. Lett., 97:035501, 2006.

[126] P. F. McMillan, B. T. Poe, P. H. Gillet, and B. Reynard.
A study of SiO_2 glass and supercooled liquid to 1950 K via high-temperature Raman spectroscopy.
Geochim. Cosmochim. Acta, 58:3653, 1994.

[127] K. P. Menard.
Dynamic Mechanical Analysis: A Practical Introduction, Second Edition.
CRC Press, 2008.

[128] J.F. Meng, K. R. Brajesh, R.S. Katiyar, and A. S. Bhalla.
Raman investigation on $(Ta_2O_5)_{1-x}$-$(TiO_2)_x$ system at different temperatures and pressures.
J. Phys. Chem. Solids, 58:1503, 1997.

[129] G. Mills and H. Jónsson.
Quantum and thermal effects in H_2 dissociative adsorption: Evaluation of free energy barriers in multidimensional quantum systems.
Phys. Rev. Lett., 72:1124, 1994.

[130] G. Mills, H. Jónsson, and G. K. Schenter.
Reversible work transition state theory: application to dissociative adsorption of hydrogen.
Surf. Sci., 324:305, 1995.

[131] Hideyuki Mizuno, Stefano Mossa, and Jean-Louis Barrat.
Relation of vibrational excitations and thermal conductivity to elastic heterogeneities in disordered solids.
Physical Review B, 94:144303, 2016.

[132] G. Monaco and V. M. Giordano.
Breakdown of the debye approximation for the acoustic modes with nanometric wavelengths in glasses.
P. Natl. Acad. Sci., 106:3659–3663, 2009.

[133] G. Monaco and S. Mossa.
Anomalous properties of the acoustic excitations in glasses on the mesoscopic length scale.
P. Natl. Acad. Sci., 106:16907–16912, 2009.

[134] N. Mousseau and G. T. Barkema.
Event-based relaxation of continuous disordered systems.
Phys. Rev. E, 57:2419, 1998.

[135] T. Mura.
Micromechanics of Defects in Solids.
Springer Netherlands, 1982.

[136] P. G. Murray, I. W. Martin, K. Craig, J. Hough, S. Rowan, R. Bassiri, M. M. Fejer, J. S. Harris, B. T. Lantz, A. C. Lin, et al.
Cryogenic mechanical loss of a single-crystalline GaP coating layer for precision measurement applications.
Phys. Rev. D, 95:042004, 2017.

[137] T. Nakamura, Y. Hiraoka, A. Hirata, E. G. Escolar, and Y. Nishiura.
Persistent homology and many-body atomic structure for medium-range order in the glass.
Nanotechnology, 70:304001, 2015.

[138] H. Ono, Y. Hosokawa, K. Shinoda, K. Koyanagi, and H. Yamaguchi.
TaO phonon peaks in tantalum oxide films on Si.

Thin Solid Films, 381:57, 2001.

[139] S. Parke.
Logarithmic decrements at high damping.
Br. J. Appl. Phys., 17:271–273, 1966.

[140] A. Pasquarello and R. Car.
Identification of Raman defect lines as signatures of ring structures in vitreous silica.
Phys. Rev. Lett., 439:5145, 80.

[141] A. P. Paz, I. V; Lebedeva, I. V. Tokatly, and A. Rubio.
Identification of structural motifs as tunneling two-level systems in amorphous alumina at low temperatures.
Phys. Rev. B, 90:224202, 2014.

[142] W. A. Phillips.
Two-level states in glasses.
Rep. Prog. Phys., 50:1657–1708, 1987.

[143] H. Poincaré.
Sur la dynamique de l'électron.
Comptes rendus hebdomadaires des séances de l'Académie des sciences, 140:1504–1508, 1905.

[144] D. R. Queen, X. Liu, J. Karel, H. C. Jacks, T. H. Metcalf, and F. Hellman.
Two-level systems in evaporated amorphous silicon.
J. Non-Cryst. Solids, 426:19, 2015.

[145] A. Rahmani, M. Benoit, and C. Benoit.
Signature of small rings in the Raman spectra of normal and compressed amorphous silica: A combined classical and ab initio study.
Phys. Rev. B, 68:184202, 2003.

[146] J. Reinisch and A. Heuer.
What is moving in silica at 1 K? A computer study of the low-temperature anomalies.
Phys. Rev. Lett., 95:155502, 2005.

[147] Ranko Richert and CA Angell.
Dynamics of glass-forming liquids. V. on the link between molecular dynamics and configurational entropy.
J. Chem. Phys., 108:9016, 1998.

[148] D. Rodney, A. Tanguy, and D. Vandembroucq.
Modeling the mechanics of amorphous solids at different length and time scales.

Model. Simul. Mater. Sci. Eng., 19:083001, 2011.

[149] G. A. Rosales-Sosa, A. Masuno, Y. Higo, H. Inoue, Y. Yanaba, T. Mizoguchi, T. Umada, K. Okamura, K. Kato, and Y. Watanabe.
High elastic moduli of a $54Al_2O_3$-$46Ta_2O_5$ glass fabricated via containerless processing.
Sci. Rep., 5:15233, 2015.

[150] C. Rossignol, J. M. Rampnoux, M. Perton, B. Audoin, and S. Dilhaire.
Generation and detection of shear acoustic waves in metal submicrometric films with ultrashort laser pulses.
Phys. Rev. Lett., 94:166106, 2005.

[151] J. Rottler, S. S. Schoenholz, and A. J. Liu.
Predicting plasticity with soft vibrational modes: From dislocations to glasses.
Phys. Rev. E, 89:042304, 2014.

[152] T. Rouxel.
Elastic properties and short-to medium-range order in glasses.
J. Am. Ceram. Soc., 90:3019, 2007.

[153] M. Rubinstein and R. H. Colby.
Polymer physics.
Oxford University Press, 2003.

[154] B. Rufflé, G. Guimbretière, E. Courtens, R. Vacher, and G. Monaco.
Glass-specific behavior in the damping of acoustic like vibrations.
Phys. Rev. Lett., 96:045502, 2006.

[155] B. Rufflé, E. Courtens, and M. Foret.
Inelastic ultraviolet Brillouin scattering from superpolished vitreous silica.
Phys. Rev. B, 84:132201, 2011.

[156] G. Ruocco and F. Sette.
High-frequency vibrational dynamics in glasses.
J. Phys-Condens. Mat., 13:9141–9164, 2001.

[157] G. Ruocco, F. Sette, R. Di Leonardo, D. Fioretto, M. Krisch, M. Lorenzen, C. Masciovecchio, G. Monaco, F. Pignon, and T. Scopigno.
Nondynamic origin of the high-frequency acoustic attenuation in glasses.
Phys. Rev. Lett., 83:5583–5586, 1999.

[158] G. Ruocco, F. Sette, R. Di Leonardo, G. Monaco, M. Sampoli, T. Scopigno, and G. Viliani.
Relaxation processes in harmonic glasses?
Phys. Rev. Lett., 84:5788–5791, 2000.

[159] S. Sadtler, A. Devos, and M. Foret.
Hypersound damping in vitreous silica measured by ultrafast acoustics.
Phys. Rev. B, 77:100201, 2013.

[160] S. Sastry, P. G. Debenedetti, and F. H. Stillinger.
Signatures of distinct dynamical regimes in the energy landscape of a glass-forming liquid.
Nature, 393:554, 1998.

[161] P. R. Saulson.
Thermal noise in mechanical experiments.
Phys. Rev. D, 42:2437–2445, 1990.

[162] W. Schirmacher, G. Diezemann, and C. Ganter.
Harmonic vibrational excitations in disordered solids and the boson peak.
Phys. Rev. Lett., 81:136–139, 1998.

[163] H. R. Schober.
Vibrations and relaxations in a soft sphere glass: boson peak and structure factors.
J. Phys-Condens. Mat., 16:S2659–S2670, 2004.

[164] B. Schweinhart, J. K. Mason, and R. D. MacPherson.
Topological similarity of random cell complexes and applications to dislocation configurations.
Phy. Rev. E, 93:062111, 2016.

[165] A. Seeger, H. Donth, and F. Pfaff.
The mechanism of low temperature mechanical relaxation in deformed crystals.
Discuss. Faraday Soc., 23:19, 1957.

[166] Brett Shapiro, Rana X Adhikari, Odylio Aguiar, Edgard Bonilla, Danyang Fan, Litawn Gan, Ian Gomez, Sanditi Khandelwal, Brian Lantz, Tim MacDonald, et al.
Cryogenically cooled ultra low vibration silicon mirrors for gravitational wave observatories.
Cryogenics, 81:83, 2017.

[167] S. K. Sharma, J. F. Mammone, and M. F. Nicol.
Raman investigation of ring configurations in vitreous silica.
Nature, 292:140, 1981.

[168] N. S. Shcheblanov, B. Mantisi, P. Umari, and A. Tanguy.
Detailed analysis of plastic shear in the Raman spectra of SiO_2 glass.
J. Non-Cryst. Solids, 428:6–19, 2015.

[169] M. S. Shell, P. G. Debenedetti, and A. Z. Panagiotopoulos.

Molecular structural order and anomalies in liquid silica.
Phys. Rev. E, 66:011202, 2002.

[170] H. W. Sheng, W. K. Luo, F. M. Alamgir, J. M. Bai, and E. Ma.
Atomic packing and short-to-medium-range order in metallic glasses.
Nature, 439:419, 2006.

[171] H. Shintani and H. Tanaka.
Universal link between the boson peak and transverse phonons in glass.
Nat. Mater., 7:870–877, 2008.

[172] B. Shyam, K. H. Stone, R. Bassiri, M. M. Fejer, M. F. Toney, and A. Mehta.
Measurement and modeling of short and medium range order in amorphous Ta_2O_5 thin films.
Sci. Rep., 6:32170, 2016.

[173] M. Sitarz, M. Handke, and W. Mozgawa.
Identification of silicooxygen rings in SiO_2 based on IR spectra.
Spectroc. Acta A, 59:1819, 2000.

[174] E. Stavrou, J. M. Zaug, S. Bastea, and M. Kunz.
A study of tantalum pentoxide ta_2o_5 structure up to 28 GPa.
J. Appl. Phys., 121:175901, 2017.

[175] J. Steinlechner, I. W. Martin, J. Hough, C. Krüger, S. Rowan, and R. Schnabel.
Publisher's note: Thermal noise reduction and absorption optimization via multimaterial coatings.
Phys. Rev. D, 91:069904, 2015.

[176] F. H. Stillinger and T. A. Weber.
Packing structures and transitions in liquids and solids.
Science, 225:983, 1985.

[177] P. Tangney and S. Scandolo.
An ab initio parametrized interatomic force field for silica.
J. Chem. Phys, 117:8898, 2002.

[178] A. Tanguy.
Vibration modes and characteristic length scales in amorphous materials.
JOM, 67:1832–1839, 2015.

[179] A. Tanguy, B. Mantisi, and M. Tsamados.
Vibrational modes as a predictor for plasticity in a model glass.
Europhys. Lett., 90:16004, 2010.

[180] A. Tanguy, J. P. Wittmer, F. Leonforte, and J.-L. Barrat.
Continuum limit of amorphous elastic bodies: A finite-size study of low-frequency harmonic vibrations.
Phys. Rev. B, 66:174205, 2002.

[181] S. N. Taraskin and S. R. Elliott.
Nature of vibrational excitations in vitreous silica.
Phys. Rev. B, 56:8605, 1997.

[182] S. N. Taraskin and S. R. Elliott.
Anharmonicity and localization of atomic vibrations in vitreous silica.
Phys. Rev. B, 59:8572–8585, 1999.

[183] S. N. Taraskin and S. R. Elliott.
Low-frequency vibrational excitations in vitreous silica: the Ioffe-Regel limit.
J. Phys-Condens. Mat., 11:A219–A227, 1999.

[184] S. N. Taraskin and S. R. Elliott.
Ioffe-Regel crossover for plane-wave vibrational excitations in vitreous silica.
Phys. Rev. B, 61:12031–12037, 2000.

[185] J. Tersoff.
New empirical approach for the structure and energy of covalent systems.
Phys. Rev. B, 37:6991, 1988.

[186] C. Thomsen, H. Grahn, H. J. Maris, and J. Tauc.
Surface generation and detection of phonons by picosecond light pulses.
Phys. Rev. B, 34:4129, 1986.

[187] D. Tielburger, R. Merz, R. Ehrenfels, and S. Hunklinger.
Thermally activated relaxation processes in vitreous silica: An investigation at high pressures.
Phys. Rev. B, 45:2750, 1992.

[188] K. A. Topp and D. G. Cahill.
Elastic properties of several amorphous solids and disordered crystals below 100 K.
Z. Phys. B, 101:235, 1996.

[189] J. P. Trinastic, R. Hamdan, C. Billman, and H.-P. Cheng.
Molecular dynamics modeling of mechanical loss in amorphous tantala and titania-doped tantala.
Phys. Rev. B, 93:014105, 2016.

[190] J. P. Trinastic, R. Hamdan, Y. Wu, L. Zhang, and H. Cheng.

Unified interatomic potential and energy barrier distributions for amorphous oxides.
J. Chem. Phys., 21:154506, 2013.

[191] M. Tsamados, A. Tanguy, C. Goldenberg, and J.-L. Barrat.
Local elasticity map and plasticity in a model Lennard-Jones glass.
Phys. Rev. E, 80:026112, 2009.

[192] H.-C. Tseng, J.-S. Wu, and R.-Y. Chang.
Linear viscoelasticity and thermorheological simplicity of n-hexadecane fluids under oscillatory shear via non-equilibrium molecular dynamics simulations.
Phys. Chem. Chem. Phys., 12:4051, 2010.

[193] R. Vacher, E. Courtens, and M. Foret.
Anharmonic versus relaxational sound damping in glasses. II. Vitreous silica.
Phys. Rev. B, 72:214205, 2005.

[194] B. W. H. van Beest, G. J. Kramer, and R. A. van Santen.
Force fields for silicas and aluminophosphates based on ab initio calculations.
Phys. Rev. Lett., 64:1955, 1990.

[195] G. H. Vineyard.
Frequency factors and isotope effects in solid state rate processes.
J. Phys. Chem. Solids, 3:121, 1957.

[196] M. Vladkov and J.-L. Barrat.
Linear and nonlinear viscoelasticity of a model unentangled polymer melt: Molecular dynamics and rouse modes analysis.
Macromol. Theor. Simul., 15:252–262, 2006.

[197] K. Vollmayr, W. Kob, and K. Binder.
Cooling-rate effects in amorphous silica: A computer-simulation study.
Phys. Rev. B, 54:15808, 1996.

[198] H. Wagner, D. Bedorf, S. Küchemann, M. Schwabe, B. Zhang, W. Arnold, and K. Samwer.
Local elastic properties of a metallic glass.
Nat. Mater., 10:439–442, 2011.

[199] D. J. Wales.
A microscopic basis for the global appearance of energy landscapes.
Science, 293:2067, 2001.

[200] D. J. Wales.
Decoding the energy landscape: extracting structure, dynamics and thermodynamics.
Phil. Trans. R. Soc. A, 370:2877, 2012.

[201] Z. Wang, G. Bao, H. Jiao, B. Ma, J. Zhang, T. Ding, and X. Cheng.
Interfacial damage in a Ta_2O_5/SiO_2 double cavity filter irradiated by 1064 nm nanosecond laser pulses.
Opt. Express, 21:30623, 2013.

[202] E. Wigner.
The transition state method.
Trans. Faraday Soc., 34:29, 1938.

[203] J. P. Wittmer, H. Xu, O. Benzerara, and J. Baschnagel.
Fluctuation-dissipation relation between shear stress relaxation modulus and shear stress autocorrelation function revisited.
Molecular Physics, 113:2881–2893, 2015.

[204] D. Wolf.
Reconstruction of NaCl surfaces from a dipolar solution to the Madelung problem.
Phys. Rev. Lett., 68:3315, 1992.

[205] J. J. Yeo, Z. S. Liu, and T. Y. Ng.
Enhanced thermal characterization of silica aerogels through molecular dynamics simulation.
Modelling Simul. Mater. Sci. Eng., 21:075004, 2013.

[206] A. Zaccone, J. R. Blundell, and E. M. Terentjev.
Network disorder and nonaffine deformations in marginal solids.
Phys. Rev. B, 84:174119, 2011.

[207] R. C. Zeller and R. O. Pohl.
Thermal conductivity and specific heat of noncrystalline solids.
Phys. Rev. B, 4:2029–2041, 1971.